

**The effect of strain path changes on the
subsequent recrystallisation properties of
aluminium alloys**

by

Randulf Valle

A thesis submitted to
The Norwegian University of Science and Technology (NTNU)
in partial fulfillment of the requirements for the degree of

Doktor Ingeniør

Trondheim
January 2004

Acknowledgements

The work presented in this thesis has been carried out at NTNU in Trondheim and at TU Delft in the Netherlands, in the period August 2000 to December 2003. The project has been funded by the Netherlands Institute for Metals Research (NIMR) and they are gratefully acknowledged for having done so. Special thanks also go to my supervisors; Professor Erik Nes and Professor Sybrand van der Zwaag, for their efforts, guiding a chemical engineer in to the world of metallurgy.

Corus RD and T IJmuiden, and in particular Dr. Menno van der Winden, is acknowledged for letting me use their multi mill for the hot rolling trials. Acknowledgements also go to all the people at the NIMR. In particular to Dr. Shangping Chen for helping me out with the FEM-simulations, Dr. Bruce Davenport for a thorough introduction to the field of strain path related recrystallisation phenomena and to Dr. David N. Hanlon and Jane Breedon for making my time in The Netherlands socially as well as scientifically stimulating. To those not mentioned by names – I have not forgot you!

I would also like to acknowledge my colleagues at the department of materials technology at NTNU. Special thanks go to Dr. Bjørn Holmedal for help with the ALFLOW model, Dr. Knut Sjølstad for assistance with the ALSOFT model, as well as Stian Tangen and Dr. Øyvind Ryen for help, discussions and lots of fun during the three years.

Special thanks go to Kaare Gether, Magnus Korpås and Nina Linn Ulstein. There is comfort in common destiny!

Trondheim January 2004

Randulf Valle

Contents

ACKNOWLEDGEMENTS	i
CONTENTS	iii
ABSTRACT	ix

1	INTRODUCTION	1
1.1	THE PURPOSE OF THE STUDY	1
1.2	THE STRUCTURE OF THE THESIS	1

Part I: Theoretical background

2	GENERAL THEORETICAL BACKGROUND	3
2.1	STRAIN AND STRAIN PATH – DEFINITIONS	4
2.1.1	Deformation processes and strain path change angle	4
2.2	THE MECHANICS OF STRAIN PATH CHANGES	4
2.2.1	The Baushinger Effect	4
2.2.2	The cross effect	6
2.3	MICROSTRUCTURAL CHANGES DURING DEFORMATION	7
2.3.1	The effect of strain path changes on microstructure	12
2.4	MODELLING THE EVOLUTION IN MECHANICAL PROPERTIES DURING PLASTIC DEFORMATION	14
2.4.1	Empirical relations	14
2.4.2	Physically based models	16
2.4.3	Texture	17
2.4.4	Texture and strain path	18
2.5	ANNEALING OF DEFORMED MATERIAL	20
2.5.1	Introduction	20
2.5.2	Recovery of deformed material	20
2.5.3	Driving pressure for recrystallisation	22
2.5.4	Effect of small particles during annealing of deformed material	23
2.5.5	Nucleation of recrystallised grains	25
2.5.6	Recrystallisation kinetics	34
2.5.7	Recrystallisation and strain path	36
2.5.8	Recrystallisation textures	38
2.5.9	Recrystallisation models	39

Part II:

Strain path effects on recrystallisation after hot torsion

3	THEORETICAL BACKGROUND	41
3.1	MONOTONIC AND CYCLIC TORSION – CONCEPT AND DEFINITIONS	41
3.2	MECHANICAL PROPERTIES	42
	3.2.1 Notation of orientations	42
	3.2.2 Calculation of stress, strain and strain rate	42
3.3	THE STRESS-STRAIN CURVE	44
	3.3.1 Monotonic torsion	44
	3.3.2 Cyclic torsion	47
3.4	MICROSTRUCTURAL DEVELOPMENT	49
	3.4.1 Grain shape – spacing between high angle boundaries	49
	3.4.2 Subgrain size	50
3.5	TEXTURE DEVELOPMENT	51
	3.5.1 Monotonic torsion	51
	3.5.2 Cyclic torsion	52
	3.5.3 Modeling of torsion texture development	52
3.6	ANNEALING AFTER TORSION	53
	3.6.1 Recrystallisation	53
	3.6.2 The effect of strain path	54
	3.6.3 Geometric dynamic recrystallisation	54
4	EXPERIMENTAL TECHNIQUES	57
4.1	MATERIALS AND HEAT TREATMENT	57
	4.1.1 The alloys	57
	4.1.2 Homogenization	57
4.2	HOT TORSION	57
	4.2.1 Sample geometry	57
	4.2.2 Temperature control	58
4.3	ANNEALING	59
4.4	MICROSTRUCTURAL CHARACTERISATION	59
	4.4.1 Sample geometry and preparation	59
	4.4.2 Light optical microscopy	60
	4.4.3 Scanning electron microscopy	60
4.5	GLOBAL TEXTURE MEASUREMENTS	61
	4.5.1 Sample preparation	61
	4.5.2 Reference frame and notation of orientations	62
	4.5.3 Measuring routines	62

5	EXPERIMENTAL RESULTS	65
5.1	THE STARTING MATERIAL	65
5.2	MECHANICAL BEHAVIOR	66
	5.2.1 Specimen shape change	66
	5.2.2 Corrected stress and strain	67
	5.2.3 Corrected stress strain curves	69
5.3	THE DEFORMED STATE	71
	5.3.1 Light optical micrographs	71
	5.3.2 EBSD – images	72
	5.3.3 Subgrain sizes and misorientations	76
	5.3.4 Distance between high angle boundaries	78
	5.3.5 Fractions of boundaries of low, medium and high misorientation	79
	5.3.6 Deformation textures	81
5.4	THE RECRYSTALLISATION PROCESS	83
	5.4.1 Recrystallised grain sizes	83
	5.4.2 Recrystallisation textures	84
6	DISCUSSION	87
6.1	A CLOSER LOOK AT THE STRESS-STRAIN DATA	87
	6.1.1 Influence of deformation conditions	87
	6.1.2 The flow stress curve after monotonic torsion	91
	6.1.3 The flow stress curve after cyclic torsion	92
	6.1.4 The difference in flow stress between cyclic and monotonic torsion	93
6.2	ON THE DEVELOPMENT OF DEFORMATION TEXTURE	98
6.3	RECRYSTALLISATION	100
	6.3.1 Driving pressure for recrystallisation	100
	6.3.2 Nucleation mechanisms	103
6.4	MODELING OF RECRYSTALLISATION AFTER CYCLIC AND MONOTONIC TORSION	106
	6.4.1 The model	106
	6.4.2 Nucleation mechanisms	107
6.5	MODELLING OF RECRYSTALLISATION IN AA1050 DEFORMED AT 300OC	111
6.6	MODELING OF RECRYSTALLISATION IN AA3103 DEFORMED AT 300OC	112
6.7	IS THE MODEL VALID FOR THE PRESENT DEFORMATION CONDITIONS?	114

6.7.1	Grain shape	115
6.7.2	Break up of second phase particles	118
6.7.3	Geometric dynamic recrystallisation	118
7	CONCLUSIONS	121
Part III: Recrystallisation after single pass hot rolling		
<hr/>		
8	PURPOSE AND OUTLINE OF THE EXPERIMENT	125
8.1	PURPOSE AND MOTIVATION	125
8.2	OUTLINE OF THE EXPERIMENT	126
9	THE HOT ROLLING PROCESS – BACKGROUND AND PREVIOUS WORK	129
9.1	THE INDUSTRIAL HOT ROLLING PROCESS	129
9.1.1	Breakdown rolling	129
9.1.2	Tandem rolling	130
9.2	MECHANICAL DESCRIPTION OF THE HOT ROLLING PROCESS	130
9.2.1	Strain and strain rate	130
9.2.2	Surface shear	132
9.3	THE HOT ROLLED MATERIAL – PROPERTIES THROUGH THICKNESS	133
9.3.1	Microstructure	134
9.3.2	Intermetallic particles and alloying elements	134
9.3.3	Strain path effects	135
9.4	HOT ROLLING TEXTURES	135
9.5	RECRYSTALLISATION AFTER HOT ROLLING	137
9.5.1	Recrystallisation after Industrial hot rolling	137
9.5.2	Strain path effects	138
9.5.3	Modeling of recrystallisation after hot rolling	140
10	MODELS USED IN THIS STUDY	141
10.1	THE MOTIVATION OF MODEL DEVELOPMENT	141
10.2	FEM-SIMULATIONS	143
10.2.1	Constitutive equation	143
10.2.2	The FEM-analysis	144
10.3	THE WORK HARDENING MODEL – ALFLOW	148

10.4	THE SOFTENING MODEL - ALSOFT	158
10.4.1	Flow stress	159
10.4.2	Recovery	159
10.4.3	Recrystallisation kinetics	160
10.4.4	The density of sites of different categories	160
11	EXPERIMENTAL TECHNIQUES	163
11.1	THE HOT ROLLING MILL	163
11.2	HARDNESS MEASUREMENTS	163
11.3	CONDUCTIVITY MEASUREMENTS	163
11.4	MICROSTRUCTURAL CHARACTERISATION	164
11.4.1	Sample preparation	164
11.4.2	Particle characterisation	164
11.4.3	Texture measurements - reference frame and notation of orientations	164
12	EXPERIMENTAL RESULTS	167
12.1	THE STARTING MATERIAL	167
12.2	THE HOT ROLLING EXPERIMENT	168
12.3	AS DEFORMED MICROSTRUCTURE	168
12.4	HARDNESS MEASUREMENTS	169
12.5	CONDUCTIVITY MEASUREMENTS	170
12.6	DISTRIBUTION OF SECOND PHASE PARTICLES	171
12.7	DEFORMATION TEXTURES	172
12.8	RECRYSTALLISATION KINETICS	173
12.9	RECRYSTALLISED GRAIN SIZES	174
13	MODELLING RESULTS	177
13.1	FEM-SIMULATIONS AND PREDICTION OF MICROSTRUCTURE	177
13.1.1	The modeling procedure, outline and definitions	177
13.1.2	Mechanical properties	178
13.1.3	Microstructure evolution through the rolling pass	181
13.1.4	Parameter sensitivity	184
13.1.5	Texture evolution	187
13.2	MODELING RECRYSTALLISATION - ALSOFT	188
13.2.1	Input values	188
13.2.2	Modeling results	188

14	DISCUSSION	191
14.1	AS DEFORMED MICROSTRUCTURE	191
14.2	RECRYSTALLISATION	192
14.2.1	A simplified modeling approach	192
14.2.2	Nucleation	195
14.2.3	Summing up	198
14.2.4	Concurrent precipitation	198

15	CONCLUSIONS	201
-----------	--------------------	------------

Part IV: Summing up

16	SUMMING UP	203
16.1	STORED ENERGY	203
16.1.1	The concept of strain efficiency	203
16.1.2	Flow stress as a measure of stored energy	204
16.1.3	Driving pressure and micro structure	205
16.2	NUCLEATION	210
16.2.1	Nucleation mechanisms	210
16.2.2	Site saturation	211
16.3	COMPARISON OF THE PURPOSED MECHANISMS – INFLUENCE OF MAGNITUDE OF STRAIN REVERSAL	212
16.3.1	Driving pressure	212
16.3.2	Particle stimulated nucleation	213
16.3.3	Nucleation from grain boundaries	214
16.4	FUTURE WORK – SUGGESTIONS, THOUGHTS AND CHALLENGES	214
16.4.1	Alloy selection	215
16.4.2	Non complete reversals	215

17	REFERENCES	217
-----------	-------------------	------------

Abstract

A study of strain path related effects on recrystallisation in aluminium has been carried out. The recrystallisation process has been studied after deformation in torsion and one pass hot rolling. For both deformation modes, the work has been a combination of experimental studies of the deformation microstructure and recrystallisation process, as well as use of models for prediction of the deformation- and recrystallisation process.

For deformation in torsion AA1050 and AA3103 has been studied. Cyclic deformation to zero net strain resulted in restoration of the initial grain structure, while monotonic deformation yielded an increasingly more elongated grain structure. Studies by EBSD revealed no difference in subgrain size as function of strain path, but the subgrain misorientation was larger after monotonic deformation. Similarly, the distance between high angle boundaries was smaller after monotonic deformation. The recrystallised grain size was larger after cyclic deformation, compared to monotonic deformation to the same cumulative strain. In AA1050 the difference in recrystallised grain size was mainly seen as an effect of difference in grain boundary area, leading to fewer nuclei after cyclic deformation. A small difference in driving pressure also contributed to the difference in recrystallised grain size. In AA3103 an additional effect of weakening of deformation zones surrounding particles was purposed, resulting in lower density of PSN-nuclei after cyclic deformation and accordingly larger grain size.

The experimental study of the hot rolling pass was performed on an AA3103 alloy. A slight increase in Vickers hardness was seen from center to surface of the rolling slab after deformation. The microstructure after rolling was predicted by a combination of FEM-simulations and a microstructure model. This approach resulted in a larger predicted gradient in flow stress through thickness than calculated from the hardness measurements. The recrystallisation

kinetics were monitored and were found to be fastest in the surface areas. The experimentally measured gradient in recrystallisation kinetics from center to surface was much larger than what was modeled. This was seen as an effect of the models limited coverage of changes in the density of nuclei as a result of other mechanisms than a difference in driving pressure.

1 Introduction

1.1 *The purpose of the study*

For the aluminium industry to keep its present competitiveness, it is important to be able to provide tailored products of superior quality to its customers. The industry also has to work towards the goal of zero waste production through the processing lines. This requires optimised processes and full control of processing parameters. It is now accepted that such control can only be achieved by using models that predict the influence of changes in the process on the final product. In established metallurgical models, the recrystallisation behaviour of aluminium is related to the net strain after deformation, ignoring the strain path in which the strain is achieved. However, recent research has shown that the strain path does effect the recrystallisation process in terms of kinetics, final grain size and texture. Still, most experimental studies so far have concentrated on simple strain path changes in texture free materials. Although strain path effects are expected to affect recrystallisation after industrial processes like forging and hot rolling, the understanding of the phenomena in industrial terms is still limited.

The purpose of this work is twofold: (i) To achieve a better understanding of recrystallisation dependence on strain path in torsion for a texture free material. (ii) To search for signs of strain path effects on the through thickness recrystallisation properties after hot rolling.

1.2 *The structure of the thesis*

The thesis is divided in four parts. *Part one* consists of the general theoretical background of the subjects of strain and strain paths, as well as a literature review of the development of deformation microstructure and of the recrystallisation process. In *part two* the

recrystallisation behaviour after cyclic and monotonic torsion is investigated. The objective is to understand the difference in recrystallised grain size as a function of strain path. A mechanism for the observed change is proposed, and introduced in an existing recrystallisation model. In *part three* a hot rolling pass with the subsequent recrystallisation process is studied in order to determine if strain path effects are influencing the recrystallisation process. The process is studied both experimentally and by FEM-simulations, combined with models for microstructure development during deformation and recrystallisation. *Part four* connects the results and conclusions from torsion and hot rolling. The comparability of the two processes, in terms of strain path effects on recrystallisation is discussed and the results are compared to existing studies of the subject. Suggestions for further work are also given.

Part I: Theoretical background

2 General theoretical background

2.1 Strain and strain path – definitions

For the description of strain path experiments the definitions of cumulative and net strain as well as the strain path change angle is important. The net strain is the vector sum of the strain increments, while the cumulative strain is the sum of the absolute values of the vectors. The strain path angle (Hutchinson and Davis (1983)) is the angle between the strain vectors in the deviatoric strain space. These definitions are exemplified in fig. 2.1 for the case of deformation in two dimensions. In case a, deformation in y-direction is followed by an increment in the x-direction. This represents a strain path change of 90° . The strain vectors and the resulting net strain are shown in fig. 2.1a. In fig. 2.1b a 180° change in strain path is shown. Deformation from 0-A is followed by a reverse deformation from A-B. The resulting net strain is 0-B, while the cumulative strain in this case is $\text{abs}(0-A) + \text{abs}(B-A)$

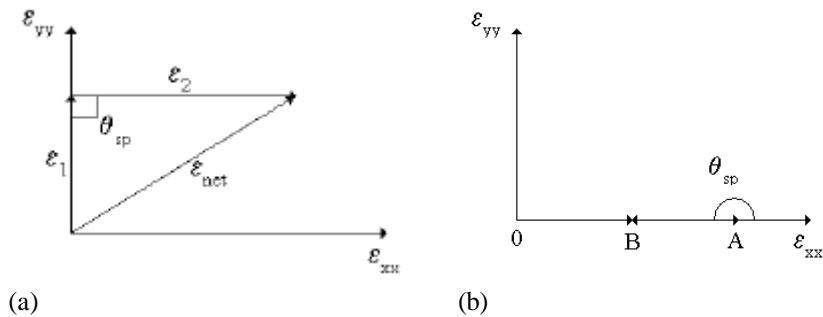


Fig 2.1: Strain path changes and corresponding strain path change angles.

2.1.1 Deformation processes and strain path change angle

Most of the studies of strain path effects have been carried out in tension/compression or torsion/reversed torsion. These are both processes with a 180° strain path change. Combination of torsion and tension/compression represents a 90° strain path change. Equal channel angular die pressing (ECAP) with a die angle of 90° gives opportunities for 90° and 180° strain path changes. Combinations of free compression and channel die compression enable strain path change angles of 90°, 120° and 180° (Higginson (2002)).

2.2 The mechanics of strain path changes

2.2.1 The Baushinger Effect

If a sample is deformed in one direction past its initial yield stress, for instance in tension, and then loaded in the opposite direction, the flow stress in reloaded direction will be smaller than in the original. This path dependency of the flow stress is known as the Baushinger effect. The magnitude of Baushinger effect displayed varies greatly from system to system. Some examples are shown in fig. 2.2.

The Baushinger effect is normally explained as a result of the microstructure in the deformed metal. During forward deformation dislocations tend to accumulate at barriers, forming cells. As the direction of deformation is reversed some of the dislocation lines may move at a lower shear stress as there are less barriers to the rear of the dislocations than in the front. This results in yielding at a lower flow stress. Another explanation is the untangling of cell structure at room temperature and subgrain structure at elevated temperature. This mechanism was confirmed by measurements of electron microscopy studies performed by Hasegawa et al. (1975) in tension, compression experiments. Images showed dissolution of subgrain boundaries and cell walls after strain reversal. Materials

Part I: Theoretical background

subjected to this mechanism are characterised by a plateau in the flow stress after strain reversal.

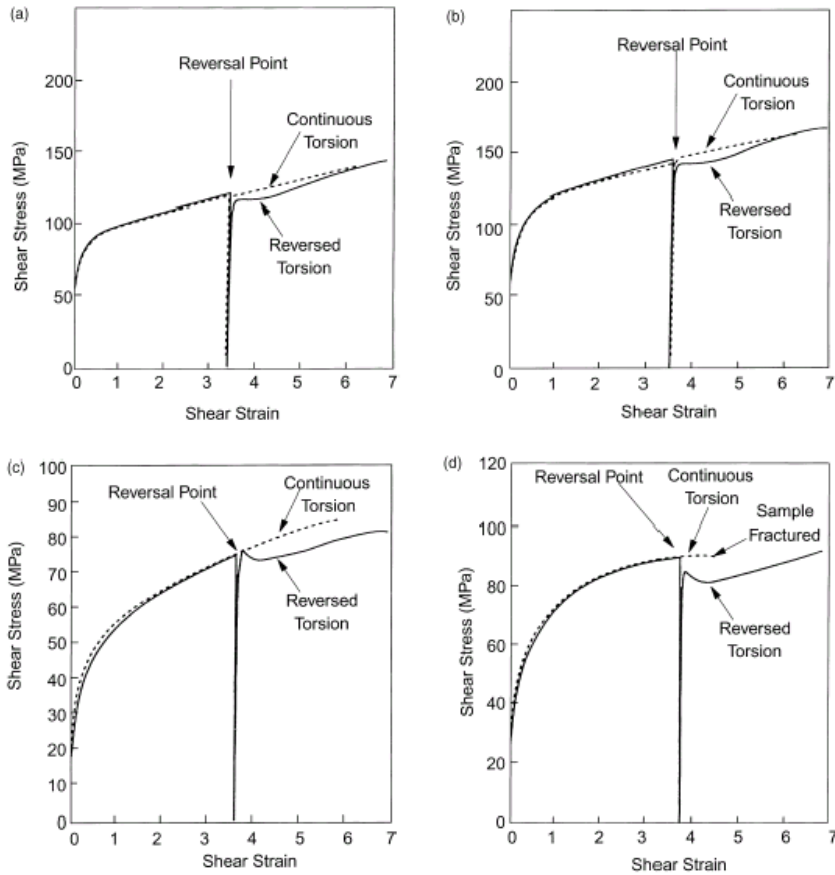


Fig 2.2: The Baushinger effect in torsion. (a):Al1%Mg; (b): Al-2%Mg; (c): Al-0.17%Fe and (d): Al-0.8%Mn. From Stout and Rollett (1990)

Non-shearable second phase particles result in a stronger Baushinger effect. The explanation for this differs with the amount of prestrain prior to strain reversal. After small prestrains, the strong Baushinger effect is due to internal elastic back stresses exerted by the strong precipitates on the metal matrix. Upon reversal of strain

these internal stresses combine with the applied stress to induce yielding at lower levels, compared to initial loading directions. (Stoltz and Pelloux (1976)) Still, these effects are limited by thermal relaxation of the matrix, and were found by Bate and Wilson (1986) to be non-existent at strains exceeding $\epsilon=0.02$ after reversal. However, the same effect of non-shearable particles is observed after large prestrains. Here the large Baushinger effect is explained as a result of pile up of dislocations against the barriers represented by the particles. This results in fewer barriers to the rear of the dislocations, compared to the front, and thus a considerable reduction in flow stress upon reversal. (Stout and Rollett (1990))

2.2.2 The cross effect

If the strain path change is close to 90° , another effect appears – namely the cross effect. In fig. 2.3 the cross effect is shown for steel, deformed in tension 90° to the rolling direction of previous cold rolling. As fig. 2.3 shows, loading 90° to prior deformation direction results in hardening past the initial flow stress followed by a rapid decrease in flow stress. For steel, this behaviour is explained as a result of dislocation walls acting as strong obstacles to the 90° tensile deformation. These obstacles are subsequently sheared locally, resulting in the reduction of stress. For aluminium deformed under similar conditions the behaviour has been explained by shortage of mobile dislocations in the initial stage, causing the hardening. The subsequent softening has been explained as a result of rapid dislocation multiplication.

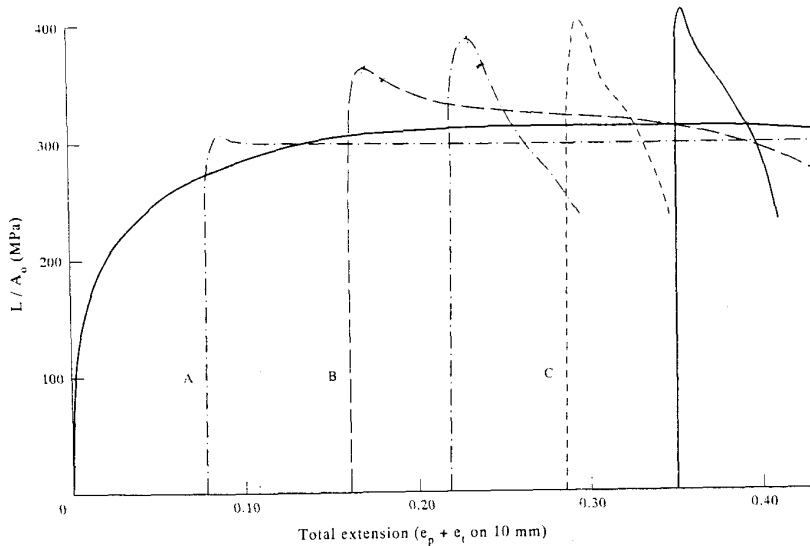


Fig 2.3: The effect of prestrain in rolling, on the stress strain relationship in subsequent tension tests 90° to the rolling direction for fine grained IF steel. (Wilson and Bate 1993)

2.3 Microstructural changes during deformation

Although the deformed microstructure has been a topic for detailed investigations for decades, a complete understanding of the phenomena has not been achieved. Commonly, the deformed microstructure is described by four parameters. The spacing of high angle boundaries, the subgrain size, the subgrain boundary misorientation and the dislocation density inside subgrains. At low strains the subgrain boundary misorientation is replaced by the thickness of the cell walls and the dislocation density inside the cell walls.

Grain elongation and the spacing of high angle grain boundaries

During deformation, grains will elongate in a manner characteristic for the deformation mode. This shape change of the grains may be calculated on a purely geometrical basis. Considering a cubic grain of initial length and diameter of L_0 and D_0 respectively. During

deformation the length of the grain will increase in a manner characteristic for the deformation mode, $L(\mathbf{e})$, and assuming conservation of volume, the high angle boundary separation D_{GSC} will be:

$$D_{GSC} = D_0 \frac{L_0}{L(\mathbf{e})} \quad (2.1)$$

however the eq. is only valid for strains below the critical strain required to pinch off the grain. Also, if the strain path is changed during deformation, obviously the spacing of high angle boundaries will be affected. If the strain is reversed 180° the spacing will start to increase again.

Subgrain size

The development of subgrain size with strain and temperature has been a subject of numerous investigations, both in TEM, and more recently by the use of EBSD. The average subgrain size after hot deformation is a function of temperature, strain and strain rate. The subgrain size tends to increase with increasing temperature, and decrease with increasing strain and strain rate. The subgrain size also tends to decrease with increasing amounts of elements in solid solution. This is illustrated in fig 2.4, where the subgrain size is plotted as a function of the temperature corrected strain rate Z . For hot deformation this Z -value, the Zener-Hollomon parameter, is often used as a measure of the deformation condition, and is defined as:

$$Z = \dot{\mathbf{e}} \exp\left(\frac{Q}{RT}\right) \quad (2.2)$$

Where Q is the activation energy, R is the molar gas constant, T is the temperature and $\dot{\mathbf{e}}$ is the strain rate. In calculating the Z -value an activation energy $U=156\,000\text{J/mol}$ is commonly selected.

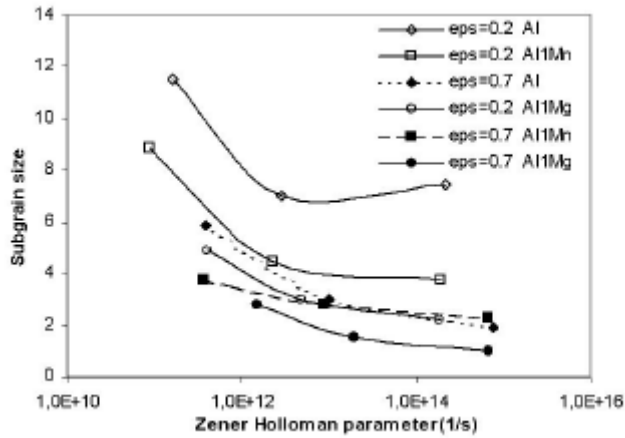


Fig 2.4: Subgrain size as function of alloy, strain and Zener Hollomon parameter. Furu et al. (1996)

Combining temperature and strain rate, the inverse steady state subgrain size is found to scale with the logarithm the Zener-Hollomon parameter for the intermediate range of hot deformation. This is shown in fig. 2.5.

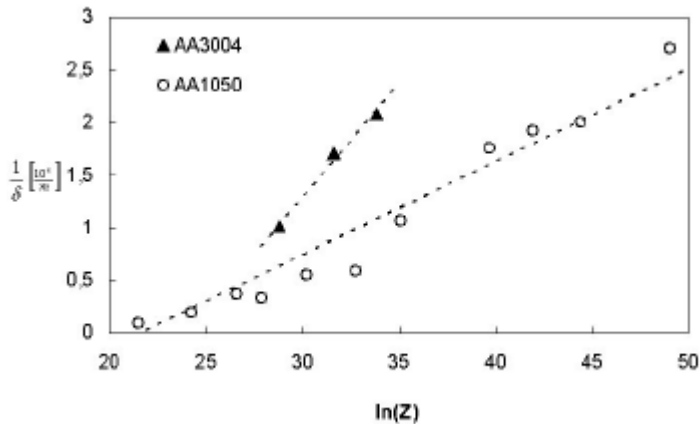


Fig 2.5: Subgrain size as function of $\ln(Z)$. (Nes and Furu (1995)) (Castro-Fernandez et al. (1990))

Similar behaviour was found by Glez and Driver (2003), testing aluminium single crystals of various orientations in plane strain compression. At constant temperature, the subgrain size was seen to decrease and stabilise with increasing strain or strain rate. However, the subgrain size was found to depend strongly on the orientation of the single crystal as shown in fig. 2.6.

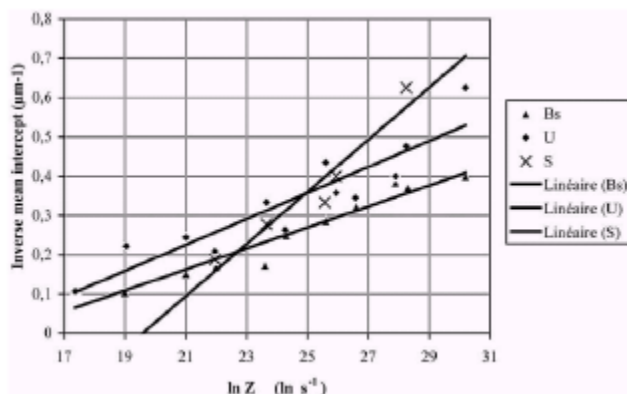


Fig 2.6: Inverse intercept length as function of Z for different orientations of single crystals in plane strain compression. (Glez and Driver (2003))

Dislocation density in the subgrain interior

The dislocation density in the subgrain interior is less documented, mainly due to a more complex and time-consuming technique. At low strains TEM-investigations have established the principle of similitude, stating $d\sqrt{r_i} = const$. However, at larger strains this principle is no longer valid. Measurements of dislocation density done by Nord-Varhaug et al. (2000) showed that for cold deformation the subgrain size converged towards saturation at strains larger than $\epsilon=0.2$. This is shown in fig. 2.7 Bardal et al. (1995) measured the dislocation density of plane strain compressed AA3004. They found that only about 10% of the stored energy was

due to the interior dislocation density. The rest was due to the subgrain boundaries.

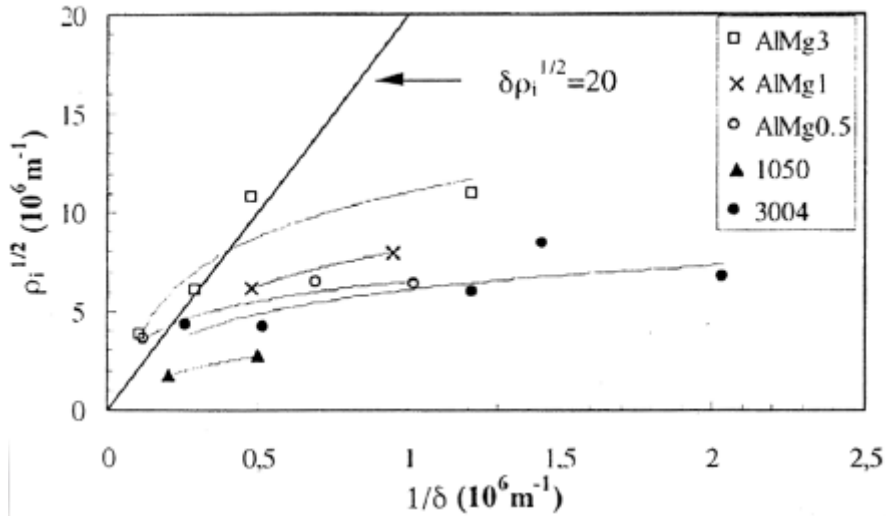


Fig 2.7: The square root of the internal dislocation density, plotted against the inverse subgrain size for different alloys after cold deformation. (Nord-Varhaug et al. (2000))

Subgrain misorientation

Furu et al (1995) measured the subgrain misorientation in TEM after various cold rolling reductions. The subgrain misorientation was found to increase up to a strain of $\epsilon=1$ and then stabilise between 2 and 3 degrees. The results are displayed in fig. 2.8.

These results were confirmed by Glez and Driver (2003) testing single crystals in hot plane strain compression, and measuring the subgrain misorientation in TEM. The average subgrain misorientation was found to depend on Z , stabilising at higher values at increased values of Z . As for the subgrain size, the misorientation was found to depend on the crystal orientation.

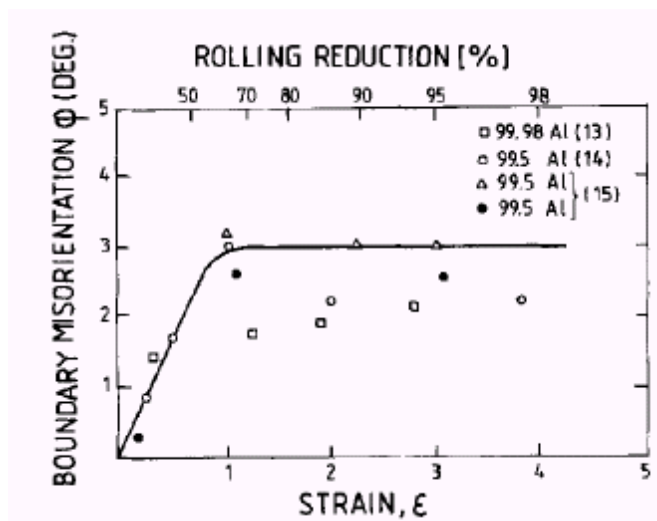


Fig 2.8 Subgrain misorientation after cold rolling to various strains. (Furu et al. (1995))

2.3.1 The effect of strain path changes on microstructure

Only a few studies of the effect of strain path on the deformation microstructure exist. In some studies of the Baushinger effect (Iyer and Gordon (1959), Hargreaves et al,(1963)), the stored energy was measured by calorimetry. These experiments indicated that the stored energy was reduced by reversed loading. Zhu and Sellars (1996) studied the effect of deformation paths on the development of microstructure in an Al-2Mg alloy deformed in tension and tension/compression at 300°C and a strain rate of $\dot{\epsilon}=0,1/s$. They found that the subgrain size was not affected by change in strain path, remaining constant at 1.6μm. However, both average subgrain misorientation and dislocation density inside subgrains was affected by changes in strain path. Deformation in tension/compression resulted in lower internal dislocation density, as well as a lower

misorientation, compared to monotonic deformation. These effects are shown in fig. 2.9.

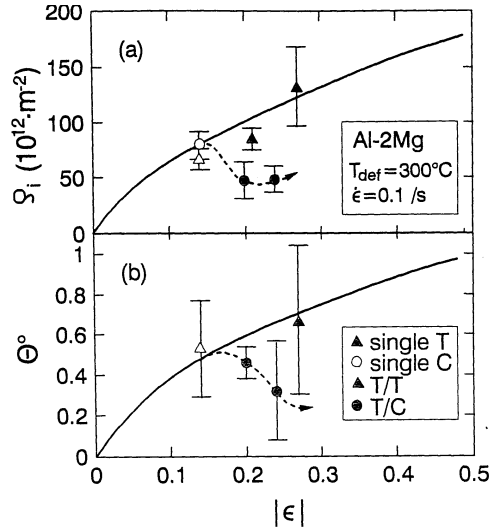


Fig 2.9: Internal dislocation density (ρ_i) and subgrain misorientation (θ) after deformation in tension (T), compression (C) and tension/compression (T/C). From Zhu and Sellars (1996)

Higginson and Sellars (2002) studied the effect on the microstructure from strain path changes during hot rolling of austenitic stainless steel. The strain path change was achieved by a two pass rolling schedule. Some of the samples were rolled in the reverse direction in the second pass (FR), while the rest was rolled in the same direction in both passes (FF). Fig. 2.10 shows the subgrain size and the free dislocation density for two position through the thickness of the slab, and for various accumulated strains. Taking the 95% confidence interval of the subgrain measurements into account, it is not possible to isolate any effect of strain path on subgrain size. For the free dislocation density, however, there seems to be a strain path effect near the surface. Here, the dislocation density is considerably higher for the samples rolled in a FF-schedule.

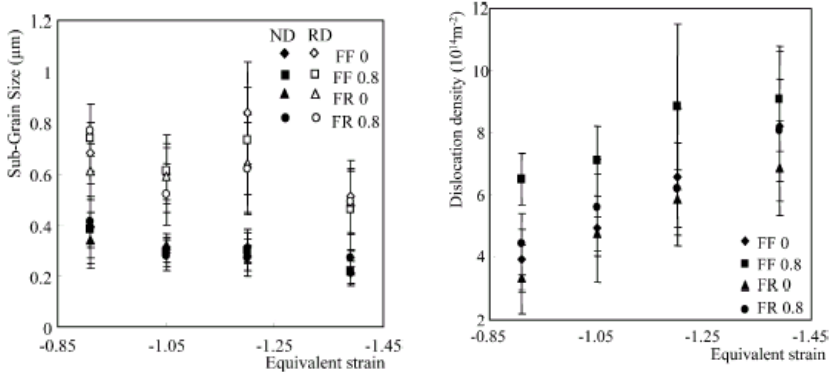


Fig 2.10: Subgrain size and free dislocation density in the rolling and normal direction against equivalent strain. From the centre of the slab (0) and from near the surface (0.8). Slabs rolled forward-forward (FF) and forward-reverse (FR). Higginson and Sellars (2002).

2.4 Modelling the evolution in mechanical properties during plastic deformation

To be able to predict changes of flow stress is of great value in all industrial processes. Traditionally such relationships have been established through empirical models, as the flow stress tend to change systematically with strain rate and deformation temperature.

2.4.1 Empirical relations

Based on extensive investigations of the steady state condition for creep and hot working, Sellars and McGregor Tegart (1972) introduced the following relationship between flow stress and deformation conditions:

$$\mathbf{s} = \frac{1}{\mathbf{a}} \text{Arc sinh} \left(\frac{\mathbf{Z}}{\mathbf{A}} \right)^{\frac{1}{n}} \quad (2.3)$$

Where \mathbf{a} , \mathbf{A} and \mathbf{n} are constants and \mathbf{Z} is the Zener-Hollomon parameter. The relationship of eq. 2.3 is widely used in the

modelling of metal forming processes such as hot rolling, forging and extrusion. The good fit between experimental observation and theoretical predictions is illustrated in fig. 2.11, where the saturation stress for two aluminium alloys tested in plane strain compression, are plotted as a function of Z . It should be pointed out, however that eq. 2.3 is a purely empirical relationship from which no basic physical mechanism can be inferred. This also applied to the selection of the activation energy, as this value defines the constants of the eq. 2.3. To illustrate this point; consider the plane strain compression results given in fig. 2.11: Although the results obtained for both alloys are well represented by eq. 2.3, it is not possible based on the result from one of these alloys, to predict the behaviour of the other, i.e. eq. 2.3 has no prediction power outside the alloy conditions tested.

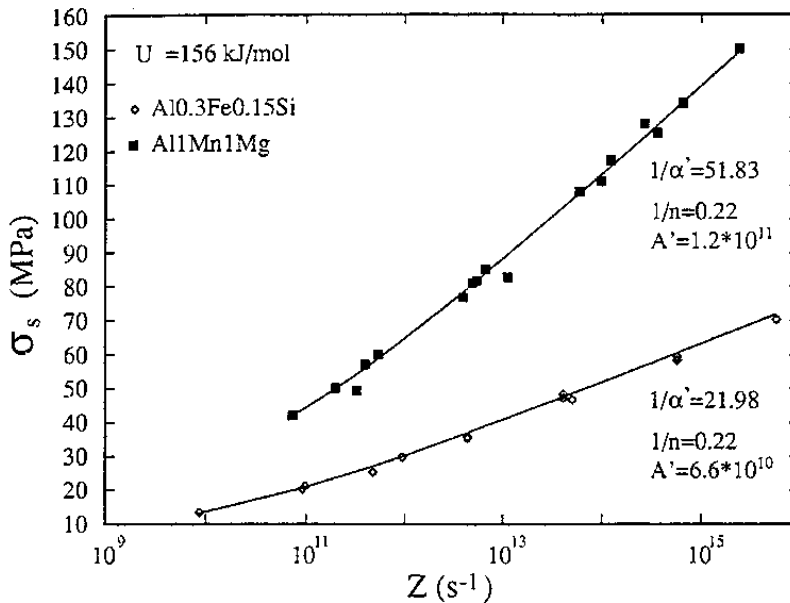


Fig 2.11: Steady state flow stress as function of the Zener-Hollomon parameter for the given alloys with the activation energy fixed at 156kJ/mol (Nes (1995a))

2.4.2 Physically based models

Work hardening is a complex problem, and the establishing of a physically based model and how to solve the problems are still matters of controversy. A common approach is to divide the problem into two. The first problem then relates to how to calculate the critical resolved flow stress for a given microstructure. The second problem is to explain how the deformation history produces this given microstructure. Different schools have approached these problems in different ways, where one major difference pertains to how to describe and characterise the microstructure. A classical approach is to rely on a one-parameter microstructural description. By one-parameter it is meant that during plastic deformation the flow stress is controlled by the average dislocation density (\mathbf{r}) in the material:

$$\mathbf{t} = \mathbf{t}_i + \mathbf{a}Gb\sqrt{\mathbf{r}} \quad (2.4)$$

where \mathbf{a} is a temperature dependent parameter. A one-parameter model for dislocation storage and dynamic recovery was introduced by Kocks (1976) and further refined by Mecking and Kocks (1981) and Estrin and Mecking (1984). For an extensive recent review, see Kocks and Mecking (2003). The way the dislocations are spatially organised, e.g. in cell structures, is not included in a direct way in such a description.

A more sophisticated approach to the problem of work hardening, as compared to the Kocks-Mecking model, is the model developed by Gottstein and co-workers (see e.g. Roters et al. 2000). It is based on a more realistic microstructure description with three internal state variables constituting a cell structure, namely a dislocation density in the cell interior, a dislocation density in the cell walls and a density of mobile dislocations. Their description is similar to that

introduced by Mughrabi (1987), and they use his composite model for the flow stress:

$$\mathbf{t} = \mathbf{t}_i + \mathbf{t}_p + (1-f)\mathbf{a}Gb\sqrt{\mathbf{r}_i} + f\mathbf{a}Gb\sqrt{\mathbf{r}_w} \quad (2.5)$$

Recently, Nes and co-workers have introduced a model for work hardening with similarities to both the models mentioned above (Nes 1998, Marthinsen and Nes 2001, Nes and Marthinsen 2002). It relies on a multi parameter description of the microstructure. The model predicts the evolution of subgrain size, subgrain misorientation and internal dislocation density as function of the deformation conditions. A detailed description of the model is given in chapter 10.3.

2.4.3 Texture

During plastic deformation of a polycrystal, each grain is subjected to stresses and strains as a consequence of the deformation. As a result, the grain changes its shape and orientation. The mechanism of plastic deformation is dislocation-induced slip. This does not produce lattice rotation by itself, rather it is the accommodation of the new grain to its surroundings which causes the change in orientation. Several models for texture development exist. For this work a short summary of the models by Sachs and Taylor is given. In FCC-metals, slip occurs on the $\{111\}\langle 110 \rangle$ slip systems during deformation at ambient temperature. At elevated temperatures slip may also occur on other slip planes.

The oldest model for polycrystalline deformation was proposed by Sachs (1928). In the original Sachs model, the stress in each grain was set equal to the macroscopic stress. Each grain also deforms independently of its neighbours, which means the strain and change in orientation are determined in the same way as for a free single crystal exposed to a stress. It is assumed that slip only takes place

on those slip systems where the resolved shear stress equals the critical resolved shear stress.

The Sachs model works relatively well for small strains. At larger strains however, its predictions no longer hold. The model then loses compatibility in strain, and open pores form between the grains. Taylor (1938) proposed a model which addressed the strain during deformation and neglected the external stress. The Taylor model is founded on three assumptions: (i) The strain in each crystallite is equal to the external strain, \mathbf{e}_{ij} . (ii) The plastic deformation occurs by means of poly-slip. (iii) The symmetric part of the strain tensor together with the law of the conservation of volume, give five linearly independent eq., which means that the prescribed strain can be accommodated by five independent slip systems. In the selection of the five slip systems the criterion of minimum internal work applies. The Taylor theory fulfils the requirement for compatibility in strain, but it violates the condition for equilibrium in stress. Several attempts have been made to modify these models, in order to improve their fit to experimental data. For the Taylor model, the shear may be relaxed in one or two planes i.e. the lath- and pancake model.

A closer look at texture development in hot rolling and torsion is given in chapter 9.4 and 3.5 respectively.

2.4.4 Texture and strain path

The effect of strain path changes on texture development has only been a subject of study for relatively short time, and only a limited number of studies exist. These studies are spread on a variety of materials and deformation modes. However, some information may be gathered from the studies. Rollett et al. (1988) studied the texture development in torsion and reversed torsion. After a full reversal to

zero net strain a weak shear component remained, even though the original grain shape was restored. Higginson et al. (2002) studied strain path changes in aluminium by combinations of free compression and plane strain compression, resulting in strain path changes of 0, 90° (two different), 120° and 180°. The starting material had a weak texture. The samples subjected to 0 and 180° strain path changes showed a weak texture after deformation, while 90° and 120° strain path change led to strong ND-rotated cube and somewhat weaker cube texture. Higginson et al. (2003) studied texture development as a function of roll pass schedule on through thickness texture development for two pass hot rolling of aluminium. A difference in strain path was obtained by reversing the rolling direction of some of the specimens between the first and the second rolling pass (FR), while the rest was rolled in the same direction in both passes (FF). The two rolling pass schedules resulted only in small textural differences. In the surface of the slab, the FF-sample showed stronger ND rotated cube texture compared to the FR-sample. For the positions 10% and 50% into the sample, no substantial texture differences were observed.

2.5 Annealing of deformed material

2.5.1 Introduction

During deformation of a metal, energy is stored in the evolving microstructure. Upon annealing, this energy is the driving pressure for the processes that transform the material into more energetically favourable microstructural states. The changes in microstructure causes softening of the metal. The purpose of annealing is usually to obtain better workability and ductility, and sometimes to obtain specific textures or grain structures. The initial stage of annealing is dominated by **recovery** reactions. In this stage, subgrain boundaries become sharper, subgrain interiors become nearly dislocation free and the subgrain structure is coarsening. In materials subjected to hot deformation, dynamic recovery is taking place and the effect of static recovery is usually small. Some softening takes place during recovery, but more important is the development of nuclei for **recrystallisation**. After nucleation of new grains, these will grow until the matrix is consumed. The recrystallisation process is treated in detail in the following chapters. After recrystallisation, further structural changes by **grain growth** may occur. The driving pressure for this reaction is the minimisation of the grain boundary energy. Grain growth is often important for the final grain size after annealing of steels, but for aluminium the reaction is usually less important.

2.5.2 Recovery of deformed material

In the beginning of the annealing process, softening occurs by dislocation annihilation and subgrain growth, before recrystallisation starts to progress. It should be noted that recovery and recrystallisation are competing processes as both are driven by

the same stored energy. It is also difficult to distinguish between recovery and the early stages of recrystallisation as recovery, by subgrain growth, is important for formation of nuclei for recrystallisation.

Recovery results in relatively small changes in the microstructure, and is usually divided into two stages; annealing of the statistically stored dislocations and subsequent subgrain growth. The magnitude of the recovery contribution to the softening reaction is dependent on the rate of recovery compared to the nucleation and growth rate of recrystallised grains. For aluminium a substantial proportion of the stored energy can be consumed by recovery, while for other metals like copper, recovery play no role in the softening process. This difference is due to the difference in stacking fault energy (I_{SFE}). Climb is the rate controlling mechanism of recovery and for metals with low I_{SFE} , like copper, climb is difficult. For metals with high I_{SFE} climb is much easier and extensive recovery can occur.

Dislocation migration in the early stages of annealing lowers the stored energy of the system, and this occurs by two processes; annihilation of dislocations with Burgers vector of opposite direction and rearrangement into subgrain boundaries. Both processes are activated by climb, glide and cross-slip of dislocations. As climb requires thermal activation, this can only occur at high temperatures. A similar configuration of screw dislocations would recover by annihilation of dislocations by cross-slip. This process may occur at lower temperatures in high I_{SFE} materials. During deformation, an unequal number of dislocations of opposite signs are produced, and these excess dislocations will rearrange into more stable low angle grain boundaries during annealing. The energy of a tilt boundary increases with misorientation, but the energy per dislocation decreases with

increasing misorientation. This means that there is a driving force to form fewer and more misoriented boundaries. An alternative mechanism to subgrain growth is coalescence, where two neighbouring subgrains rotate into the same configuration. This mechanism is only operating after small deformations.

The increase in subgrain size upon annealing has often been reported to follow the growth law in eq. 2.6, where d_0^n is the subgrain size in the as deformed condition.

$$d^n = d_0^n + kt \quad (2.6)$$

Much work has been done to determine the growth exponent (n). Varma et al. (1984, 1986, 1988) have repeatedly reported a n -value of 2, while Furu et al. (1995) have analysed their own experimental results as well as work by Sandstrøm et al. (1978) and found that a value of $N=4$ gives a better fit to the experimental results. Abtahi et al. (2001) found growth exponents varying from 2.6 at a annealing temperature of 400°C to 5.5 at a annealing temperature of 250°C.

2.5.3 Driving pressure for recrystallisation

The driving pressure for recrystallisation is the energy that is accommodated in the material during deformation. Plastic deformation introduces a variety of defects into the crystal lattice. These effects, along with elastic strains, serve as mechanisms for energy storage. The defects include dislocations, vacancies, interstitial atoms, stacking faults and twin boundaries. Of these, dislocations are the totally dominating energy source after deformation of aluminium. Dislocations in aluminium readily form a structure of subgrains with an internal dislocation network. Thus

the driving pressure is the sum of the stored energy associated with the subgrains and the internal dislocation network, given by:

$$P_D = r_i \Gamma + \frac{\mathbf{a} g_{SB}}{d} \quad (2.7)$$

where r_i is the dislocation density in the interior of the subgrains, Γ is the dislocation line tension ($\Gamma \sim Gb^2/2$), \mathbf{a} is a geometric constant ($\mathbf{a} \sim 3$), d is the subgrain size and g_{SB} is the energy of the subgrain boundary, given by the Read-Shockley relation:

$$g_{SB} = \frac{Gb}{4p(1-n)} \mathbf{q} \ln \left(\frac{e \mathbf{q}_c}{\mathbf{q}} \right) \quad (2.8)$$

where G is the shear modulus, b is the burgers vector, n is the Poisson ratio, \mathbf{q} is the angle of misorientation and \mathbf{q}_c is the critical radius for a boundary to be defined as a high angle boundary (of the order 15°).

Application of the Read-Shockley relation assumes a periodic, equiaxed substructure, which is a reasonable assumption for a hot deformed aluminium alloy. The following expression for the driving pressure is thus obtained:

$$P_D = Gb^2 \frac{r_i}{2} + \mathbf{a} \frac{Gb}{4p(1-n)} \frac{\mathbf{q}}{d} \ln \left(\frac{e \mathbf{q}_c}{\mathbf{q}} \right) \quad (2.9)$$

2.5.4 Effect of small particles during annealing of deformed material

A dispersion of small second phase particles will exert a restraining force on a moving boundary, having a retarding effect both on the

movement of low angle boundaries during recovery, and high angle boundaries during recrystallisation. As first recognised by Zener and Smith, and as published by Smith (1948), the interaction force from a single incoherent spherical particle on a grain boundary is given by:

$$F_z = 2pRg_{GB} \cos j \sin j \quad (2.10)$$

Where g_{GB} is the grain boundary energy, R is the radius of the particle and j is the angle at which the boundary meets the particle. The maximum pull of one particle may then be calculated:

$$F_z = pRg_{GB} \quad (2.11)$$

Since a part of the moving boundary is removed when the boundary meets the particle, the system lowers its energy by the particle/boundary configuration. The boundaries are hence attached to the particles, and the boundary bows out when it meets a particle. In a real metal, there is an array of particles. The pressure from this distribution of particles, commonly known as the Zener drag, was first estimated by (Smith (1948)) from a random distribution of particles.

$$P_z = ag_{GB} \frac{f}{R} \quad (2.12)$$

where f is the volume fraction of particles, R is the radius of the particles, g_{GB} is the grain boundary energy and a is a geometric constant. Thus, the effective driving pressure is then $P_D - P_z$. If the particle distribution is non-random, the effect on the microstructure might be quite different. This was demonstrated by Nes et al. (1985). As an example: If the particles are aligned in lamellar

bands, the growth rate will be direction dependant, and non-equiaxed recrystallised grain structure will be the result.

2.5.5 Nucleation of recrystallised grains

The normal process of recrystallisation of metals is the formation of small regions of nearly defect-free crystals (nuclei) and the growth of these into the surrounding deformed material. The critical size of a nucleus can be calculated by the Gibbs-Thompson Relation

$$d > d_c = \frac{4g_{GB}}{P_D} \quad (2.13)$$

Where d is the diameter of the deformation free volume, g_{GB} is the specific grain boundary energy and P_D is the stored energy. A grain fulfilling the requiriement of eq. 2.13 will grow with a growth rate G given by:

$$G = M \left(P_D - \frac{2g_{GB}}{R} \right) \quad (2.14)$$

where M is the mobility of the grain boundary. The concept of nucleation in recrystallisation is diffuse. However, a strain free grain of a size determined by eq. 2.14 is required in order to provide further growth. The process prior to this stage i.e. the nucleation reaction, requires growth or coalescence of subgrains/sub-boundaries. It follows that eq. 2.13 and 2.14 will determine the transformation and the evolution of the recrystallisation texture.

Bailey (1960) and others have emphasised that the driving force for recrystallisation is very small, and the critical nucleus size is thus quite large. The probability that so many atoms could be thrown together by random thermal processes is far to low for classical

homogenous nucleation processes to be of importance (Burke and Turnbull (1952)). Therefore, the potential nuclei must be found in the deformed structure. The central question then becomes: Which ones of the mass of potential nuclei available develop into recrystallised grains? The formal criterion was stated mathematically in eq. 2.13 and 2.14. In other words, what must be fulfilled by a successful grain are the criteria of stability and mobility. The first requires that the nuclei are thermodynamically stable at all stages of their development. A large number of crystallites are expected to fulfil this criterion. Therefore, the presumably most restrictive criterion relates to the boundary mobility. Most of the crystallites have small misorientations with their neighbours and low angle boundaries are known to be close to immobile. It is therefore essential for a successful nucleus to have, or rapidly achieve, a misorientation above the critical value to give high mobility. Thus, the places to search for nuclei in the deformed structure are the places where high angle boundaries already exist or might easily develop during annealing. The latter is especially favoured in microstructural heterogeneities with steep orientation gradients.

Nucleation at prior high angle boundaries

A pre-existing grain boundary can bulge out and create a strain-free volume which can continue to grow as a recrystallised grain. The mechanism of **strain induced boundary migration** (SIBM) was originally observed by optical microscopy by Beck and Sperry (1950) and later by electron microscopy by Bailey and Hirsch (1962). In this SIBM process a subgrain of one grain adjacent to a pre-existing high angle boundary grows by migration of that boundary, into the neighbouring grain. For this to happen, there must be a difference in stored energy on either side of the boundary

so that the grain of low dislocation density grows into that of high density and reproduces its original grain orientation.

Beck and Sperry (1950) also reported nucleation at grain boundaries where the new grain was separated from both its neighbouring grains by sharp boundaries. This was referred to as “**ordinary nucleation in grain boundaries**”. More recently, evidence for the operation of this mechanism has been obtained by Hutchinson (1989) who studied recrystallization in iron bicrystals. It was found that boundaries which separate grains having γ -fibre orientations ($\langle 111 \rangle_{\psi ND}$) gave rise to recrystallization textures, which were also within the γ -fibre. The new grains were typically found to differ in orientation from the original deformed grain by a rotation of $\sim 30^\circ$ around the $\langle 111 \rangle$ normal direction.

No evidence was found for zones of systematic lattice rotation existing adjacent to the grain boundaries. Hutchinson (1989) concluded that recrystallized grains formed in the vicinity of original grain boundaries develop from subgrain nuclei with sufficient deviation in orientation from the matrix to permit continued rapid growth.

Experiments reported by Vatne et al. (1995) have been carried out to investigate the nucleation of random oriented grains at grain boundaries compared to particle stimulated nucleation (PSN). Comparing cold rolled material with the same number of critically sized particles, but different initial grain sizes, it was found that smaller initial grain size gave smaller recrystallized grain size (with random recrystallization texture). Hence, these results indicate that nucleation at prior grain boundaries results in randomly oriented grains. Similar results were also found for hot deformed material, most explicit at higher temperatures, where PSN is expected to be less potent.

Deformation zones at particles

Since the famous works by Humphreys (1977, 1979) there has been a general consensus that particle stimulated nucleation (PSN) is one of the governing nucleation mechanisms in commercial alloys containing large particles. The deformation zones are areas of high stored energy and a progressive lattice rotation from the remote matrix to the particle surface. Due to the favourable growth conditions within the zones, the critical stage is not the consumption of the deformation zone itself, but the growth into the less highly strained and misoriented matrix. Although the crystallites which become nuclei can probably exist anywhere within the deformation zone (Humphreys (1977), Ørsund and Nes (1988)), the ultimately successful ones will normally lie close to the particle surface since these have the high misorientation necessary for growth into the matrix.

The strain and the particle size are the most important parameters, influencing the presence PSN. This may be seen in Fig. 2.16, showing experiments carried out on a AlCuSi-alloy (Humphreys (1977)). During low temperature deformation the energy stored in the deformation zones is relatively large. The critical step in the nucleation process is then the growth of new grains after the deformation zone has been consumed. Successful nucleation requires a deformation zone larger than a critical value (I_c) As the size of the deformation zone depends on the particle size, the requirement for nucleation may be expressed by a critical particle diameter ($h_c = I_c/3$). The critical size of the deformation zone for successful growth out of the deformation zone is given by (Nes (1980)):

$$I_c = 3h_c = \frac{4g_{GB}}{(P_D - P_Z)} \quad (2.15)$$

where P_D is the driving pressure due to stored energy in the matrix, P_Z is the Zener drag due to small dispersoid particles and g_{GB} is the high angle boundary energy.

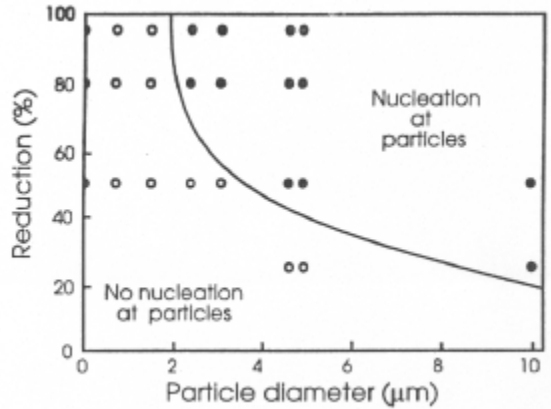


Fig 2.12: The effect of particle size and rolling reduction on particle stimulated nucleation (Humphreys (1977)).

During high temperature deformation, annihilation of dislocations will prevent formation of a deformation zone at the smaller particles. For this situation Humphreys and Kalu (1987) proposed that deformation zones will only be formed at particles larger than h_c , given by:

$$h_c = K (TZ)^{-\frac{1}{3}} \quad (2.16)$$

where K is a constant and Z is the Zener-Hollomon parameter. Eq. 2.13 is a formation criterion that comes in addition to the growth criterion of eq. 2.12 for PSN to be successful. The growth criterion is, as in the case of cold deformation the most important for those Zener-Hollomon parameters that are normally obtained during hot rolling. This is shown in fig. 2.13.

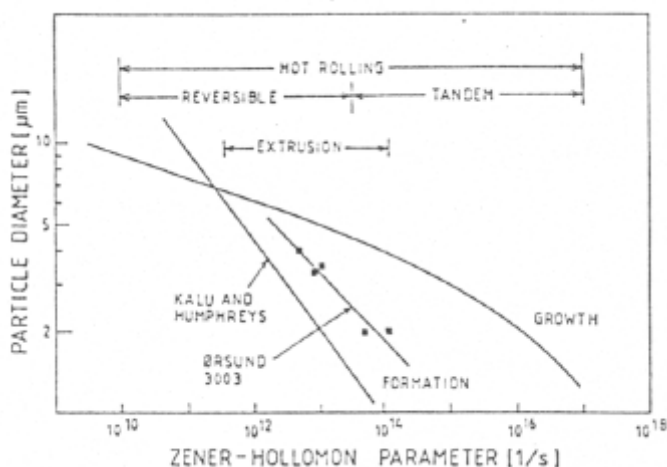


Fig 2.13: The effect of the Zener-Hollomon parameter on the formation and growth of nuclei formed at particles, (Furu et al. (1993)).

Nucleation at transition bands

A characteristic feature of a transition band is a sharp orientation gradient bridging two neighbouring regions of different texture components. Hence, a subgrain in the transition band can easily gain a boundary of high misorientation by growing into the surrounding areas. The orientation of the subgrains in the transition band is a result of the slip process and the strain path, and hence it is often found that the grains nucleated at transition bands have special orientations. A well-known example of this is the prediction of transition bands of Cube orientation during plane strain deformation of high stacking fault energy fcc metals. Ridha et al. (1982), Dons et al. (1986) and Hjelen et al. (1987) confirmed experimentally that Cube oriented grains nucleated from transition bands in copper and aluminium. Also other orientations have been found to nucleate at transition bands, and Hjelen et al. (1987) found Goss-oriented grains nucleated from transition bands in aluminium.

It is not quite obvious how the nuclei of recrystallization are formed within the transition band. The subgrains in transition bands are often found to be elongated as shown schematically in fig. 2.14.

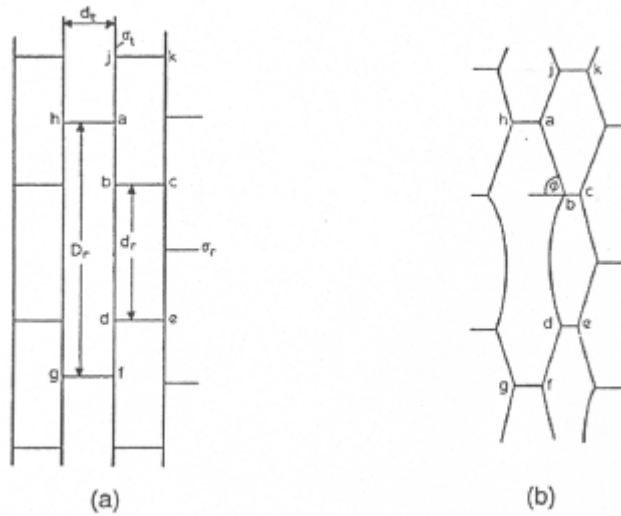


Fig 2.14: Sketch illustrating the model for subgrain growth in transition bands. a) as deformed microstructure with elongated subgrains, b) the microstructure after annealing. (Dillamore et al. (1972)).

Based on this geometry, Dillamore et al. (1972) proposed a mechanism for nucleation at transition bands. When annealing a material of elongated subgrains, the subgrains are assumed to relax to comply with the equilibrium forces at the sub-boundary junction. A critical condition that would allow the continued growth of the large subgrain a-h-g-f-d-b would be if b and c came into contact before this equilibrium angle was achieved. This would occur if:

$$D_r > \frac{4}{3} \left(d_r + d_t \left(\frac{4\mathbf{s}_t^2}{\mathbf{s}_r^2} - 1 \right)^{\frac{1}{2}} \right) \quad (2.17)$$

that is, if the particular subgrain is sufficiently long compared to the average transition band subgrain, the particular subgrain will act as a nucleation site for recrystallisation. The nuclei will grow both in the r- and t-directions, the latter case being where the misorientation between the nuclei and its surroundings is continuously increasing, creating an increasing mobility of the grain boundary. However, as pointed out by Doherty (1978) the question of how the over-critical subgrain may have achieved the length D_r is left open. One suggestion is that over-critically sized subgrains could be formed by subgrain coalescence of two or more subgrains. However, Smith and Dillamore (1970) reported that predictions of coalescence kinetics gave a subgrain development rate that was several orders of magnitude less than what is actually observed. This suggests that nucleation through general subgrain growth by boundary migration is the fastest process. This further means that the nucleation might take place solely by subgrain boundary migration.

Nucleation at shear bands

The structure that appears when deformation becomes localised into a shear band should be ideal for the nucleation of recrystallisation. Since no orientation is truly stable in shear, there is a large possible range of spin angles resulting in large misorientations towards the surroundings. Due to low local stored energy with large subgrains within the bands, growth might easily take place. Since the mechanism was first purposed by Adcock (1922), it has been disputed and its importance has not been proved. Nucleation from shear bands has been seen result in various orientations. In steel, Goss oriented grains have been identified by Ushioda et al. (1981), in aluminium the R orientation has been suggested by Hjelen et al. (1991). Engler et al. (1995) correlated the occurrence of Goss Q- and the P-orientation to shear bands in aluminium.

Nucleation from Cube-oriented bands present in the starting material

Investigation of hot deformed aluminium alloys have demonstrated that the Cube orientation may be nucleated from Cube grains that are present in the starting material, remaining orientation stable during deformation. (Weiland and Hirsch (1990), Daaland (1993), Daaland and Nes (1996a-b), Vatne (1995), Vatne et al. (1996a-d). The Taylor theory provides theoretical support for such a mechanism, predicting metastability of the Cube orientation during rolling. As shown by Dillamore and Katoh (1974), this metastability is due to rotations around the normal direction into the Cube orientation and rotations around the rolling direction out of the Cube orientation. In the experimental investigations by Daaland (1993), Daaland et al. (1996a-b), Vatne (1995) and Vatne et al. (1996a-d) the original Cube grains were found to change shape during deformation, forming long elongated bands of the Cube orientation. The subgrains within the Cube-bands were also seen to have a size advantage compared to subgrains of other orientations, probably due to a higher recovery rate in the bands of Cube orientation. This makes the Cube-bands very efficient as nucleation sites. Nucleation at prior Cube-grains is schematically illustrated in fig. 2.15.

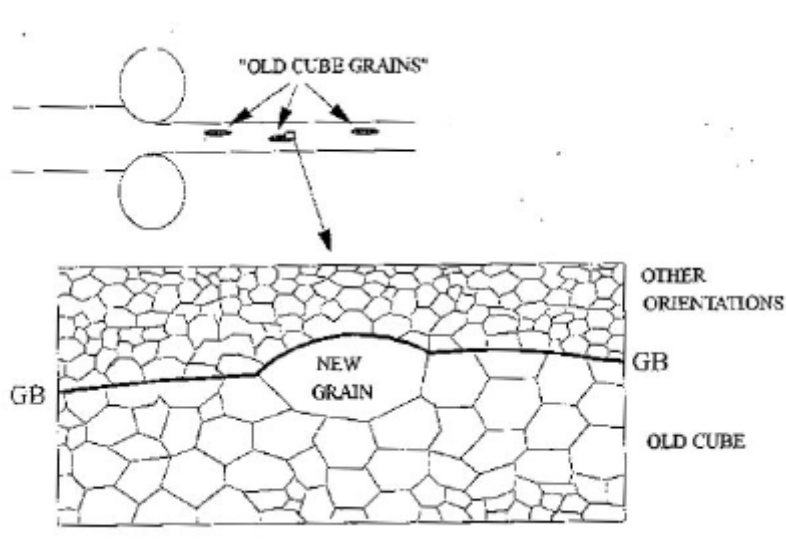


Fig 2.15: Schematic illustration of the nucleation of Cube-oriented grains from grains of the Cube orientation present in the starting material. (Vatne, (1995)).

2.5.6 Recrystallisation kinetics

The kinetics of recrystallisation are a function of the nucleation rate and the growth rate. Both quantities are in general expected to vary within the material and with transformation time. With the basic assumption of a constant isotropic growth rate and a random spatial distribution of nucleation sites, the JMAK theory (Johnson and Mehl (1939), Avrami (1939) and Kolmogorov (1937)) predicts the following simple relationship between the volume fraction of transformed material, X , and the annealing time t :

$$X_v = 1 - \exp(-kt^n) \quad (2.18)$$

where k and n are constants. The latter referred to as the Avrami exponent. The Avrami exponent depends on the nucleation rate. For some idealised nucleation conditions, the Avrami exponent has been calculated. Assuming site saturation – all the nuclei are present

from the start – the Avrami exponent is found to have the value of 3. Given nucleation at a constant rate, the Avrami exponent is found to be 4. In aluminium alloys the Avrami exponent is commonly found to scatter around 2 when measured experimentally. (Daaland (1993)). Relaxations of the JMAK theory have been undertaken by Furu et al. (1990) who incorporated both a non-homogenous distribution of nucleation sites and a decreasing growth rate due to both recovery and an inhomogeneous distribution of stored energy. This resulted in a lower Avrami exponent than in the classical approaches.

Gokhale and DeHoff (1985) developed a stereological approach to obtain the nucleation frequency. Vandermeer and Rath (1989) used this methodology in order to determine the nucleation rate in iron single crystals deformed to 70% by cold rolling. The same approach was used by Daaland (1993) for a hot rolled AlMgMn alloy. Their results showed that almost all the nucleation positions were activated within a short time compared to the time for transformation i.e. site saturation applies. In this case, eq. 2.15 takes the form

$$X(t) = 1 - \exp\left[-\frac{4}{3}pN(Gt)^3\right] \quad (2.19)$$

where N is the number of nucleation sites per unit volume and G is the growth rate given by:

$$G = M(P_D - P_Z) \quad (2.20)$$

where

$$M = \frac{M_0}{RT} \exp\left(-\frac{U_{GB}}{RT}\right) \quad (2.21)$$

is the temperature dependent mobility of the recrystallisation front, P_D is the driving pressure for recrystallisation given in eq. 2.9, P_Z is the Zener drag M_0 is a constant U_{GB} is the activation energy for grain boundary migration, T is the annealing temperature and R is the universal gas constant.

2.5.7 Recrystallisation and strain path

The research on strain path effects on subsequent recrystallisation was motivated by the knowledge that recrystallisation behaviour was not related only to the total strain during deformation. The most apparent example is the subsurface regions in hot rolling, which are affected both by shear, reversed shear and plane strain compression. For the development of quantitative recrystallisation models, knowledge of such effects is vital for correct prediction of recrystallisation microstructures.

Lindh et al. (1993) studied recrystallisation in copper specimens deformed in various combinations of tension and tension/compression. For samples deformed to the same net strain, the recrystallisation temperature was found to be lower for samples deformed in tension, compared to samples deformed in tension/compression. During deformation, the samples deformed in tension/compression showed permanent softening. If the recrystallisation temperature was plotted against the final flow stress, no differences in recrystallisation temperature was found between deformation in tension and tension/compression. Reduced stored energy after cyclic deformation was therefore seen as the reason for the difference in recrystallisation behaviour after tension and tension/compression. Cowan et al. (1995) studied

recrystallisation in aluminium after the following deformation modes: Torsion, torsion/reversed torsion, compression and torsion/compression. The recrystallisation kinetics after torsion/reversed torsion were found to be significantly slower than after the other deformation modes, and the recrystallised grain size was found to be larger. Reversal of the torsion direction resulted in a lower flow stress, compared to monotonic torsion. Anyhow, the magnitude of the flow stress reduction was not of sufficient size to explain the large shift in recrystallisation kinetics. In contrast to the effect of torsion/reversed torsion, the combined torsion/compression did not result in slower recrystallisation kinetics. Zhu and Sellars (1996) studied the recrystallisation in Al-2Mg after tension/tension and tension/compression. Again, strain reversals was found to slow down recrystallisation kinetics and increase the recrystallised grain size. The samples deformed in tension/compression were found to have lower final flow stress. They also displayed a lower dislocation density inside subgrains and lower average subgrain misorientation, implying lower driving pressure for recrystallisation. Still, calculations of recrystallisation kinetics based on flow stress showed that the difference in stored energy could not explain the difference in recrystallised grain size or recrystallisation kinetics. Deviation from site saturation after tension/compression was suggested as a possible explanation for this deviation. Higginson et al. (2002) deformed Al-1Mg in combinations of plane strain compression and free compression resulting in strain path changes of 0° , 90° (two different ways), 120° and 180° . The samples subjected to 120° and 180° strain path changes, both showed retarded recrystallisation kinetics and larger recrystallised grain size than the sample with no change in strain path. The two samples that underwent a 90° strain path change behaved differently upon recrystallisation. One of the samples showed recrystallisation kinetics and grain size similar to the sample with no strain path change. The other sample showed

retarded kinetics and increased recrystallised grain size, although to a smaller degree than the samples subjected to 120° and 180° strain path changes. Difference in local (affecting nucleation) and global (affecting growth) stored energy was given as explanation for the differences in the recrystallisation.

2.5.8 Recrystallisation textures

The work on the understanding of recrystallisation textures has been characterised by a debate between two rival theories; oriented nucleation and oriented growth.

Oriented nucleation

Oriented nucleation implies that the recrystallisation texture is determined by the orientation of the nuclei. The theory originates from Dehlinger (1928) and Burgers and Louwse (1931), and has later been modified by Doherty (1985). The theory of oriented nucleation is based on that grains of the orientation dominating the recrystallised texture nucleate more frequently than grains of other orientations. Taking nucleation of random grains into account, normalisation of the fraction of grains of a specific orientation (\mathbf{a}_{tex}) by the fraction of random oriented grains (\mathbf{a}_{ran}) is required. Achieving a strong texture by oriented nucleation then requires that: $\mathbf{a}_{tex}/\mathbf{a}_{ran} \gg 1$.

Oriented growth

The theory of oriented growth was originally purposed by Barret (1940), followed by further development by Lücke (1984) and Hu (1986). The theory assumes the formation of a wide spectrum of nuclei orientations. The nuclei with the best growth conditions with respect to the microstructure will dominate and determine the recrystallisation texture. The oriented growth factor (\mathbf{b}) is determined by the relative size of the given texture to the average

grains. For an oriented growth effect to be present, it is required that $b = d_{tex}/d_{ran} \gg 1$. Today it is widely accepted that neither of the theories is capable of explaining all observed effects. Thus, recrystallisation textures are most probably determined by a combination of both mechanisms.

2.5.9 Recrystallisation models

Numerous recrystallisation models have been developed during the latest 30 years. A review is beyond the limits of this work. For this study, the model developed by Vatne (1996 a-d) will be used. The model was originally developed for hot rolling, but has been modified for hot torsion by Pettersen and Nes (2003a). The model will be described in detail for the two deformation modes in their respective sections of the thesis. (6.4 and 10.4)

The model proposed by Vatne is physically based, and calculates the recrystallised grain size and texture by prediction of the number of nuclei of various orientations present in the as deformed material. The random nuclei are supposed to originate from deformation zones surrounding particles, or from old grain boundaries. The cube texture component is assumed to originate from old cube grains surviving the deformation. The model has successfully been applied to predict recrystallisation behaviour after single pass plane strain compression, and industrial multipass hot rolling.

Chapter 2: General theoretical background

Part II: Strain path effects on recrystallisation after hot torsion

3 Theoretical background

3.1 Monotonic and cyclic torsion – concept and definitions

The use of cyclic and monotonic torsion is a good way of investigating strain path effects, as it enables reaching the same accumulated strain along clearly different strain paths. In monotonic torsion, the strain increase is always in the same torsional direction. In cyclic torsion the direction is reversed, returning the specimen to the original position for every second torsion step. In this investigation a strain step of $e=1.8$ is used, which equals one full rotation for the current sample geometry. For the description of the strain states in cyclic and monotonic torsion, two different notations of strain are being used, labeled **net strain** and **accumulated strain**. The difference between the two is described in fig. 3.1 showing cyclic and monotonic torsion with strain increments of $e=1.8$.

Net strain monotonic	$\epsilon = 1,8$	$\epsilon = 3,6$	$\epsilon = 5,4$	$\epsilon = 7,2$
Accumulated strain	$\epsilon = 1,8$	$\epsilon = 3,6$	$\epsilon = 5,4$	$\epsilon = 7,2$
Net strain cyclic	$\epsilon = 1,8$	$\epsilon = 0$	$\epsilon = 1,8$	$\epsilon = 0$

Fig 3.1: Definitions of net- and accumulated strain in monotonic and cyclic torsion.

As seen from the figure the accumulated strain refers to the sum of strain applied to the sample regardless of strain path changes. The net strain refers to the strain calculated from the final position of the sample, relative to the starting position. Thus, for monotonic torsion net- and accumulated strains are equivalent. In cyclic torsion the net strain is zero for every second torsion step, while the accumulated strain develops as during monotonic torsion.

3.2 Mechanical properties

3.2.1 Notation of orientations

In fig. 3.2 the geometry of the torsion sample is shown, with shear directions as well as the definition of orientations.

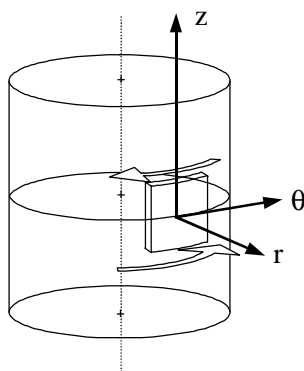


Fig 3.2: Notation of directions of torsion specimens. From Pettersen (2003b)

3.2.2 Calculation of stress, strain and strain rate

In order to calculate the stress, strain and strain rate data, the measured values of the torque, the angle of twist and the angular velocity are needed in addition to the geometry of the specimen. Considering a cylindrical bar of length L and a circular cross section of radius r subjected to a total angle of twist \mathbf{q} , the shear strain and the shear strain rate is given by:

$$\mathbf{g} = \frac{r}{L} \mathbf{q} \quad (3.1)$$

$$\dot{\mathbf{g}} = \frac{r}{L} \frac{d\mathbf{q}}{dt} = \frac{r}{L} \mathbf{w} \quad (3.2)$$

The shear stress has to be calculated from the measured torque, and a method to do this was proposed by Fields and Backofen (1957). Using this method, a solid cylindrical bar of outer radius $r=a$ is considered that is deformed to an angle of twist \mathbf{q} at an angular velocity \mathbf{w} , giving a torque $\mathbf{G}(\mathbf{q}, \mathbf{w})$. It is found that, when assuming that \mathbf{w}/\mathbf{q} is constant, the shear stress in the outer fibre, \mathbf{t}_a can be expressed by the following relationship:

$$\mathbf{t}_a = \frac{\Gamma}{2pa^3} \left[3 + \left(\frac{\mathcal{J}(\ln \Gamma)}{\mathcal{J}(\ln \mathbf{q})} \right)_w + \left(\frac{\mathcal{J}(\ln \Gamma)}{\mathcal{J}(\ln \mathbf{w})} \right)_q \right] \quad (3.3)$$

Introducing the parameters $p = \mathcal{J}(\ln \Gamma) / \mathcal{J}(\ln \mathbf{q})|_w$ and $q = \mathcal{J}(\ln \Gamma) / \mathcal{J}(\ln \mathbf{w})|_q$ gives the simpler expression:

$$\mathbf{t}_a = \frac{\Gamma}{2pa^3} (3 + p + q) \quad (3.4)$$

Hence, to find the shear stress the values of p and q have to be found first. In the present investigation the steady state value or the peak value of the torque has generally been used, hence $p=0$. The value of q has to be found from experimental data. Systematic experiments to determine q have not been carried out in the present investigation, however, an estimate of the value of q can be found on the basis of previous experiments, *e.g.* Rønning (1998) and

Rønning et al. (1998). It was found by Rønning (1998) that at low torques the value of q is constant, changing to decreasing values at higher strains. The value of q used in the present investigation is 0.19.

By using the von Mises criterion, the shear-stress and shear-strain data are converted to equivalent stress and strain by the following equations:

$$\mathbf{e} = \frac{\mathbf{g}}{\sqrt{3}} \quad \dot{\mathbf{e}} = \frac{\dot{\mathbf{g}}}{\sqrt{3}} \quad (3.5)$$

$$\mathbf{s}_a = \sqrt{3}\mathbf{t}_a \quad (3.6)$$

3.3 The stress-strain curve

3.3.1 Monotonic torsion

The mechanical properties of aluminium in torsion have been investigated by McQueen et al. (1985,1989), Kassner et al (1987, 1989) Montheillet et al. (1984) and Pettersen (1999). The recorded stress-strain curves are normally described by the following characteristics: A rapid initial rise of the flow stress to a peak value, followed by a gradual decrease in flow stress to a steady state plateau. Thus the stress strain curve is characterised by the following parameters: The value of the strain where the peak flow stress is reached (\mathbf{e}_p). The value of the peak flow stress. The value of the strain where the stress has reached its final steady state (\mathbf{e}_{ss}) and the total fall in the flow stress. In fig 3.3, flow curves recorded by Pettersen (1999) shows the development with Zener-Hollomon parameter. It is clear that the initial peak and the following decrease

are most prominent at high values of the Zener-Hollomon parameter.

Several reasons for the fall in the stress-strain curve has been suggested, such as:

- (i) Texture changes causing a reduction in the overall Taylor factor
- (ii) Microstructural changes, such as increase in cell or subgrain size.
- (iii) A change in operating deformation mechanism, due to the dramatic increase of the fraction of high angle grain boundaries with strain.

Pettersen (1999) investigated these proposed explanations, and made the following discoveries: Texture development was monitored in the decreasing part of the stress-strain curve. It was found that although the texture shifts towards a lower Taylor factor with increasing strain, this change is not in step with the change in flow stress. By the time the flow stress reaches the steady state, the texture change could not account for more than a fall in flow stress of about 5-7%, less than the half of the observed drop. The experimentally observed change in subgrain size was found to account for a fall in flow stress of approximately 10%, and thus was not fully sufficient for explaining the observed fall of about 20%. Even if a large fraction of high angle boundaries was present at large strains, no evidence was found for the occurrence of either grain boundary sliding or “diffusional creep” under the present conditions.

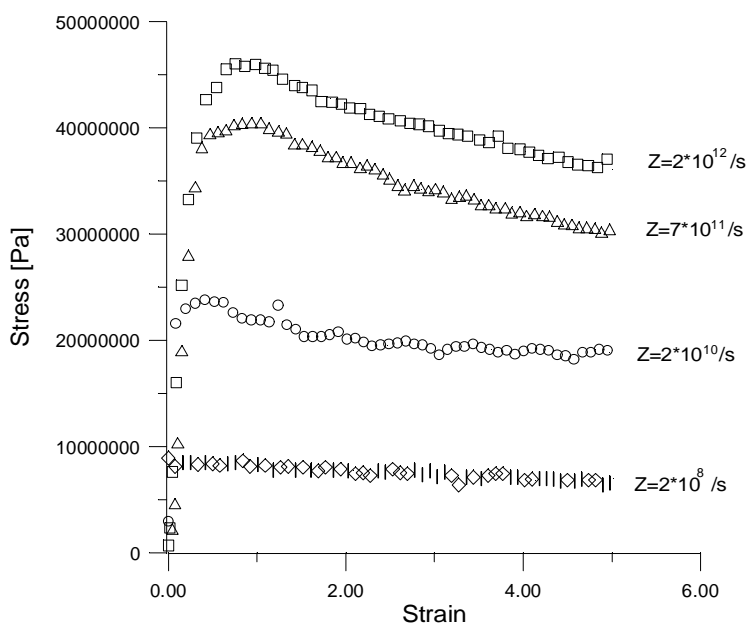


Fig 3.3: Stress strain curves for 6060 material deformed at different values of the Zener-Hollomon parameter. From Pettersen (1999)

However, the softening after an initial peak is not always observed. Mousavi (1995) recorded the flow stress in torsion for AA3003 subjected to two different homogenisation treatments. The results are shown in fig. 3.4. One of the homogenisation treatments (B1) resulted in a distribution of large particles. Samples deformed in torsion after this homogenisation treatment showed a stress strain curve with no strain softening. On the other hand, a homogenisation treatment, giving a high dispersoid density (B2) resulted in a stress strain curve showing an initial maximum and subsequent softening. No explanation was given for the homogenisation-dependent flow stress behavior.

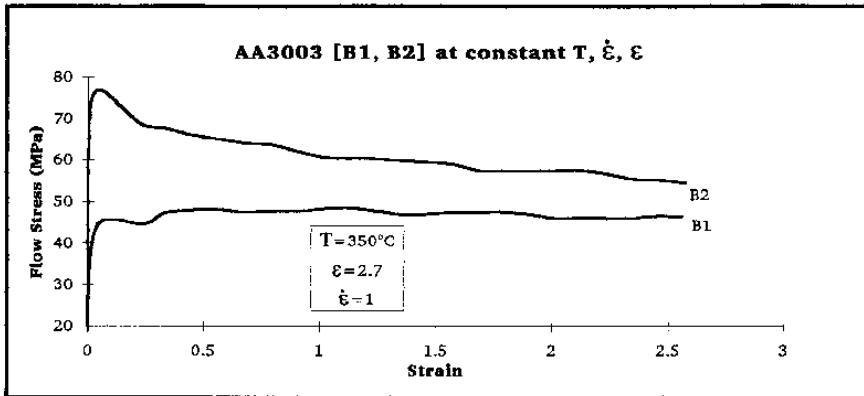


Fig 3.4: Stress strain curves for AA3003 after two different homogenisation treatments. (Mousavi (1995))

3.3.2 Cyclic torsion

Studies of the stress-strain relationship in cyclic torsion are normally associated with studies of the Bauschinger effect. Because of the large strains used in this work, only large strain Bauschinger effects are of interest. Stout and Rollett (1990) studied the large strain Bauschinger effects in torsion for a variety of fcc metals and alloys, using short and thin walled samples. Different mechanisms of the Bauschinger effect were proposed for the different microstructures. The alloys that deformed by wavy slip, were characterized by a flow stress after strain reversal, close to that of monotonic torsion, followed by a section of slow hardening or even strain softening. At larger strains the flow stress again reached the value equal to monotonic deformation. (fig. 3.5a) These alloys showed a dislocation structure consisting of cell walls of different morphologies after monotonic torsion. The Bauschinger effect in these alloys was explained as untangling of the cell arrangements explaining the plateau region of the flow stress, subsequent to strain reversal.

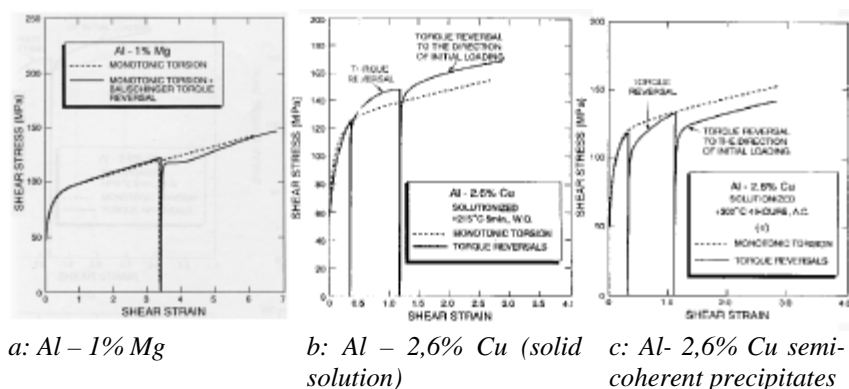


Fig 3.5: Stress strain curves in cyclic- and monotonic torsion at room temperature. Stout and Rollett (1990)

Al-Cu solid solution materials and Al-Cu heat-treated to produce coherent precipitates and GP-zones deform by planar glide. The stress-strain curves in cyclic torsion for these alloys were characterized by larger flow stresses after reversal of the direction of the stress, compared to continued monotonic torsion to the same accumulated strain (fig 3.5b). Work hardening in these alloys was seen as an effect of debris from intersection of gliding dislocations, resulting in permeable barriers to dislocation motion. Because of the small number of dislocations in the pileups, flow stress quickly attains the same level as in monotonic deformation. With reverse plastic deformation, slip is activated on secondary systems, which results in higher degree of generation of debris compared to monotonic torsion. This results in stress levels after reversal, larger than those obtained in monotonic torsion to equivalent accumulated strain. In the overaged Al – Cu alloys containing hard particles the flow stress returned almost to the initial value for the undeformed material. (Fig 3.5c) During deformation, the particles cause pileups of large numbers of dislocations. When the direction of stress is reversed, these pileups are removed and the flow stress drops considerably.

3.4 Microstructural development

3.4.1 Grain shape – spacing between high angle boundaries

Knustad et al. (1985) considered the following case: Straining a hypothetical surface grain of cubic shape in torsion, the grain is sheared into a spiral grain of constant section in the $r\mathbf{q}$ -plane. Considering the special geometry of a torsion sample and assuming constant volume of a grain during deformation, the following relationship was suggested to describe the change in grain width with strain:

$$D_z = \frac{D_0}{\sqrt{3} \cdot \bar{\epsilon}} \quad (3.7)$$

Where D_0 is the initial grain size. However, during deformation at large values of the Zener-Hollomon parameter the distance between high angle boundaries will decrease much faster than predicted by the equation. Thus, new high angle boundaries are formed during torsion. At low values of the Zener-Hollomon parameter, the distance between high angle boundaries may be larger than predicted by eq. 3.7. Both these situations were observed by Pettersen et al. (2003) as shown in fig. 3.6. The figure also includes the calculated drop in distance between high angle boundaries calculated from the geometric shape change of the grains as well as a calculation including grain break up.

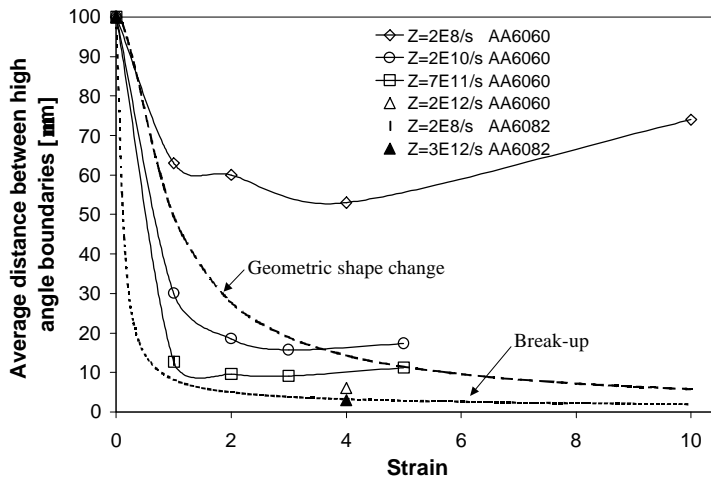


Fig 3.6: Average distance between high angle boundaries, compared to the expected value calculated from eq. 3.7, and from a model including break up effects. (Pettersen et al. (2003))

3.4.2 Subgrain size

The development of the microstructure during deformation in torsion mostly follows the same general trends as described in chapter 2. However, at medium torsional strains, subgrain growth has been observed during deformation. Pettersen and Nes (2003b) reported increase in subgrain size with strain in the decreasing part of the stress-strain curve. In constant second steady state, the subgrain size remained constant as shown in fig 3.7. The same phenomena was observed by Perdrix et al. (1981) observing increase in subgrain size from a value of $3.5 \mu\text{m}$, found at the peak of the flow curve, to a value of $4.8 \mu\text{m}$ found in the second steady state region. However, the increase in subgrain size is not of sufficient magnitude to explain the fall in the flow curve. Neither was any mechanism suggested for the increase in subgrain size.

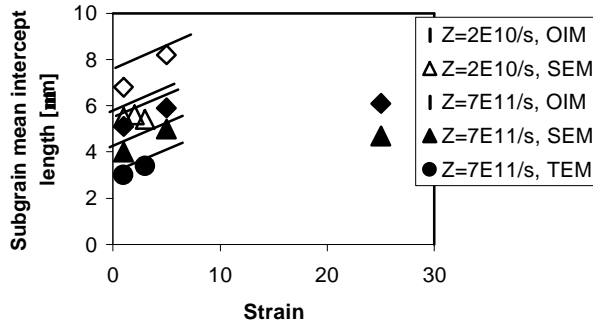


Fig 3.7: Subgrain size as function of torsional strain. (Pettersen and Nes (2003b))

3.5 Texture development

3.5.1 Monotonic torsion

Texture development in monotonic torsion has been studied by Montheillet et al (1984), Solberg et al. (1989), McQueen et al. (1989) and Pettersen (1999). Their investigations have revealed similar results, regarding texture evolution with strain. The reported torsion textures consists of the components listed below.

$$(A^1) \{1\bar{1}\bar{1}\} \langle 110 \rangle \text{ and } \{\bar{1}11\} \langle \bar{1}\bar{1}0 \rangle$$

$$(A^2) \{\bar{1}11\} \langle 112 \rangle \text{ and } \{11\bar{1}\} \langle 112 \rangle$$

$$(B^1) \{\bar{1}12\} \langle 110 \rangle \text{ and } \{1\bar{1}\bar{2}\} \langle \bar{1}\bar{1}0 \rangle$$

$$(C) \{001\} \langle 110 \rangle$$

The A^1 component is reported by Montheillet et al. (1984) only after torsion at room temperature to very small strains ($\epsilon=0.62$). Increasing the strain results in weakening of the A^1 component, and increase of the C component. During hot torsion the amount of B^1

component increased with total strain and temperature, while C- and A²-component decreased. This behavior is also seen in copper specimens. The same trend was reported by Solberg et al. (1989), except for that the A¹ component was observed instead of the A² component. Relatively strong C- and A²-components were reported after small strain ($\epsilon=3$). Pettersen (1999) observed that the A² component rapidly decreased in intensity with increasing strain in hot torsion. The C component increased in strength up to a strain of $\epsilon=3$ and then decreased rapidly. The B¹ component showed a continuous increase with strain, and dominated the texture from strains $\epsilon>10$.

3.5.2 Cyclic torsion

The studies of texture development in cyclic torsion are more limited. Backofen (1950) discovered that although the grain shape was restored after one full torsion cycle, a residual texture component remained. Rollett et al. (1988) confirmed Backofen's results, reporting textures from one torsion cycle. After a rotation to a strain of $\epsilon=3.5$ the texture consisted of mainly of the B fiber, with a weak A fiber. After reversal to zero net strain, only a weak C component remained. Vatne et al. (1996) observed weaker textures in cyclic torsion, compared to monotonic torsion to the same net strain. Still, after zero net strain a weak shear component was left.

3.5.3 Modelling of torsion texture development

Canova et al. (1984) modeled texture evolution in monotonic torsion, applying both full constraints and relaxed constraints Taylor theory. Both models were found to describe the texture evolution well at small strains. At large strains the relaxed constraints calculation showed a better fit to experimental data. Rollett et al. (1988) modeled texture evolution in cyclic torsion, using two different codes. Using a code based on Bishop and Hill analysis resulted in full reversal of the texture in cyclic torsion.

Calculations with the Asaro-Needleman code left a small residual texture after a full torsion cycle.

3.6 Annealing after torsion

3.6.1 Recrystallisation

Recrystallisation after torsion follows similar mechanisms as recrystallisation after other deformation modes. Still, one characteristic feature of recrystallisation after torsion is the development of the Bs recrystallisation texture component. The Bs-component is $30^\circ \langle 111 \rangle$ rotated with respect to the B^1 -component, and is especially prominent at recrystallisation after large torsional strains. Pettersen (1999) proposed two mechanisms for the origin of the Bs-component. Provided that the Bs orientation is stable during deformation, the Bs oriented grains will pinch off at large strains leaving island regions of the Bs orientation. However, small regions of Bs orientation were also detected at strain lower than the expected pinch off strain. These regions were explained as a result of a $30^\circ \langle 111 \rangle$ rotation of Bs orientated areas in the surface regions of B^1 oriented grains as shown in fig. 3.8. These Bs oriented regions will be surrounded by an area of gradually changing misorientation, giving them an advantage as a nucleation site. The B^1 component was found to increase with strain, and thus the probability of formation of Bs oriented grains during recrystallisation also increases with strain, as observed experimentally by Pettersen.

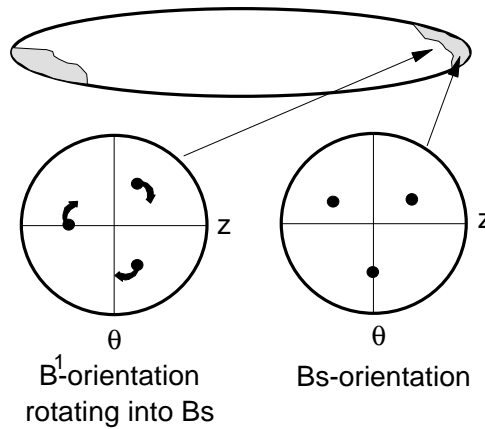


Fig 3.8: Formation of small B_s oriented areas by rotation of parts of a B¹ oriented grain. (Pettersen (1999))

3.6.2 The effect of strain path

Vatne et al. (1996e) investigated recrystallisation after monotonic and cyclic torsion in an AA3003 alloy, and observed larger recrystallised grain size after cyclic torsion.

3.6.3 Geometric dynamic recrystallisation

The origin of the term “geometric dynamic recrystallisation” (GDRX) is given as a result of the observations of the microstructures, and follows the following mechanism (McQueen et al. (1989)): During deformation at increasing strains, the original grains change their shape and become elongated in the direction of the deformation. Due to dynamic recovery the grain boundaries develops serrations of a wavelength similar to the subgrain size. As the grain thickness is reduced, the distance between the original grain boundaries will become comparable with the serrations. Thus, at some critical strain the grains are pinched off. The resulting microstructure will be composed of equiaxed grains surrounded by high angle boundaries. As is evident from the above description, the

mechanism of geometric dynamic recrystallisation is not a nucleation-and-growth process in the same sense as static or dynamic recrystallisation. However, as it produces small crystallites that are fully or partly surrounded by high angle boundaries, the recrystallization term can be justified.

The critical strain for pinch off of the grains may be calculated on the basis of geometrical considerations. In eq. 3.7 the distance between high angle boundaries as function of torsional strain was given. If we assume perforation of the grains at an axial width of $D_z=2\mathbf{d}$, the critical strain for pinching of the old grains becomes,

$$\mathbf{e}_c = \frac{D_0}{2\sqrt{3} \cdot \mathbf{d}} \quad (3.8)$$

where \mathbf{d} is the subgrain size. Since the above equation contains the subgrain size it can be replaced with an expression relating critical strain to the flow stress, or equivalently, the Zener-Hollomon parameter. That is, the pinch off strain depends on the deformation conditions (strain rate and temperature) and material properties such as initial grain size.

4 Experimental techniques

4.1 Materials and heat treatment

4.1.1 The alloys

Two different alloys have been studied. The chemical composition of the two alloys is shown in table 4.1.

Table 4.1: Chemical composition of the investigated alloys (wt%)

	<i>Mg</i>	<i>Si</i>	<i>Fe</i>	<i>Mn</i>	<i>Ti</i>	<i>Zn</i>	<i>Cu</i>
AA1050	0.0024	0.090	0.27	0.0027	0.023	0.015	0.0003
AA3103	-	0.12	0.57	1.02	-	-	-

Both alloys were cast at Hydro Sunndal. AA1050 was cast as sheet ingot, while AA3103 was DC-cast, producing a billet of diameter 203 mm. The outer 2 cm. were not used for samples, in order to assure homogeneity.

4.1.2 Homogenization

The A1050 alloy was heated 6°C/h to 560°C, held there for six hours and then water quenched. The AA3103 alloy was heated 100°C/h to 610°C, held for eight hours, cooled at 87°C/h to 450°C and then air cooled to room temperature.

4.2 Hot torsion

4.2.1 Sample geometry

The geometry of the torsion samples is shown in fig 4.1. The sample is solid with a gauge length and diameter of 10mm.

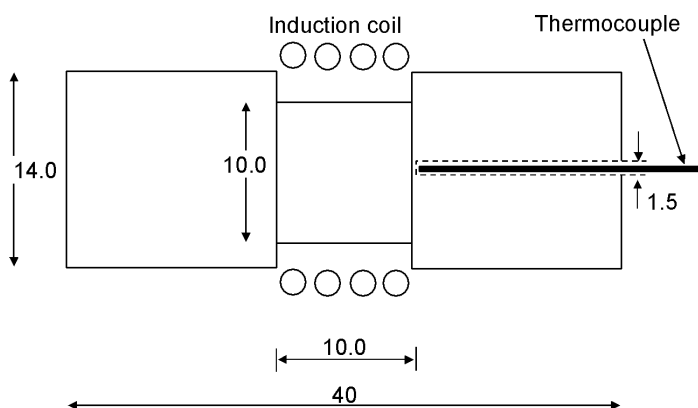


Figure 4.1: Sample geometry of the torsion specimen, with position of thermocouple and induction coil. From Pettersen (1999)

4.2.2 Temperature control

The sample was heated by an induction coil positioned as shown in figure 4.1. A thermocouple, measuring the temperature in the centre of the sample, was connected to the temperature control unit and thus enabling a controlled increase in temperature to the selected level. The heating rate was slowed down to 1°C/s as the set point was approached, to prevent temperature overshoot. Before deformation was started the samples was kept at the deformation temperature for 300 seconds, in order to ensure homogenous temperature. To preserve deformation microstructure, the samples were water quenched immediately after deformation.

However, there will be temperature gradients in the sample prior to deformation because of conduction to the cooled torsion machine. During deformation, adiabatic heating of the sample will also occur. The magnitude of these effects, and their influence on the recorded results will be dealt with in chapter 6.1.1.

4.3 Annealing

The samples were isothermally annealed by direct immersion in molten salt baths. The samples were agitated in the bath after immersion to ensure rapid heat transfer, and were water quenched after heat treatment.

4.4 Microstructural characterisation

4.4.1 Sample geometry and preparation

The sample geometry for light optical microscopy and SEM-investigations is shown in figure 4.2. The samples were investigated in the $z\theta$ plane, and care was taken to make sure the plane of study was at the same distance from the centre for all the samples.

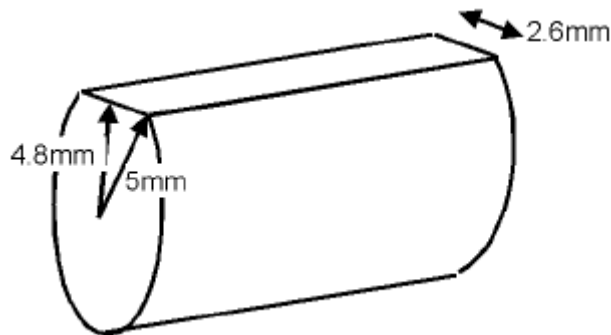


Fig 4.2: Torsion specimen for light optical and SEM investigations. From Pettersen (1999)

The initial preparation of the samples was carried out using SiC-paper, to a grid size of 2400. The samples for light optical microscope were then polished with 6μ and 3μ diamond spray, followed by anodising in Barkers reagent to reveal the grain structure under polarised light. The samples for EBSD-study were electropolished at 30 volts for 10 seconds in a solution of 7.8%

perchloric acid, 10% buthylglycol, 12% distilled water and balance ethanol.

4.4.2 Light optical microscopy

In the present work, light optical microscopy has only been used to get an overview of the deformed microstructures, using polarised light. The light optical microscope is well suited for this because of its large field of view. A Leica microscope has been used in the current study.

4.4.3 Scanning electron microscopy

In addition to higher resolution than the light optical microscope, the scanning electron microscope (SEM) also enables measurements of chemical composition and orientation of crystals in the sample

The EBSD technique

The Electron Back-Scattering Diffraction Technique (EBSD). In the study of samples deformed in torsion EBSD has been used for measurements of subgrain sizes, misorientations between subgrains and distance between high angle boundaries in the deformed structure. For the recrystallised samples, EBSD has mainly been used to determine the recrystallised grain sizes.

The principles of the EBSD-method are as follows: When the electrons in the incident beam hit the specimen, some of them will undergo elastic scattering with the atoms in the specimen, and a certain fraction of these electrons will become diffracted according to the Bragg law on their way out. Some of these back-scattered and diffracted electrons hit a phosphor screen giving a pattern showing the planes in the crystal, the EBSD pattern. Through a lead glass in

the specimen chamber the EBSD pattern is registered by a camera and displayed on a monitor. Before presentation on the monitor, the background is subtracted and the image is processed to give better interpretation. To provide a high density of detected back-scattered electrons, the samples were tilted to an angle of 70° during operation. The microscope was operated at an acceleration voltage of 20 kV, a beam current of $1 \cdot 10^{-9} - 1 \cdot 10^{-8}$ A and the specimen was placed at a working distance of 21-23mm.

The orientation of the specific grain or subgrain can be obtained by indexing the pattern displayed. When running the indexing in an automated mode, the EBSD pattern is detected automatically from the digitalized image on the monitor. A software package calculated the orientation for the specific point and the beam or the stage is moved to measure the orientation of the next point. Many thousands of orientations can be collected in this manner, and a map of the orientations in the specimen is obtained. When reconstructing the microstructure from orientation maps, it is necessary to define the minimum angle of misorientation that is plotted as a boundary. In the present investigation a boundary is designated as a high angle boundary if the rotation angle is greater than 15° , and as a low angle boundary if the orientation lies below 15° and above 2° . Recrystallised grain sizes and subgrain sizes were recorded by the linear intercept method. The mean intercept length was the average between the intercept length in the shear and normal direction.

4.5 Global texture measurements

4.5.1 Sample preparation

The specimens for texture measurements were made by drilling out the core of the gauge section of the torsion sample, leaving a cylinder with 1 mm tick walls. The cylinder was cut open and carefully flattened out. The outer surface was ground, using SiC

paper to a grit size of 1200. The samples were then etched by a solution of 15% NaOH and sugar (one teaspoon per litre). This was followed by 20 seconds in water and 20 seconds in 25% HNO₃ solution.

4.5.2 Reference frame and notation of orientations

Fig 3.2 showed the geometry of the torsion sample. With regard to Miller indexes, {hkl} is parallel to the z-direction, and <uvw> is parallel to the q -direction, as illustrated in figure 4.2.

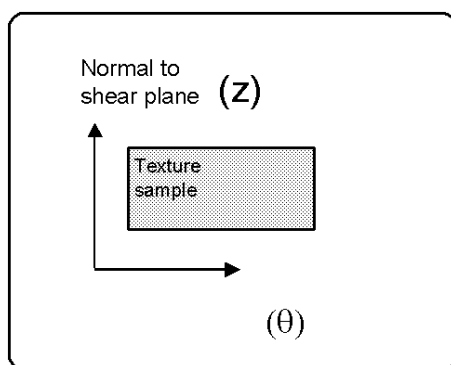


Fig 4.2: Geometry of the torsion texture sample. From Pettersen (1999)

4.5.3 Measuring routines

A Siemens D5000 X-ray diffractometer was used for the texture measurements. The specimen was permitted to rotate such that a partial pole figure extending to 80° from the centre was obtained. Simultaneously the sample oscillated in the specimen plane in order to increase the investigated area and improving the statistics of the texture recording.

During the measurements diffraction takes place according to the Bragg's law:

$$2 \cdot d \cdot \sin \mathbf{q} = n \cdot \mathbf{l} \quad (4.1)$$

The equation states that for an incoming X-ray beam of wave length \mathbf{l} and inclination angle \mathbf{q} , reflection only takes place from planes of interplanar distance d that fulfil eq. 4.1. For cubic crystals like aluminium

$$d = \frac{a}{\sqrt{h^2 + k^2 + l^2}} \quad (4.2)$$

where a is the lattice constant and $\{hkl\}$ are the Miller indices of the corresponding plane. As \mathbf{l} is a constant given by the type of X-ray tube that is used eq. 4.1 and 4.2 give a unique relationship between the incoming angle \mathbf{q} and the reflecting plane $\{hkl\}$. This means that a pole figure for a given plane $\{hkl\}$ is measured by selecting the angle \mathbf{q} in accordance with Bragg's law and keeping this constant during the measurement. The $\{hkl\}$ pole figure is then measured by rotation and tilting of the specimen during which the normals of the $\{hkl\}$ planes are recorded.

Chapter 4: Experimental techniques

5 Experimental results

5.1 The starting material

The grain size and texture of the starting material was determined using EBSD-mapping. Examples of the microstructures are shown in fig 5.1 and 5.2

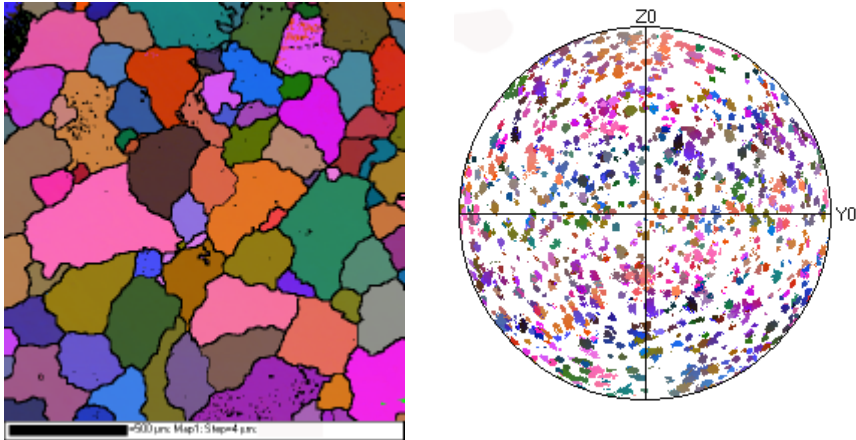


Fig 5.1: Microstructure and texture of AA1050 as cast.

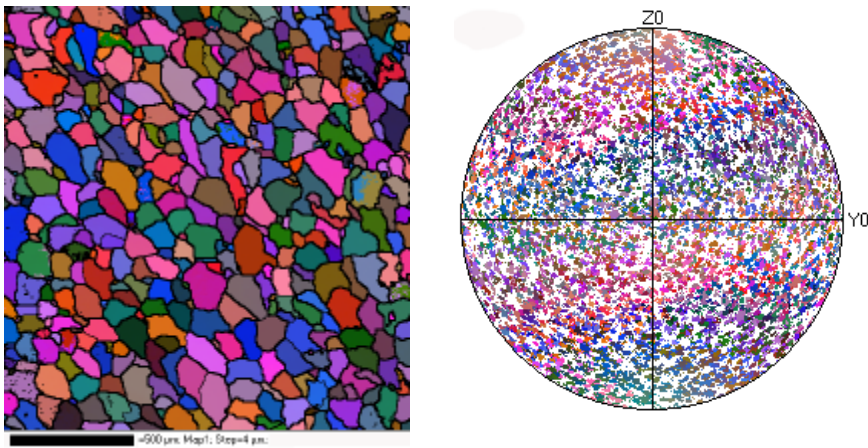


Fig 5.2: Microstructure and texture of AA3103 as cast

There is a considerable difference in grain size between the alloys. Using the line intercept method, the average grain size was found to be $82\mu\text{m}$ for AA3103, and $135\mu\text{m}$ for AA1050. As expected, neither of the materials shows any texture, although the coarse grain size of AA1050 makes it hard, covering sufficient area.

5.2 Mechanical behavior

5.2.1 Specimen shape change

As seen from equation 3.1 and 3.4 the calculated stress and strain depends on the sample geometry. Thus, if the sample geometry changes during deformation, these changes have to be taken into account in the calculation. For one series of experiments the diameter and length of the gauge section were measured for each torsion step. The results are presented in fig. 5.3.

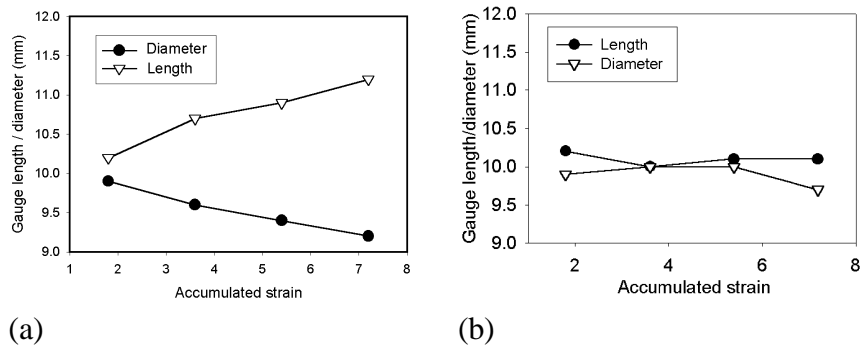


Fig 5.3: Specimen shape change during monotonic (a) and cyclic(b) torsion at $T=300^{\circ}\text{C}$ and $\dot{\epsilon}=1/s$

During monotonic deformation, a considerable shape change occurs. The diameter is reduced, and the gauge length increases. This behaviour will affect the calculation of stress and strain. During cyclic deformation the shape of the gauge section is more or less constant.

The shape change affects both stress and strain. The stress calculated, without taking the shape change into consideration, will be smaller than the actual stress. Similarly the calculated strain will be too large. To quantify these deviations, a closer look at the equations for torsional stress and strain is required.

5.2.2 Corrected stress and strain

Corrected strain data for specimen shape change

The torsional shear strain was defined in eq. 3.1. The equation for the shear strain refers to the instantaneous values of gauge length and radius, assuming both to be constant during deformation. With r and L depending on angle of rotation, it turns into an equation on the form:

$$\mathbf{g} = \int_0^{\mathbf{q}} \frac{r(\mathbf{q})}{L(\mathbf{q})} d\mathbf{q} \quad (5.1)$$

Assuming both $r(\mathbf{q})$ and $L(\mathbf{q})$ are linear functions, the equation for the corrected torsional strain becomes.

$$\mathbf{g} = \int_0^{\mathbf{q}} \frac{(a + b\mathbf{q})}{(c + d\mathbf{q})} d\mathbf{q} \quad (5.2)$$

Where a, b, c and d are constants. The corrected strain may then be found by integration of equation 5.2.

$$\mathbf{g} = \left[\frac{a}{d} \ln(c + d\mathbf{q}) + b \left(\frac{(c + d\mathbf{q}) - c \ln(c + d\mathbf{q})}{d^2} \right) \right] \quad (5.3)$$

The values for the constants a-c are obtained from linear regression of the experimental data for the development of L and r with q . The resulting equations for L and r then turn into

$$R = 5 - 0,0162q \quad (5.4)$$

$$L = 10 + 0.0501q \quad (5.5)$$

The corrected and the uncorrected strain is plotted as function of angle of rotation, in fig. 5.4.

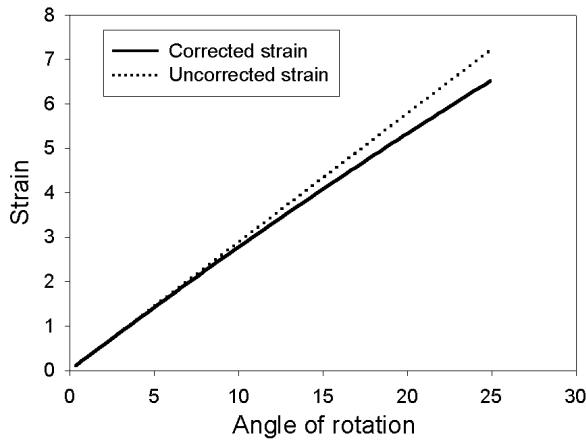


Fig 5.4: Corrected and uncorrected strain as function of angle of rotation for AA1050 deformed at $T=300^{\circ}\text{C}$ and $\dot{\epsilon} = 1/\text{s}$

It is clear that the shape change influences the calculation of the strain. Still the influence is relatively small at strains less than $\epsilon=5$. Thus, in the presented stress strain curves, uncorrected strain data will be used. This is done in order to clearly visualize which sets of monotonic and cyclic deformed samples are subjected to the same net deformation.

Corrected stress data for specimen shape change

Looking at the equation for the shear stress in torsion (eq. 3.4), the correction for shape change is easily introduced. Given that the dimensions of the specimen at each investigated strain are known. To correct the equation for change in sample geometry, the initial value of r is simply replaced by the actual value as strain increases. Assuming a linear relationship between r and q , the expression for $r(q)$ is, as previously shown, easily obtained from the experimental data by linear regression.

5.2.3 Corrected stress strain curves

The stress strain curves for cyclic and monotonic torsion, with stress corrected for specimen shape change, are shown in fig. 5.5 and 5.6.

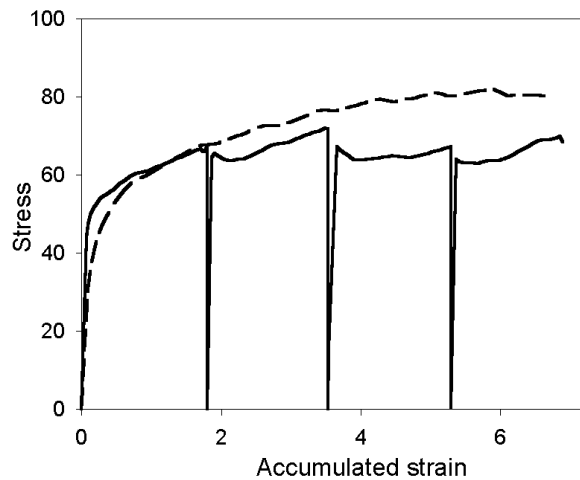


Fig 5.5: Stress-strain curves for AA1050 deformed in monotonic (dotted) and cyclic (solid) torsion at $T=300^{\circ}C$ and $\dot{\epsilon}=1/s$. Corrected for change in sample geometry.

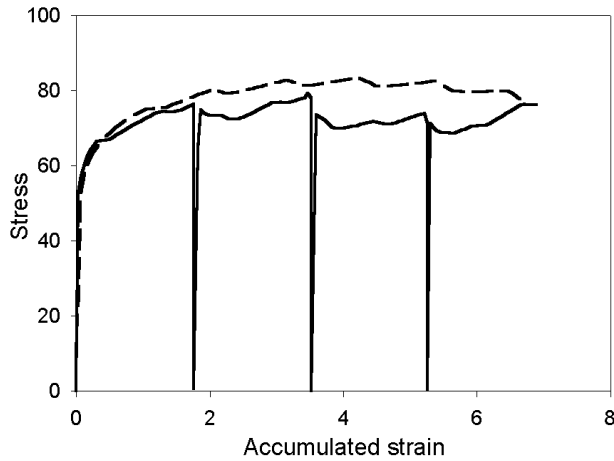


Fig 5.6: Stress-strain curves for AA3103 deformed in monotonic (dotted) and cyclic (solid) torsion at $T=300^{\circ}\text{C}$ and $\dot{\epsilon} = 1/\text{s}$. Corrected for changes in sample geometry.

The stress strain curves of both alloys are relatively similar. Subjected to monotonic deformation, the AA1050-sample fractured at a strain slightly below $\epsilon=7$, and thus the largest strain for AA1050 is $\epsilon=6.8$. The reason why AA1050 fractured before AA3103 is probably the larger initial grain size. As expected, AA3103 hardens faster than AA1050, reaching a peak flow stress at a strain of approximately $\epsilon=3$. On the other hand, AA1050 hardens continuously for the whole strain range, and reaches the same stress as AA3103 approximately at a strain of $\epsilon=5$. Thus, the flow curve of AA1050 is showing a tendency to stage IV hardening, which is quite surprising under the given deformation conditions. The two alloys also behave remarkably similarly in cyclic torsion. After the first reversal, only small signs of the Baushinger effect are seen. After the flow stress is reached, a plateau in the flow stress is observed, followed by a rapid increase at the same rate as for monotonic torsion. In the second strain reversal, the Baushinger effect is observed in both alloys. A small initial peak, followed by a

drop and an area of constant flow stress. Towards $\epsilon=5.6$ an increase in flow stress is observed. The third strain reversal is similar to the first, showing rapid strain hardening towards $\epsilon=7.2$. The difference in flow stress between cyclic and monotonic torsion is largest after the second strain reversal (cumulative strain of $\epsilon=5.6$) for both alloys. The difference in flow stress between cyclic and monotonic torsion is also largest for AA1050 at all strain states. In AA3103 the difference between flow stress in cyclic and monotonic torsion is very small after cumulative strains of $\epsilon=5.6$ and $\epsilon=7.2$

5.3 The deformed state

5.3.1 Light optical micrographs

Although the resolution in light optical microscopy is relatively small, the technique gives a good overview of the microstructure. In fig. 5.7 light optical micrographs of AA1050 as cast and deformed in monotonic and cyclic torsion to various strains at $T=300^\circ\text{C}$ and $\dot{\epsilon}=1/\text{s}$ are given.

The samples deformed in monotonic torsion to strains of $\epsilon=1.8$ (fig. 5.7b) and $\epsilon=3.6$ (fig. 5.7d) shows a microstructure consisting of elongated grains. The angle of the grains relative to the torsion axis is approaching 90° as the strain is increased. In fig 5.7c the microstructure after the first torsion cycle is shown. The grains have now regained their original shape, and the microstructure is similar to the as cast structure. The restoration of the original grain shape after a full torsion cycle is interesting, but hardly a surprise as similar behavior has been reported formerly.

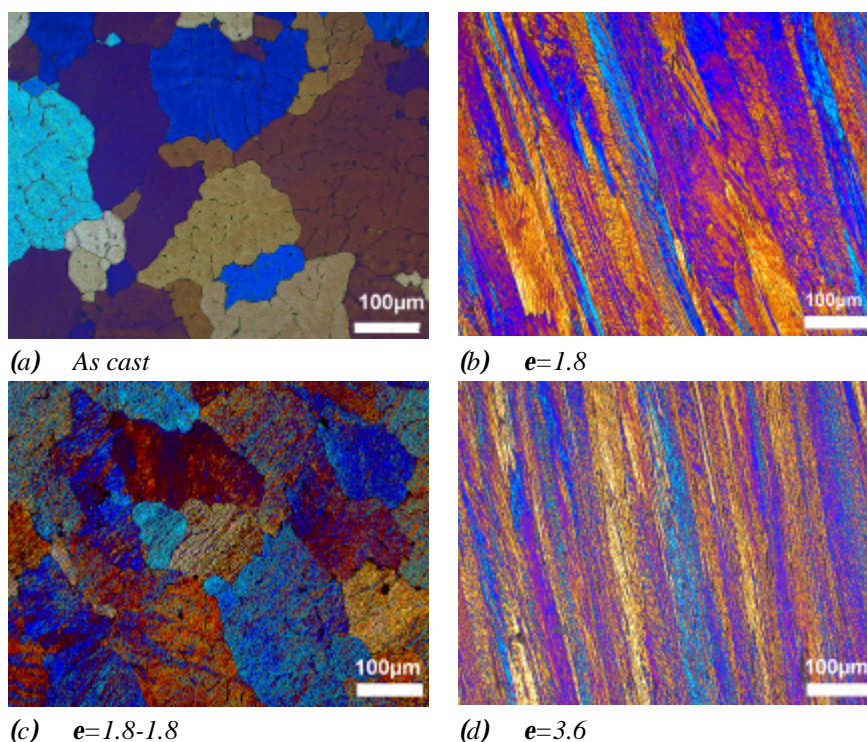


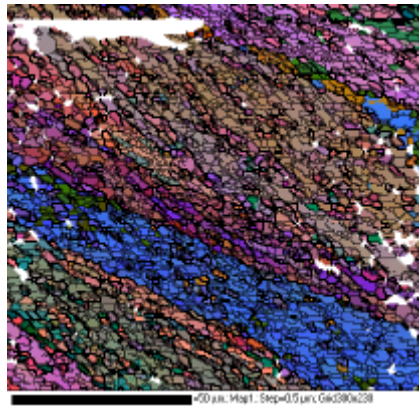
Fig 5.7: Light optical micrographs of AA1050 deformed in cyclic and monotonic torsion at $T=300^{\circ}\text{C}$ $\dot{\epsilon} = 1/\text{s}$

5.3.2 EBSD – images

The use of EBSD enables a thorough description of the microstructure, not only qualitatively but also in terms of quantitative measurement of microstructure parameters like subgrain-size and misorientation. In fig 5.8 (a-g) the microstructure of AA3103 deformed in cyclic and monotonic torsion to various strains at $T=300^{\circ}\text{C}$ and $\dot{\epsilon} = 1/\text{s}$ is shown for a cumulative strains from $e=1.8$ to $e=7.2$

For monotonic deformation to $e=1.8$ (fig 5.8a), the EBSD-micrographs shows a microstructure consisting of elongated bands, separated by high angle boundaries. Within the bands, low angle

boundaries are dominating. After a monotonic strain of $\epsilon=3.6$ (fig 5.8c) the microstructure still consists of elongated bands, but within the bands, high angle boundaries get increasingly dominating. After strains of $\epsilon=5.4$ (fig 5.8e) and $\epsilon=7.2$ (fig 5.8g) the microstructure consists of small grains surrounded by high angle boundaries. There are now almost no signs of any band structure. After a cyclic strain of $\epsilon=1.8-1.8$ (fig 5.8b) the original grain shape is restored. Still the interior of the old grain is divided by both low- and high angle boundaries. After a cyclic strain of $\epsilon=1.8-1.8-1.8$ (fig 5.8d), the elongated bands observed after a monotonic strain of $\epsilon=1.8$ reappears. While increasing the strain to $\epsilon=1.8-1.8-1.8-1.8$ (fig 5.8f) to certain extent restores the equiaxed grain structure observed after a strain of $\epsilon=1.8-1.8$.



(a) $\epsilon=1.8$

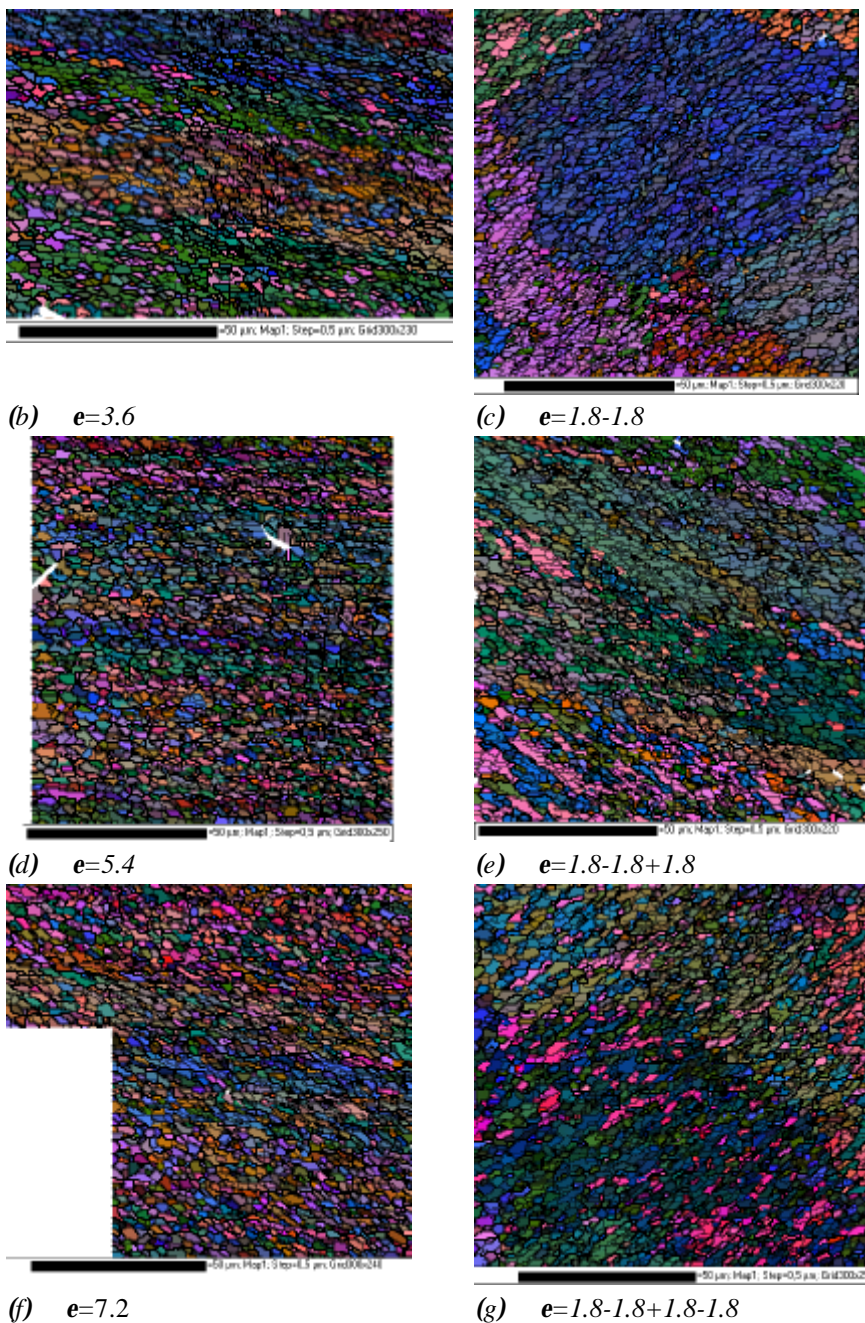


Fig 5.8: EBSD- images of AA3103 deformed in cyclic and monotonic torsion at $T=300^{\circ}C$ $\dot{\epsilon}=1/s$

In fig 5.9, selected EBSD-images from AA1050 deformed in cyclic and monotonic torsion at $T=300^{\circ}\text{C}$ $\dot{\epsilon} = 1/s$ are presented. The microstructure is quite similar to AA3103, although the larger initial grain size creates a larger band with.

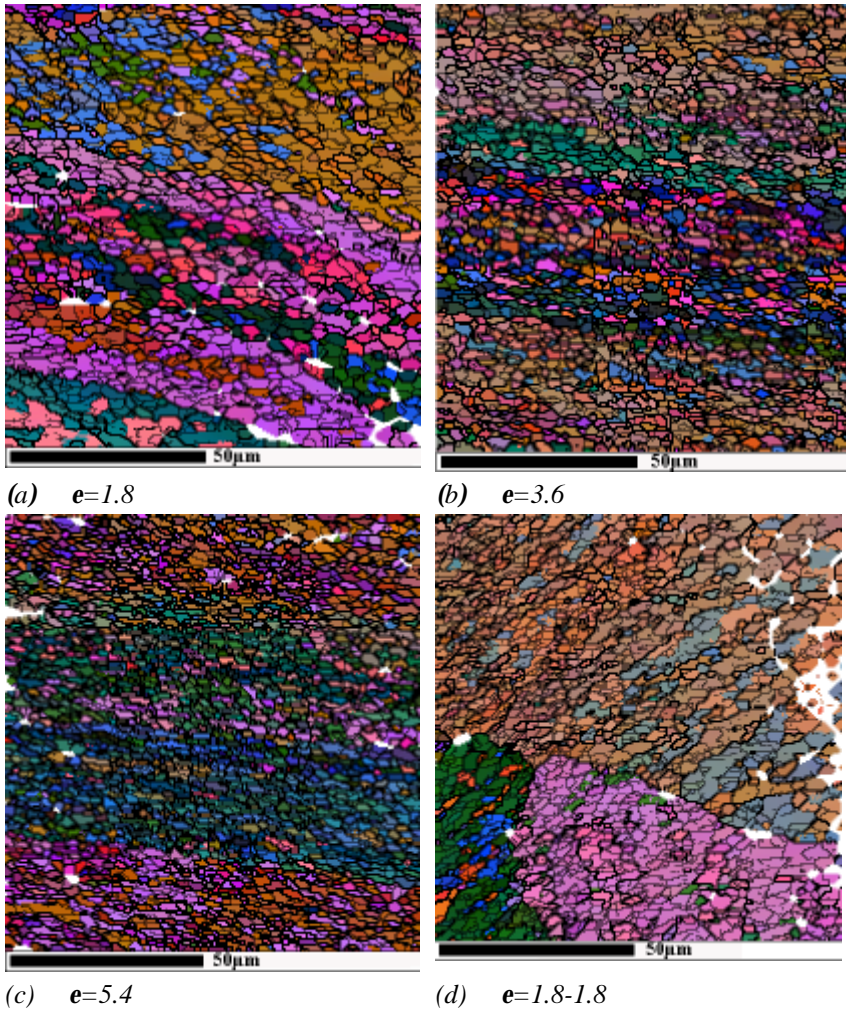


Fig 5.9: EBSD- images of AA1050 deformed in cyclic and monotonic torsion at $T=300^{\circ}\text{C}$ $\dot{\epsilon} = 1/s$

5.3.3 Subgrain sizes and misorientations

In order to explain and understand recrystallisation behavior, a thorough knowledge of the deformed state is important. The EBSD-data enables measurement of quantitative properties, which is helpful to understand the development of the as deformed microstructure.

The subgrain size and average misorientation were measured for all the strain states and for both alloys. The mean intercept length was measured for all angles larger than 2 degrees. The results are shown in fig 5.10 and 5.11. The main information gathered from the measurements of subgrain size, is the difference between the alloys. In AA1050, the subgrain size decreases up to a strain of $\epsilon=5.4$, which is in fact supporting the observations of continuously increasing flow stress in the same region. In contradiction to this, the subgrain size in AA3103 is not affected by increasing strain in the strain range investigated, being more or less constant at $1.8\mu\text{m}$. Strain path changes, seems to have only minor, if any, effects on subgrain size.

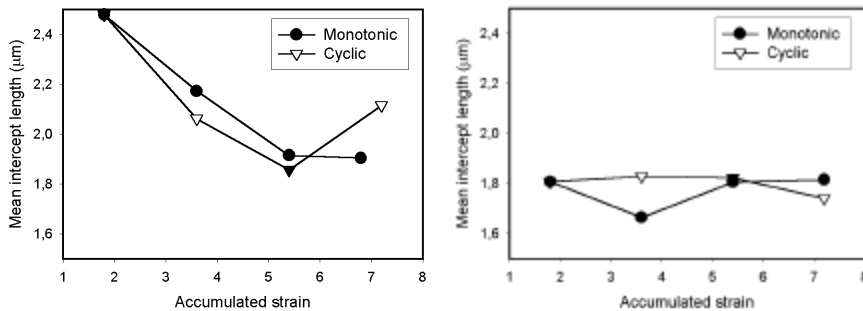


Fig 5.10 Boundary separation in AA1050 and AA3103 deformed in cyclic and monotonic torsion at $T=300^{\circ}\text{C}$ and $\dot{\epsilon}=1/\text{s}$

Part II: Strain path effects on recrystallisation after hot torsion

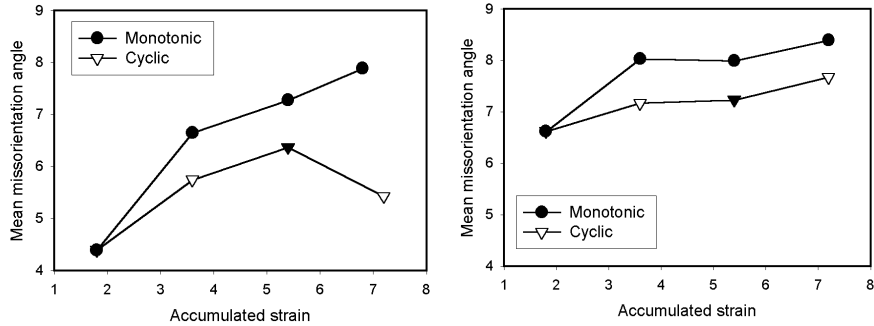


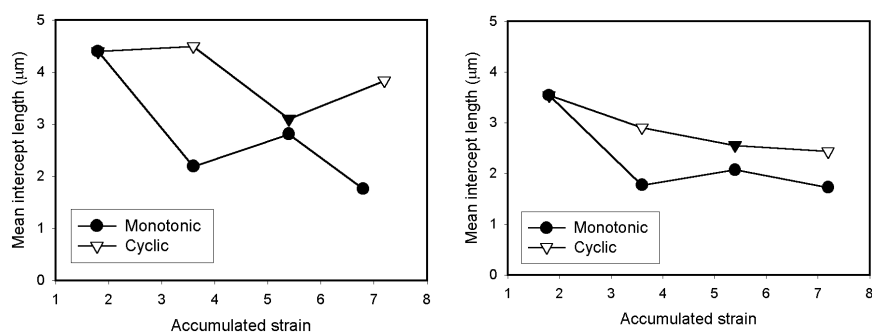
Fig 5.11: Average misorientation in AA1050 and AA3103 deformed in cyclic and monotonic torsion at $T=300^{\circ}\text{C}$ and $\dot{\epsilon} = 1/s$

Differences in average subgrain misorientation affect the driving pressure for recrystallisation, without affecting the flow stress and thus is important for understanding the recrystallisation process. Clearly, average misorientation depends on both strain path, alloy and deformation conditions. The average misorientation generally increases with strain during monotonic torsion. In AA3103 the misorientation increases rapidly from $e=1.8$ to $e=3.6$, and then reaches an almost steady state. In AA1050 a steady increase is seen for the whole strain range although it remains lower than for AA3103. For the cyclic case, the increases in average misorientation with increasing accumulated strain are smaller. Still, there are differences between the alloys. AA1050 has a smaller average misorientation than AA3103. AA1050 also displays a slowly increasing average misorientation, while AA3103 shows only small variations with cyclic strain. In AA1050 there is also a drop in the average misorientation from $e=5.4$ to $e=6.8$, although the difference may be within the error margins. The differences in average misorientation between samples deformed to the same net strain along cyclic and the monotonic strain path are generally larger for AA1050, than for AA3103. But in both cases, the average misorientation will be largest along the monotonic strain path for

any given accumulated strain. In all comparable cases AA3103 has a larger average subgrain misorientation than AA1050.

5.3.4 Distance between high angle boundaries

At large strains and at large values of the Zener-Hollomon parameter, new high angle boundaries are commonly formed during deformation. In order to estimate the break up, the distance between high angle boundaries in the as deformed microstructure was measured from the EBSD-data. The mean intercept length was measured in the direction normal to the shear direction and the results are shown in fig 5.12. Taking into account that the average distance between high angle boundaries in the as cast material was $82\mu\text{m}$ for AA3103 and $135\mu\text{m}$ for AA1050, it is clear that considerable break up occurs during deformation. In fig 5.13 the experimentally observed distance between high angle boundaries is compared to the distance between high angle boundaries during monotonic torsion calculated from equation 3.7.



AA1050

AA3103

Fig 5.12: Distance between high angle boundaries in the as deformed microstructure $T=300^{\circ}\text{C}$ $\dot{\epsilon}=1/s$

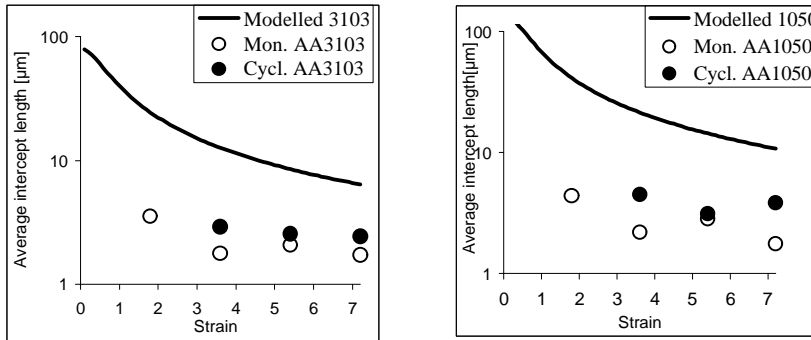


Fig 5.13: Observed distance between high angle boundaries, compared to calculated distance based on elongation of grains only. $T=300^{\circ}C$ $\dot{\epsilon} = 1/s$

Relative to the calculated distance between high angle boundaries, the break up is largest in AA1050. Most of the break up occurs during the first torsion step, while the changes after the additional steps are smaller. Still the distance between high angle boundaries is larger after cyclic than monotonic torsion. This observation is in contradiction to the measured subgrain sizes, where strain path did not seem to have any effect.

5.3.5 Fractions of boundaries of low, medium and high misorientation

The fractions of boundaries of low, medium and high misorientation were also measured from the EBSD data. The results are presented in fig. 5.14 and 5.15 for AA1050 and AA3103 respectively.

Chapter 5: Experimental results

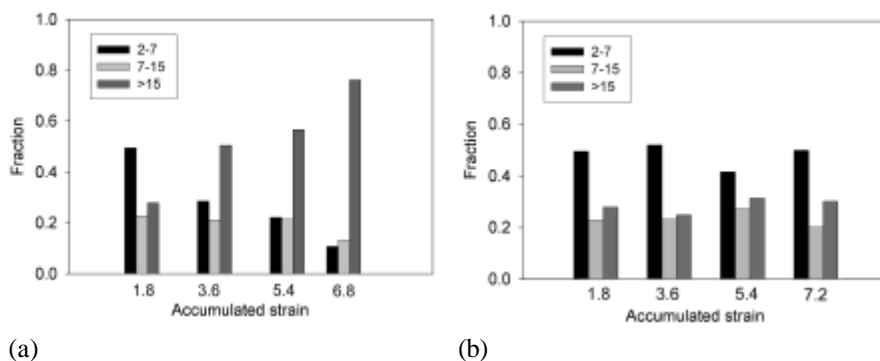


Fig 5.14: Fractions of boundaries of high, medium and low misorientation for AA1050 deformed in monotonic(a) and cyclic(b) torsion $T=300^{\circ}\text{C}$ $\dot{\epsilon} = 1/s$

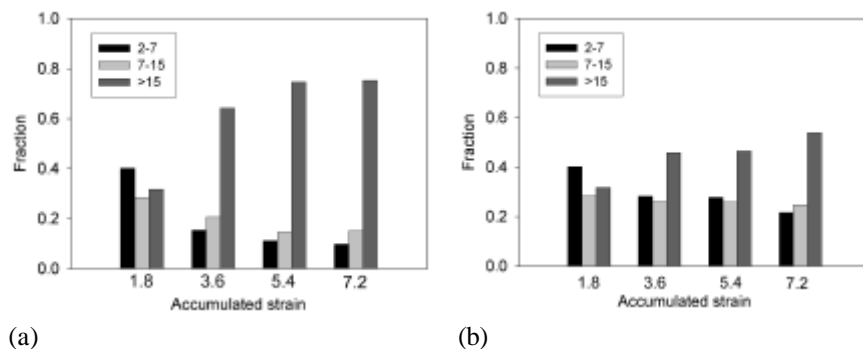


Fig 5.15: Fractions of boundaries of high, medium and low disorientation for AA3103 deformed in monotonic (a) and cyclic(b) torsion $T=300^{\circ}\text{C}$ $\dot{\epsilon} = 1/s$

The fraction of high angle boundaries increases during monotonic deformation. From a strain of $\epsilon=3.6$, high angle boundaries are dominating. At the largest strains almost 80% of the boundaries are of high angle character. After cyclic torsion, the high angle boundaries are less dominating. This is especially the case for AA1050 where a considerable fraction of low angle boundaries remains, even at the largest cyclic strains. Both after cyclic and monotonic torsion at the development of high angle boundaries is faster in AA3103, compared to AA1050. This is probably as a result of the larger fraction of large particles in AA3103.

5.3.6 Deformation textures

The development with strain and strain path of torsion textures has been investigated. Three types of texture components have been observed. The designation of Montheillet et. al. (1984) has been employed. The observed texture components are labelled as follows:

$$(A^2) \quad \{\bar{1}\bar{1}1\}\langle 112 \rangle \text{ and } \{11\bar{1}\}\langle 112 \rangle$$

$$(B^1) \quad \{\bar{1}12\}\langle 110 \rangle \text{ and } \{1\bar{1}\bar{2}\}\langle \bar{1}\bar{1}0 \rangle$$

$$(C) \quad \{001\}\langle 110 \rangle$$

Schematic illustrations of the components as $\{200\}$ polefigures are given in fig. 5.16. In Fig 5.17 and 5.18 the deformation textures after deformation at $T=300^\circ\text{C}$ $\dot{\epsilon}=1/\text{s}$ are shown for AA1050 and AA3103 respectively.

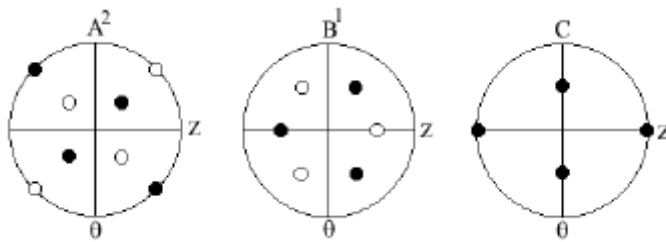


Fig 5.16: Schematic illustration of texture components found in aluminium deformed in torsion.

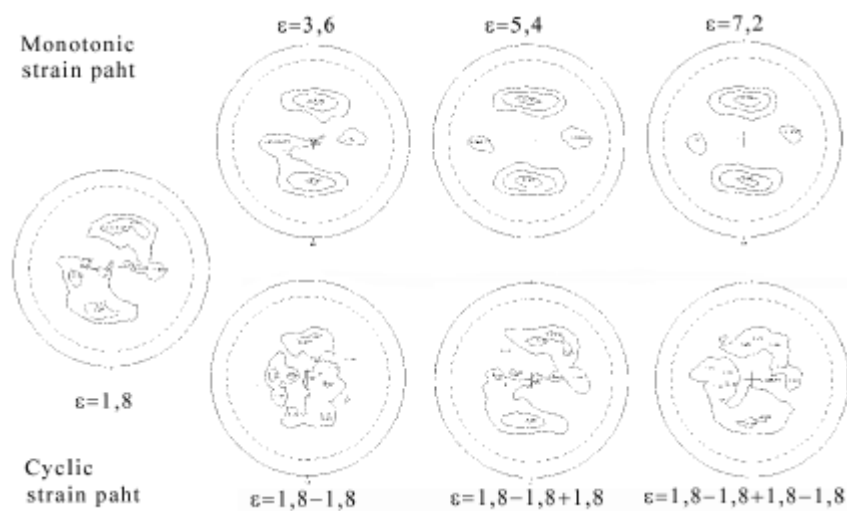


Fig 5.17: Deformation textures for AA1050 deformed in monotonic and cyclic torsion $T=300^{\circ}C$ $\dot{\epsilon} = 1/s$

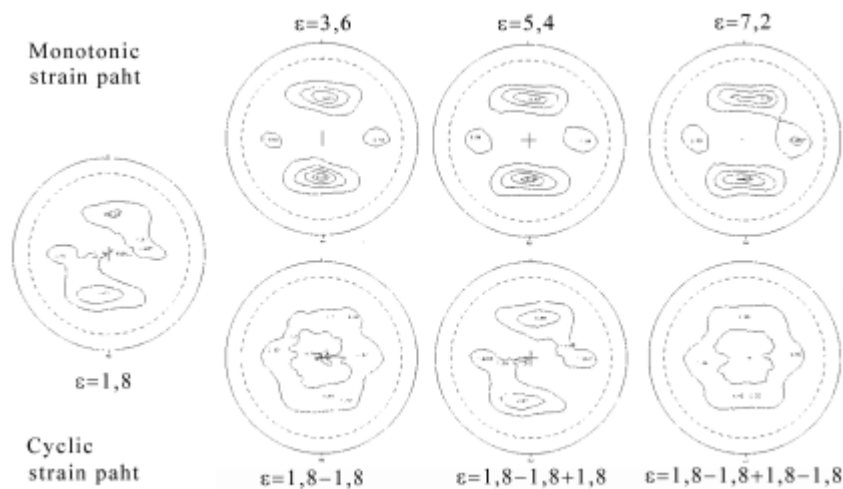


Fig 5.18: Deformation textures for AA3103 deformed in monotonic and cyclic torsion $T=300^{\circ}C$ $\dot{\epsilon} = 1/s$

In general, the textures are relatively weak. In monotonic torsion, the C-component is dominating at all strains. A weak B-component is also seen, and in AA3103 a small increase in this component is

seen as strain increases. During cyclic torsion the textures are even weaker, with no specific component dominating. Taking the random starting texture into account, it is clear that a residual texture component is left after the first full torsion cycle, i.e a cumulative cyclic strain of $\epsilon=3.6$. In contradiction to this, the deformation textures after a net strain of $\epsilon=1.8$ and cumulative strains of $\epsilon=1.8$ and $\epsilon=5.6$ respectively look similar and comparable. The same similarity is observed after zero net strain for cumulative strains of $\epsilon=3.6$ and $\epsilon=7.2$. This observation indicates that the initial texture is restored after a full torsion cycle if the starting state is already deformed. In contradiction, a full torsion cycle starting at an as cast state leaves a residual texture.

5.4 The recrystallisation process

The torsion samples were recrystallised at 450°C. The AA3103 samples were completely recrystallised after 20 seconds while the AA1050 samples needed 100 seconds to fully recrystallise.

5.4.1 Recrystallised grain sizes

Recrystallised grain sizes were measured by EBSD. The results are presented in fig 5.19. Both alloy composition and strain path affect the recrystallised grain size. For AA1050 a gradual decrease in recrystallised grain size is seen with monotonic strain, while the recrystallised grain size after cyclic strain is relatively constant at a larger level. The difference in recrystallised grain size is increasing with accumulated strain. For AA3103, increasing the strain above $\epsilon=3.6$ has no additional effect on the recrystallised grain size. The reduction in recrystallised grain size after an increase in strain from $\epsilon=1.8$ to $\epsilon=3.6$ is also quite small. The recrystallised grain size after cyclic torsion is relatively constant, as well as the difference in

recrystallised grain size after cyclic and monotonic torsion to the same cumulative strain.

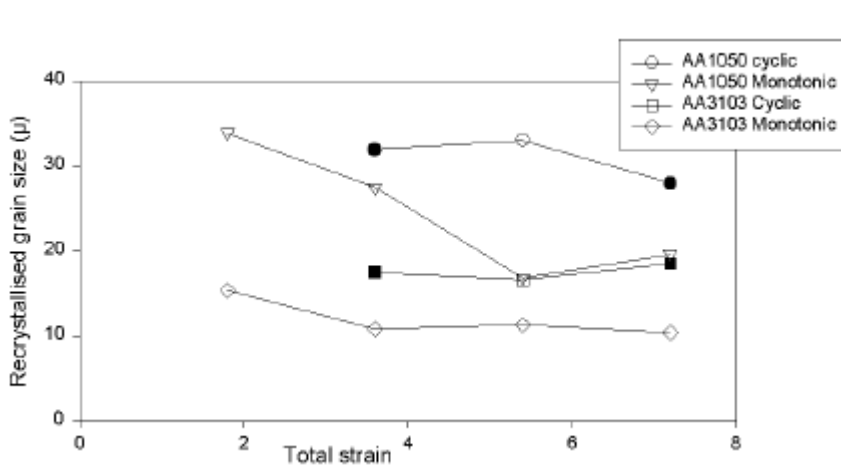


Fig 5.19: Recrystallised grain sizes for AA1050 and AA3103 recrystallised at 450°C after cyclic and monotonic torsion

5.4.2 Recrystallisation textures

The recrystallised textures were measured by x-ray diffraction. In fig. 5.20 and 5.21 the recrystallisation textures of AA1050 and AA3103 are shown. All the recrystallisation textures for both alloys are very weak. This is especially the case after cyclic deformation, where hardly any specific components can be distinguished. The recrystallised samples after monotonic strains of $\epsilon=5.4$ and $\epsilon=7.2$ reveals some interesting differences between the alloys. AA1050 shows a retained deformation texture with the B^1 component being the most distinct, even if the C-component dominates the deformation texture. After the same strains the recrystallisation textures of AA3103 are weaker, but a B_s texture (fig. 3.7) is starting to appear.

Part II: Strain path effects on recrystallisation after hot torsion

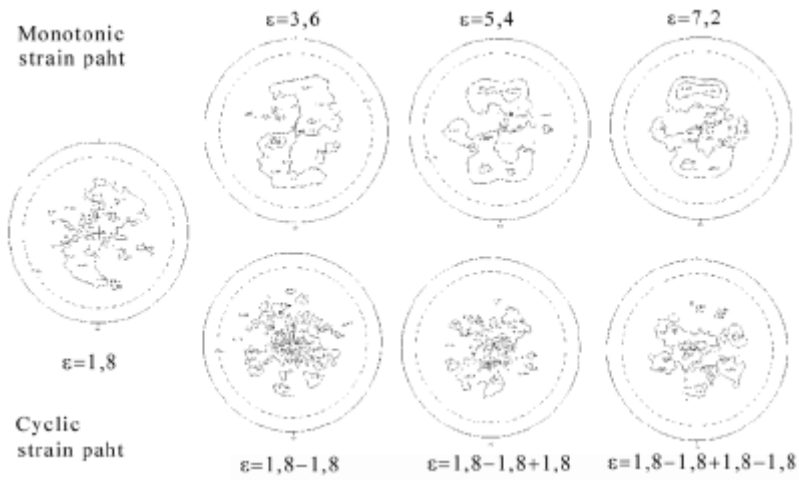


Fig 5.20: Recrystallisation textures AA1050

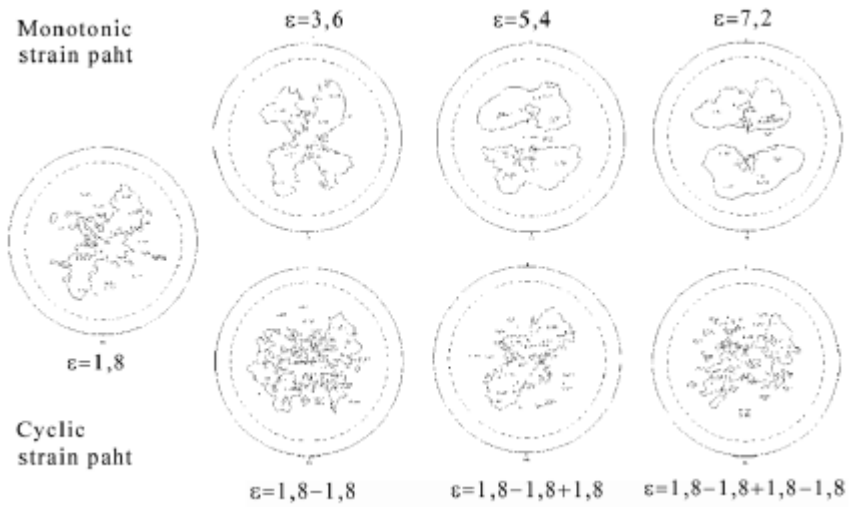


Fig 5.21: Recrystallisation textures AA3103

Pettersen (1999) reported strong Bs recrystallised textures in AA6060 and AA6082 deformed in torsion. The presence of the Bs texture in the recrystallised samples was always associated with a strong B¹ deformation texture. This was explained as a result of surface areas of B¹ grains rotating into Bs orientation during deformation by a 30° [111] rotation, and thus providing favourable nucleation sites. Pettersen observed the Bs component for samples deformed in monotonic torsion at $Z=7 \cdot 10^{11}/s$, to a strain of $\epsilon=3$ with increasing Bs component strength for $\epsilon=5$. The weak Bs component in this case supports the connection between the B¹ deformation texture and the Bs recrystallised texture.

6 Discussion

6.1 A closer look at the stress-strain data

In the present chapter, the stress strain behaviour of AA1050 and AA3103 during monotonic and cyclic torsion will be discussed. The shape of the individual flow curves will be discussed, as well as the difference in flow stress as function of strain path. First, however, the influence of deformation conditions on flow stress will be evaluated.

6.1.1 Influence of deformation conditions

The flow stress in hot deformation depends to a large extent on the strain rate and the deformation temperature. An estimate of the flow stress as function of strain rate and temperature can be obtained from the Sellars and McGregor Tegart relationship (eq. 2.3). The equation was fitted to experimental data for AA3103, with results shown in table 6.1. In the following, the effect of deformation temperature and strain rate will be investigated, and a combined maximum error will be calculated.

Table 6.1: Constants for the Sellars and McGregor Tegart relation, fitted for AA3103

constant	value
A	$1.53 \cdot 10^{13}$
$1/\alpha$	62.18
n	5.82

Deformation temperature

The sample temperature affects the value of the Zener-Hollomon parameter, and thus both the stress-strain curve and the microstructure after deformation. Prior to deformation, there will be temperature gradients in the torsion sample as a result of conduction to the cooled torsion machine. The induction coil also

primarily heats the surface of the sample, and thus the heating of the interior of the sample is due to conduction. During deformation, adiabatic heating of the sample will also affect the temperature. Pettersen (1999) studied the temperature distribution in the torsion sample prior to deformation closely, and found that the temperature difference between the thermocouple and the surface of the sample at the center of the gauge section was increasing with temperature. At 300°C, the difference was 2°C, and at 400°C it was 4-5°C. During the deformation, approximately 5-10% of the energy will be stored in the sample as microstructural changes. The rest will be converted to heat. If the strain rate is low, this will be compensated by the temperature control system. However, at large strain rates the temperature control system will not be able to respond quickly enough. Thus the sample temperature will increase. Pettersen (1999) calculated the temperature increase due to adiabatic heating during deformation. For an AA 6082 alloy, deformed to a strain of $\epsilon=1$ at a strain rate of 5, the adiabatic temperature increase was calculated to 3.9°C and 4.8°C after deformation at 349°C and 398°C respectively.

These results are of course not directly transferable to the system investigated in this study, as both the alloys and deformation conditions are different. But it is seen that the temperature difference prior to deformation increases with temperature. In contradiction, the adiabatic temperature rise is decreasing with temperature. To give a totally precise description of the temperature distribution in the sample as function of time and position is difficult, as there are quite a few issues that has to be taken into consideration:

- The sample temperature will increase during deformation as a result of adiabatic heating. Thus the value of the Zener

Hollomon parameter will change continuously during deformation.

- For the largest monotonic strains in this investigation, the temperature control system should have time to correct for adiabatic heating, as the deformation takes over seven seconds.
- For cyclic torsion, the temperature will probably be corrected between the torsion steps, as the sample is left for a short while before the strain direction is reversed.

In total, it is likely that both the samples subjected to cyclic and monotonic deformation have a temperature higher than the one measured by the thermocouple. During deformation, the temperature probably increases due to adiabatic heating, and the increase is probably largest in the monotonically deformed samples. Still it is unlikely that the temperature increase is larger than 5-10°C. In this study the most important is that the temperature difference between samples deformed in cyclic and monotonic torsion is small. That condition seems to be fulfilled. In fig 6.1 an estimate based on the Sellars McGregor Tegart relationship is given for the potential influence of temperature differences on the flow stress. The figure shows that the maximum deviation in flow stress, given a difference in deformation of 10°C, is approximately 5 MPa.

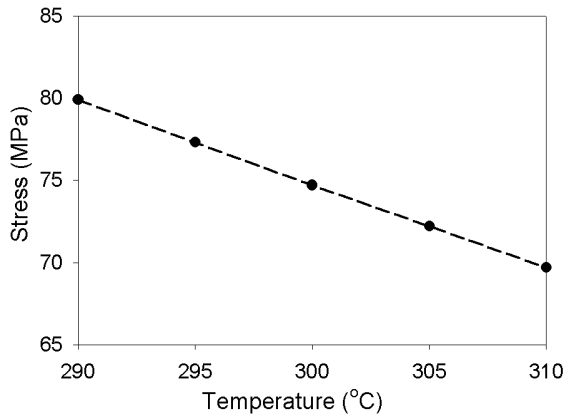


Fig 6.1: Influence of temperature on flow stress for AA3103

Strain rate

The strain rate during deformation is never constant. For an estimated maximum deviation of $\pm 10\%$ the resulting change in flow stress is shown in fig 6.2. The effect of change in the strain rate is smaller, compared to change in deformation temperature. Even a change in strain rate of 10% changes the flow stress less than 2MPa.

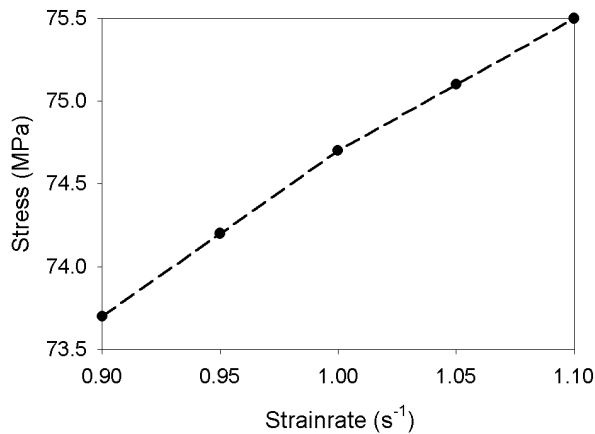


Fig 6.2: Influence of strain rate on flow stress for AA3103.

Combined effect

Combining the maximum deviations of temperature and strain rate, an estimate of the maximum error of the flow stress due to deformation conditions is obtained. The result is given in table 6.2.

Table 6.2: Effect on flow stress for combined deviations in strain rate and temperature.

	Strain rate (s ⁻¹)	Temperature (°C)	Estimated flow stress (MPa)
Minimum	0.9	290	68.8
Normal	1.0	300	74.7
Maximum	1.1	310	80.8

As seen from the table, a deviation of 6 MPa is predicted as the maximum deviation in flow stress, on basis of the given variations in strain rate and temperature.

6.1.2 The flow stress curve after monotonic torsion

To investigate the stress strain behavior in monotonic torsion is not the key aspect of this study. Still, some comments to the stress strain curves after monotonic torsion are required. As was explained in chapter 3.3, the flow stress curve in torsion usually shows rapid hardening to a peak value, followed by a gradual decrease to a flow stress plateau. This behavior was observed by Pettersen and Nes (2003) for AA6060. The peak was seen to sharpen at large values of the Zener-Hollomon parameter. However, in this study neither AA1050 nor AA3103 show this kind of stress-strain behavior. In stead a gradual increase in flow stress ending in a plateau is observed. For AA3103 the plateau in flow stress is reached at a strain of approximately $\epsilon=2$, while AA1050 shows hardening up to a strain of almost $\epsilon=6$. Especially the latter is surprising. Still the measured subgrain sizes provide support for the flow stress

observations. In AA3103 the subgrain size remains constant for increased strains from $\epsilon=1.8$, while in AA1050 the subgrain size decreases from $e=1.8$ to $e=5.4$. However, when interpreting the flow stress curves it should be noted that the correction introduced for specimen shape change, as well as the effect of variance in deformation conditions, also could play a significant role. For the calculation of the shear stress a constant value of q has been used in eq. 3.4. Rønning (1998) observed that q decreased at high strains. Thus, keeping q constant will result in too large values for the stress at high strains. However, by looking at eq. 3.4 it is clear that this effect will be relatively small.

Even if the absence of work softening is surprising, such behavior has been observed before. As mentioned in chapter 3.3.1 Mousavi (1995) found the shape of the stress strain curve in AA3003 to be dependent on homogenisation schedule. For a homogenisation schedule similar to the one employed in the current study, no work softening was observed.

6.1.3 The flow stress curve after cyclic torsion

Although the *difference* between the flow stress curves after cyclic and monotonic torsion is the key aspect to understand the difference in recrystallisation properties as function of strain path, the flow stress curves after cyclic deformation shows some interesting features by themselves. As was also commented on in chapter 5.2 the level of the Baushinger effect is not the same for the three individual strain reversals. For both alloys only a small reduction in yield strength is observed after the first and third strain reversal. While a stronger Baushinger effect is seen after the second strain reversal. As the strain after reversal is large ($e=1.8$), no microstructural investigations have been carried out on material

quenched in the region where the Baushinger effect occurs. Thus, it is hard to say what microstructural features that cause this difference. It is however very interesting that the two investigated alloys behave so similarly. The shape of the stress strain curves after cyclic torsion is almost identical for AA1050 and AA3103, in contradiction to monotonic torsion, where different behaviour is seen. Stout and Rollett (1990) investigated strain path effects in torsion at room temperature for a variety of metals and alloys. They found that the behaviour of an Al-Cu alloy changed drastically when heat treatment was changed to produce semicoherent precipitates. Keeping the difference in particle distribution between AA3103 and AA1050 in mind, the similarity between the flow curves could suggest that particles do not influence the Baushinger effect in the same manner at elevated temperatures.

6.1.4 The difference in flow stress between cyclic and monotonic torsion

For the explanation of the recrystallisation behavior after cyclic and monotonic torsion, the difference in flow stress at large strain reversals is more important than the Baushinger effect. To find the microstructural causes for the persisting difference in flow stress between the deformation modes would be helpful for the explanation of the differences in recrystallisation properties. Although the estimated error in flow stress resulting from deviations in the deformation conditions are not very large, they are of a magnitude that is sufficient to close the gap in flow stress between cyclic and monotonic torsion. Still, regardless of the cause, the difference in flow stress between cyclic and monotonic torsion should be followed by a difference in microstructural parameters as well. However, because of the relatively small difference in flow stress, the corresponding difference in the microstructural parameters may be too small to detect. In the

following the change in subgrain size and dislocation density required to explain the observed difference in flow stress will be calculated.

Boundary spacing

The boundary spacing is known to affect the flow stress. Nes and Marthinsen (2003) have suggested a relation between boundary spacing and flow stress contribution as described in eq. 6.2.

$$s = a_2 M G b \left(\frac{1}{d} + \frac{1}{D} \right) \quad (6.2)$$

With $M=3$ and $a_2=2$, an estimate of the required deviations in boundary spacing in order to produce the observed differences in flow stress may be obtained as shown in fig 6.3. Especially if the subgrain size is small, the figure shows that minor changes in the subgrain size may result in relatively large changes in flow stress. The maximum and minimum measured subgrain size for the two alloys are indicated in the figure. Based on these values, it is likely that if the whole difference in flow stress had been caused by difference in subgrain size, the difference in subgrain size would have been so large it would have been detected in the EBSD measurements. Still the measurement error is quite large. Thus, for the smallest observed differences in flow stress between cyclic and monotonic torsion the difference in subgrain size required for explaining such a difference is clearly within the error margin of the subgrain size measurements.

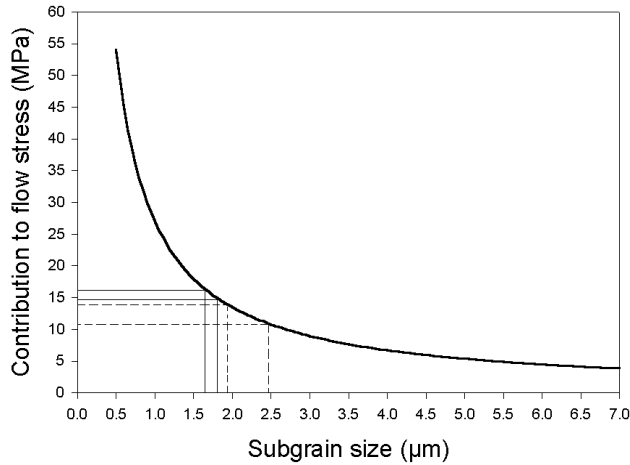


Fig 6.3: Contribution to flow stress from boundary spacing. Largest and smallest subgrain sizes and corresponding contributions to flow stress shown for AA1050 (dotted lines) and AA3103 (lines) deformed at 300°C and $\dot{\epsilon} = 1$

(ii) Internal dislocation density

According to Nes and Marthinsen (2003), the internal dislocation density influences the flow stress according to

$$\mathbf{s} = \mathbf{a}_1 M G b \sqrt{\mathbf{r}_i} \quad (6.3)$$

The internal dislocation density has not been measured in this study, and is therefore an element of uncertainty. Still, by the aid eq. 6.3 the required change in \mathbf{r}_i for a sufficient influence on the flow stress may be calculated with $M=3$ and $\mathbf{a}_1=0.5$. The result is shown in fig 6.4.

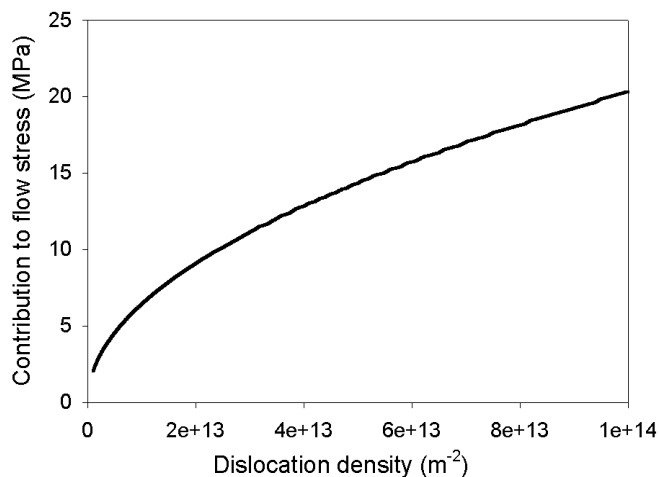


Fig 6.4: The influence on flow stress from internal dislocation density. Calculated from eq. 6.2.

Without experimental measurements of the dislocation density, it is of course difficult to evaluate to what extent the flow stress is influenced by changes in dislocation density. Still, fig. 6.4 shows that relatively small changes in the dislocation density may induce changes in flow stress exceeding 5 MPa. The change in the flow stress is especially rapid if the dislocation density is low. For an estimate of the effect of strain path changes on the dislocation density the results obtained in tension/compression by Zhu and Sellars (1996) are used as guidance. They observed that the dislocation density clearly decreased when the strain path was reversed, and the observed difference in dislocation density between tension and tension/compression was large enough to influence the contribution to the flow stress. (Fig. 2.9) At a net strain of 0.2 Zhu and Sellars measured dislocation densities of approximately $5.0 \cdot 10^{13}/m^2$ and $8.5 \cdot 10^{13}/m^2$ for cyclic and monotonic deformation respectively. As calculated from eq. 6.3 this corresponds to flow stress contributions of 14.3MPa and 18.7MPa respectively.

However, the difference in dislocation density between the strain paths seems to stabilize or decrease as the reversed strain is increased. For the large strain increments in the present study ($\epsilon=1.8$) it is therefore hard to say what the difference in dislocation density between cyclic and monotonic deformation will be. The results of Zhu and Sellars suggest that differences in dislocation density may be a contributing effect to the difference in flow stress between cyclic and monotonic torsion. Without experimental data it is however difficult to predict the magnitude of the contribution.

Taylor factor

The texture, and thus the Taylor factor, changes during deformation. Change in Taylor factor also means a change in flow stress. Driver and co-workers (Driver (1998)) studied the texture development in torsion, and developed a rate sensitive mixed slip model that was used to calculate textures based on slip on several systems. Driver also calculated the Taylor factors for various torsion texture components as shown in table 6.3.

Table 6.3: Taylor factors for torsion texture components and random orientation. (From Driver and co-workers)

	Random	C-component	B ¹ -component
\bar{M}	2.69	2.65	2.34

A transformation from random texture to pure B¹ component represents the full potential for reduction in flow stress due to texture development. Calculation shows such a transformation represents a reduction in flow stress of 13%, which would be sufficient for explaining the difference between cyclic and monotonic torsion. However, it is unlikely that texture is causing the difference in flow stress. The deformation textures are very weak both for cyclic and monotonic torsion, and the texture after cyclic torsion is very close to random. There is also hardly any

difference in the amount of B^1 -component between the deformation modes. It is therefore unlikely that there will be any large deviation in Taylor factor.

6.2 On the development of deformation texture

It has long been known that, even if the original grain shape is restored, reversing a torsion test to zero net strain does not restore the initial texture of the material. This was shown in the results of Rollett et al. (1988) in a study undertaken on recrystallised material. The deformation consisted of one torsion cycle. In this study, the samples were subjected to two successive torsion cycles. This extension of the experiment revealed some interesting facts. These discoveries are best shown by plotting the strength of the individual texture components as a function of cumulative strain in cyclic torsion, as shown in fig 6.6.

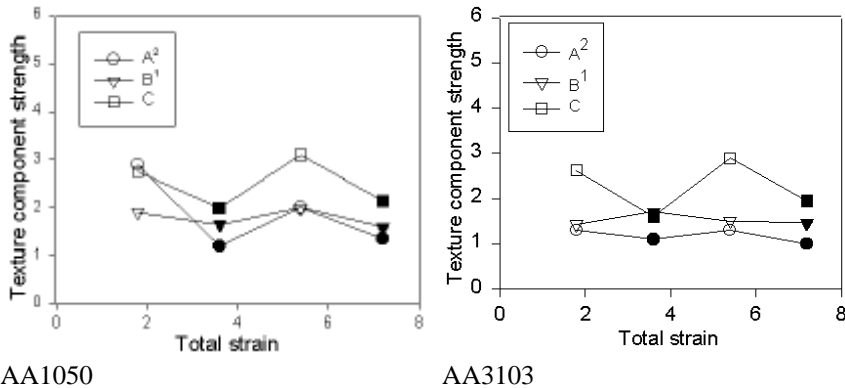


Fig 6.5: Strength of individual texture components after cyclic torsion. Filled symbols denote full reversal to starting position.

The sequence of four torsion steps could be viewed as three individual torsion experiments. All tests consisting of one full reversal, but with different starting material conditions. The three

situations with corresponding starting material conditions and texture development during the cycle are given in table 6.4. The results suggest that the texture development during the torsion cycle depends on the starting condition of the material. Starting at an as cast material state, a residual texture is left after one torsion cycle, while starting with a already deformed material yields a full reversal of the texture.

Table 6.4: Texture development in fully reversed torsion cycles.

<i>Strain interval</i>	<i>Material conditions at the start of the cycle</i>	<i>Net texture development after full cycle</i>
0 – 3.6	As cast, texture free	Residual texture left
1.8 – 5.4	Deformed, weak texture	≈ Full reversal of texture
3.6 – 7.2	Deformed, weak texture	≈ Full reversal of texture

Rollett et al.(1988) modelled the texture development of aluminium cylinders deformed in cyclic torsion to zero net strain using a Taylor based model. In contradiction to the experimental results, the model predicted full reversal to a random texture. Rollett concluded that the irreversibility of the texture could not be modelled simply by change in grain shape. The break up of the structure into subgrains with large misorientations between them was suggested as a reason for this. The current results support this suggestion. During the first deformation step, considerable break up occurs, as shown in fig. 5.13. Further deformation, either monotonic or cyclic, has only limited effect on the break up, compared to the major break up that occurs in the first torsion step. Thus, the failure to restore the random texture of the starting material after the first torsion cycle may be an effect of the introduction of additional high angle boundaries during deformation. Once the high angle boundaries are introduced, the texture development becomes reversible.

6.3 Recrystallisation

A key objective of this study is to explain the difference in recrystallisation behavior after cyclic and monotonic torsion. In the discussion of the results, some qualitative relationships will first be established based on the experimental observations. Then an attempt will be made to explain these observations in a more quantitative way by employing a recrystallisation model.

6.3.1 Driving pressure for recrystallisation

Difference in driving pressure after monotonic and cyclic torsion may explain the observed difference in recrystallisation properties. Traditionally, the explanations of strain path dependency of recrystallisation have been focused on differences in driving pressure as a result of the strain path change.

Driving pressure and flow stress

Difference in driving pressure between cyclic and monotonic torsion will cause a difference in recrystallisation kinetics and recrystallised grain size. The dislocation network providing the driving pressure also contributes to work hardening. Thus, the flow stress is a reasonable measure of the driving pressure. By plotting recrystallised grain size against the flow stress, as shown in fig 6.6, an indication of the dependence between driving pressure and recrystallised grain size may be obtained.

Part II: Strain path effect on recrystallisation after hot torsion

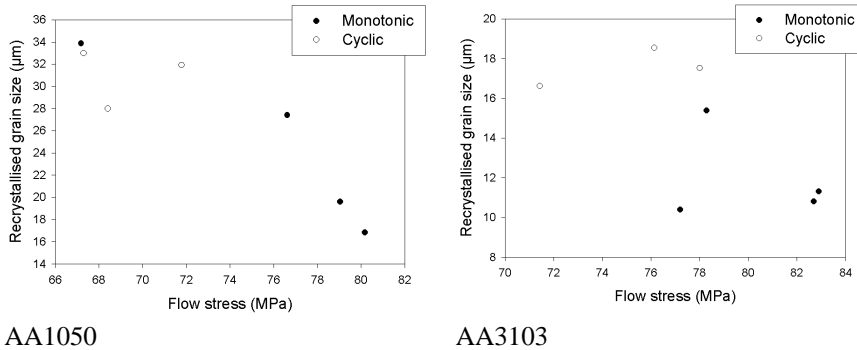


Fig 6.6: Recrystallised grain size as function of the flow stress.

For AA1050 a tendency of dependence between flow stress and recrystallised grain size may be spotted. A trend line could easily be inserted diagonally from the upper left corner. Still flow stress of 69MPa and 77MPa results in the same recrystallised grain size, so no firm conclusion can be drawn. For AA3103 a much weaker relationship between flow stress and recrystallised grain size is found as samples of similar flow stress produces different recrystallised grain sizes and vice versa.

Calculation of the driving pressure

The driving pressure may also be calculated from the quantitative measurements of the microstructure using eq. 2.9. As the dislocation density in the subgrain interior has not been measured, the empirical relationship connecting the interior dislocation density and the subgrain size proposed by Castro-Fernández et al. (1990) has been employed.

$$\sqrt{r_i} = \frac{C_d}{d} \tag{6.7}$$

This relationship is often referred to as the principle of similitude, and the constant C_d has been found to be in the order of 10 for aluminium alloys (Castro-Fernandèz, (1990)). It needs to be pointed out, however, that this is an approximation. It has been experimentally found that C_d does decrease with increasing Z . Employing the principle of similitude, the driving pressure may now be calculated, based on the measured microstructural parameters.

$$P_D = \frac{Gb}{\bar{d}} \left[\frac{b C_d^2}{2 \bar{d}} + \frac{3q}{4p(1-n)} \ln \left(\frac{eq_c}{q} \right) \right] \quad (6.8)$$

By closer examination of eq. 6.8 it turns out that the value of C_d does not affect the calculated driving pressure in the case studied, as the contribution from subgrain size and misorientation is several orders of magnitude larger than the contribution from internal dislocation density. This means that the internal dislocation density is of small importance in terms of influence on recrystallisation.

With the experimental subgrain size and misorientation data, the driving pressure is calculated. In fig 6.7 the results are displayed as a function of total strain for AA1050 and AA3103. There is a major difference in the development of driving pressure with total strain between the alloys. For AA1050 continuous increase in driving pressure is seen from $e=1.8$ to $e=5.4$ for both monotonic and cyclic torsion. At a total strain of $e=7.2$ there is a stagnation in the increase for the monotonically deformed sample, while the cyclic deformed sample shows a drop in driving pressure. For AA3103 the driving pressure is more or less constant with total strain, for both monotonic and cyclic torsion. The driving pressure is also larger for AA3103 than for AA1050. For both the alloys, the difference in driving pressure between cyclic and monotonic torsion is small. Thus the difference in driving pressure is probably not a major

contribution to the difference in recrystallised grain size between cyclic and monotonic torsion.

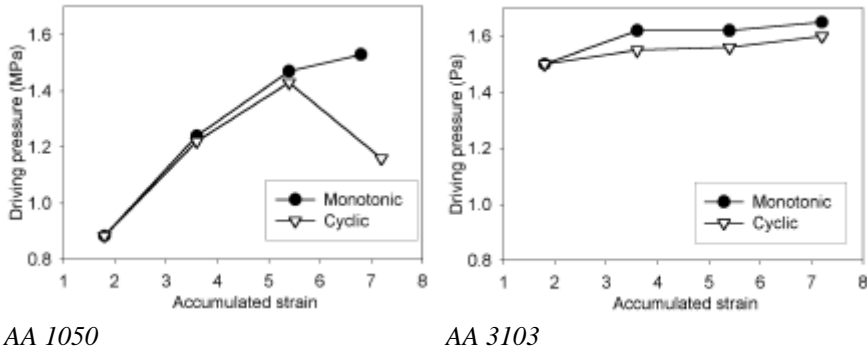


Fig 6.7: Driving pressure for recrystallisation as function of total strain for AA3103 and AA1050

6.3.2 Nucleation mechanisms

When differences in driving pressure fails to explain the full range of the observed difference in recrystallised grain size after cyclic and monotonic torsion, the attention has to be turned to the nucleation process. In the following the influence of strain path on the formation of nuclei will be discussed.

Nucleation at old grain boundaries

In the regions close to the original grain boundaries, orientation gradients will be present, creating possible nucleation sites. For the nucleation at grain boundaries a strain induced boundary migration type mechanism is assumed. Accordingly, the density of nuclei originating from the grain boundary regions is estimated by considering the area of old grain boundaries.

As seen from the micrographs of the as-deformed state, (fig. 5.7-5.9) the original grain shape is restored after full reversal in cyclic

torsion. The development of grain boundary area with strain will therefore be different for a cyclic strain path, compared to a monotonic. This difference in behavior is shown for deformation of an idealized circular grain in fig. 6.8.

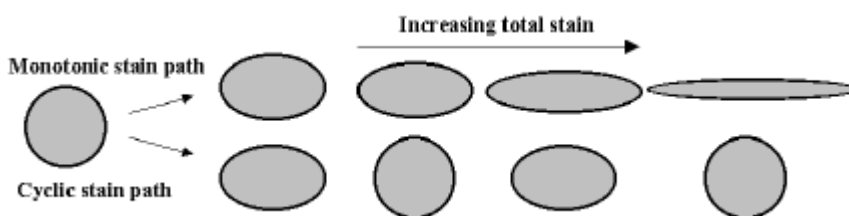


Fig 6.8: Deformation of a circular grain during cyclic and monotonic torsion.

It is obvious that, at a given total strain, the grain boundary area, relative to volume, will be larger after monotonic than cyclic torsion. The density of grain boundary nuclei will therefore be larger in the monotonic case, and will contribute to the smaller recrystallised grain size, seen after monotonic torsion.

Particle stimulated nucleation (PSN)

Nucleation from deformation zones developed around second phase particles will influence recrystallisation, especially in AA3103. In order to predict the variation of the density of PSN-sites with strain and strain path, a closer look at the mechanism behind the formation of the deformation zones is required.

Several models for the formation of the deformation zone exists, but as stated by Humphreys (1996): “The process occurs at a scale which is difficult to model successfully”. Still, if we base the description of the phenomena on a relatively simple model, the effect of strain reversals on nucleation from PSN may be estimated. The model is based on the theory that the deformation zone develops as the metal matrix rotates around the hard particles.

Repeated rotations generate an increasingly larger misorientation, as shown in fig. 6.9. As the deformation zones consists of geometrically necessary dislocations; it is reasonable to assume that reversing the direction of strain will result in annihilation of dislocations in the deformation zone. This will result in a weakening of the deformation zones, which in turn result in fewer sites with sufficient energy to nucleate recrystallisation, leading to a larger recrystallised grain size.

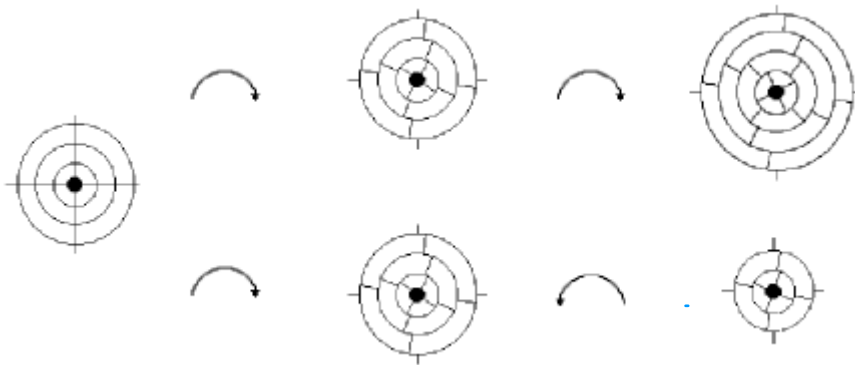


Fig 6.9: Development of deformation zones surrounding hard particles, in monotonic and cyclic deformation.

6.4 Modeling of recrystallisation after cyclic and monotonic torsion

6.4.1 The model

In order to quantify the effect of the proposed explanations for the observed differences in recrystallised grain sizes after monotonic and cyclic torsion, a recrystallisation model is applied to the results.

Pettersen (1999) developed a model for recrystallisation of aluminium deformed in torsion. The model is based on the model developed by Vatne et al. (1996a-d) to describe recrystallisation after plane strain compression. The model provides a method for predicting the number of possible nucleation sites formed during deformation, as well as the driving pressure for recrystallisation. The predicted number of nuclei, combined with their orientation, yields the recrystallised grain size and texture. A thorough description of the recrystallisation model for hot rolling is given in section 10.4. The most basic assumptions of the model are as follows:

- (i) Near site saturation kinetics applies.
- (ii) The nucleation sites are randomly distributed in space.
- (iii) The recrystallisation texture is a result of oriented nucleation.

These assumptions have been confirmed experimentally for AA3004 deformed in plane strain compression (Daaland and Nes (1996a-b), Vatne et al (1996a-d)), and are assumed to apply for the alloys and deformation modes used in this investigations as well.

Pettersen and Nes (2003a) assumed that the nucleation of recrystallisation after torsional deformation was fully described by four types of nuclei:

- (i) Nucleation at old grain boundaries
- (ii) Nucleation at large second phase particles
- (iii) Nucleation at Bs-oriented bands originating from Bs-oriented grains in the starting material.
- (iv) Nucleation from Bs oriented grains from small areas of the Bs orientation formed during deformation.

Pettersen and Nes (2003a) observed a strong Bs-component in the recrystallisation textures. In the present investigation, this component is virtually absent. Thus, the nucleation of recrystallisation is assumed to be fully described by sites of category i and ii.

6.4.2 Nucleation mechanisms

Nucleation from old grain boundaries

The density of nucleation sites in the grain boundary regions becomes:

$$N_{GB} = \bar{d} \cdot A(\epsilon) \cdot S_{GB}^* \quad (6.10)$$

$A(\epsilon)$ is the grain boundary area pr. volume as a function of strain, and \bar{d} is the average subgrain size. The product of the two yields the volume where nucleation may occur, as shown in fig. 6.10.

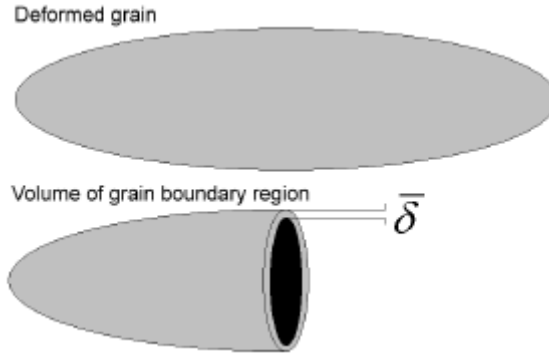


Fig 6.10: Volume of grain boundary region.

S_{GB}^* is the number of subgrains per unit volume in the grain boundary regions larger than the critical size of nucleation. The critical subgrain size is given by

$$d^* = \frac{4g_{GB}}{(P_D - P_Z)} \quad (6.11)$$

And the density of subgrain larger than the critical size for nucleation then becomes:

$$S_{GB}^* = \frac{1}{d^4} \int_{d^*}^{\infty} f(d) dd \quad (6.12)$$

The subgrain size data is described by a G -distribution of the following form (Vatne (1995), Vatne et al. (1996b)):

$$f\left(\frac{d}{\bar{d}}\right) = A\left(\frac{d}{\bar{d}}\right)^4 \exp\left(-B\frac{d}{\bar{d}}\right) \quad (6.13)$$

where A , B and n are constants determined from experimental subgrain size measurements, and \bar{d} is the mean subgrain size.

Using the \mathbf{G} -distribution in eq. 6.13, the integral in eq. 6.12 is solved, giving the following expression for the number of subgrains per unit volume larger than the critical size:

$$S_{Gb}^* = \frac{24}{\bar{d}_{Bs}^3} \frac{A}{B^5} \exp\left(-B \frac{d^*}{\bar{d}_{Bs}}\right) \left[1 + B \frac{d^*}{\bar{d}_{Bs}} + \frac{1}{2!} \left(B \frac{d^*}{\bar{d}_{Bs}}\right)^2 + \frac{1}{3!} \left(B \frac{d^*}{\bar{d}_{Bs}}\right)^3 + \frac{1}{4!} \left(B \frac{d^*}{\bar{d}_{Bs}}\right)^4 \right] \quad (6.14)$$

Introducing an expression for the change in area of the old grain boundaries with strain, the expression for the density of grain boundary sites can be written:

$$N_{GB} = C_{GB} \frac{2\bar{d} \cdot S_{GB}^*}{D_0} \left[\sqrt{1 + 3e^2} + \frac{1}{\sqrt{1 + 3e^2}} + 1 \right] \quad (6.15)$$

Where the symbols in the eq. are as previously defined. The constant C_{GB} is introduced as a modeling constant.

Strain reversals can easily be introduced in this eq. by defining ε as net strain in stead of accumulated strain in the cyclic case, as shown in table 6.5.

Table 6.5: Net strain and accumulated strain for cyclic torsion

Cyclic strain	Accumulated strain	Net strain
$\varepsilon=1.8-1.8$	3.6	$\varepsilon=0$
$\varepsilon=1.8-1.8+1.8$	5.4	$\varepsilon=1.8$
$\varepsilon=1.8-1.8+1.8-1.8$	7.2	$\varepsilon=0$

Particle stimulated nucleation (PSN)

When the particle size distribution $f(\mathbf{h})$, is given, the number of nucleation sites provided by particle stimulated nucleation can be calculated by the following eq.:

$$N_{PSN} = \frac{C_{PSN}}{\bar{\mathbf{h}}} \int_{\mathbf{h}^*}^{\infty} f(\mathbf{h}) d\mathbf{h} \quad (6.16)$$

Where C_{PSN} is a constant determining the average number of nuclei generated at each particle and \mathbf{h}^* is the critical particle size for nucleation to occur. An important step becomes choosing the correct value for the particle size above which nucleation occurs. Assuming conditions similar to cold deformation, the critical process will be the growth of the nuclei out of the deformation zones, and the critical particle size for nucleation will be given by eq. 2.12. During deformation at sufficiently low values of the Zener-Hollomon parameter, the formation of deformation zones around the particles will be retarded due to dynamic recovery, and the critical particle size will instead be governed by eq. 2.13. However, it has been estimated that for values of the Zener-Hollomon parameter exceeding $10^{12}/s$ nucleation is growth controlled (fig. 2.13) In the current study the Zener-Hollomon parameter is $10^{14}/s$, and it could safely be estimated that nucleation is growth controlled. Based on this, the density of PSN-nuclei may be calculated

$$N_{PSN} = C_{PSN} N_0 \exp\left(-\frac{4B\mathbf{g}_{GB}}{3(P_D - P_Z)}\right) \quad (6.17)$$

where $N_0 = A/(B\bar{\mathbf{h}})$ and \mathbf{g}_{GB} is the specific grain boundary energy which in the present investigation is set equal to 0.3 J/m^2 .

In this case, as the eq. for the density of nuclei does not include strain as a parameter, strain reversals are not as easily introduced as in the case of grain boundary nucleation. The only way to introduce dependence of strain path is through C_{PSN} . Such use of the tuning parameter must be done with caution.

6.5 Modelling of recrystallisation in AA1050 deformed at 300°C

As the fraction of large particles is relatively low in AA1050, it is reasonable to assume that nucleation from grain boundaries is dominating in this alloy. The first attempt was to model the recrystallised grain size, solely on basis of the difference in grain boundary area. The recrystallised grain size was tuned to the experimental for $e=1.8$.

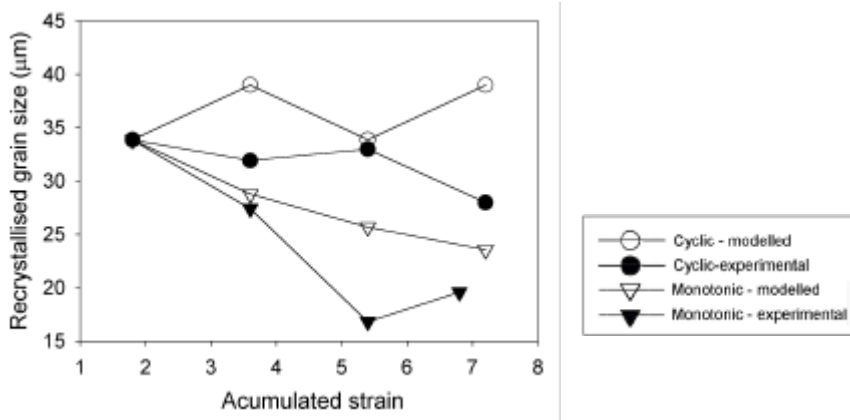


Fig 6.11: Recrystallised grain size for AA1050, modeled on the basis of difference in grain boundary area only. Compared to experimental results.

Fig. 6.11 shows a relatively good agreement between experimental and modeled results. The model tends to overestimate the grain size in both the monotonic and the cyclic case. By introducing the

measured variations of subgrain- size and misorientation with strain and strain path, both driving pressure, grain boundary volume and subgrain size distribution are affected. The resulting modeled grain sizes are shown in fig 6.12. The modeled results now fit the experimental data relatively well. It could be concluded that the difference in grain size as function of strain path in AA1050 could be explained as an effect of difference in grain boundary area. The contribution from the difference in driving pressure and subgrain size mainly alters the recrystallised grain size as a function of accumulated strain, and thereby improves the fit to the experimental data.

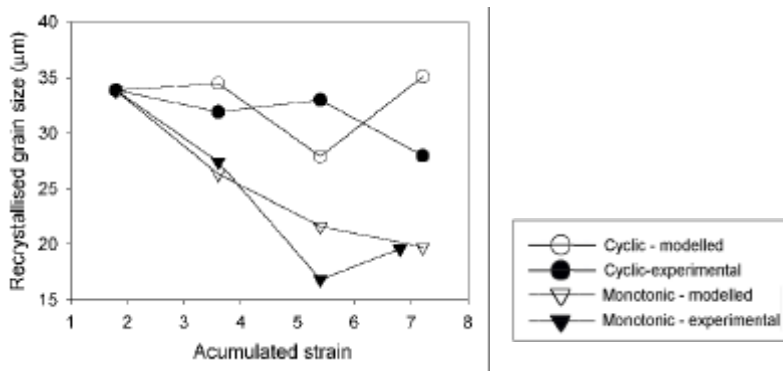


Fig 6.12: Recrystallised grain sizes for AA1050, modeled on the basis of calculated difference in grain boundary, area and experimentally measured differences in subgrain sizes and misorientations. Compared to experimental results.

6.6 Modeling of recrystallisation in AA3103 deformed at 300°C

In AA3103 particle stimulated nucleation has to be taken into account, as the alloy has a larger fraction of particles than AA1050. For the modeling of recrystallised grain size in AA3103 two vital parameters are unknown: Firstly, the ratio of GB-nuclei to PSN-

nuclei. Secondly, the effect of strain reversals on the density of PSN-nuclei. From the start, the density of PSN-nuclei is assumed *not* to be affected by strain path. Then the recrystallised grain size is modeled for various ratios of N_{PSN}/N_{GB} . This is shown in fig. 6.13 (a-d) where the ratio of PSN- to GB-nuclei is shifted from a dominance of GB to a dominance of PSN.

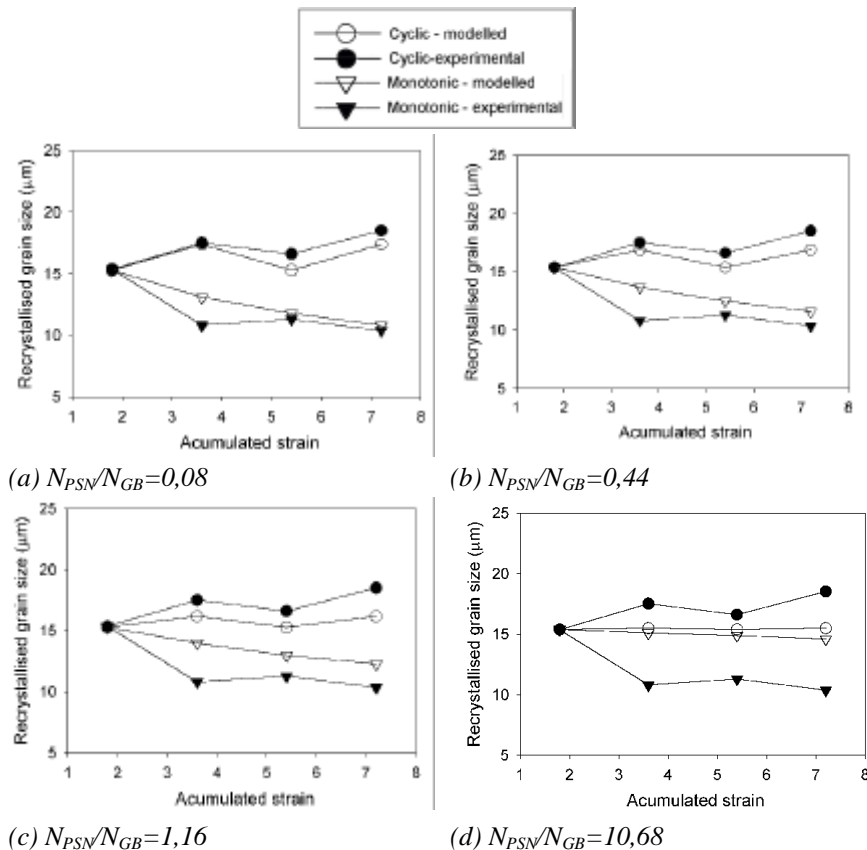


Fig 6.13: Modelling of recrystallised grain size in AA3103 deformed at 300°C. Increasing density of PSN-nuclei introduced from a-d. Compared to experimental results.

The results presented in fig. 6.13 could be interpreted in two different ways: The straight forward interpretation would be that our assumption that strain reversals does not affect PSN is correct,

and that nucleation from grain boundaries is totally dominating the recrystallisation process. The recrystallisation textures may however indicate that this is not the case. Retained deformation texture after recrystallisation is believed to originate from grains nucleated at old grain boundaries. For AA1050, there is a clear retained deformation texture present, especially at the two largest monotonic strains. For AA3103 almost no sign of retained deformation texture is visible. This may indicate that nucleation from grain boundaries is not the dominating nucleation mechanism in AA3103. However, if PSN is the dominating nucleation mechanism, fig. 6.14 c and d shows that the predicted difference in recrystallised grain size between cyclic and monotonic torsion will be too small – given that strain path is not assumed to affect the density of PSN-nuclei. No decisive conclusion regarding the effect of strain reversals on PSN can be reached, on the basis of the existing experimental data. However, some kind of strain path related effect on the density of PSN-nuclei seems to be present, maybe in the form proposed in fig. 6.9. This strain path dependence of nucleation may however also be a result of nucleation by PSN being enhanced in the areas surrounding grain boundaries (Bay and Hansen (1984))

6.7 Is the model valid for the present deformation conditions?

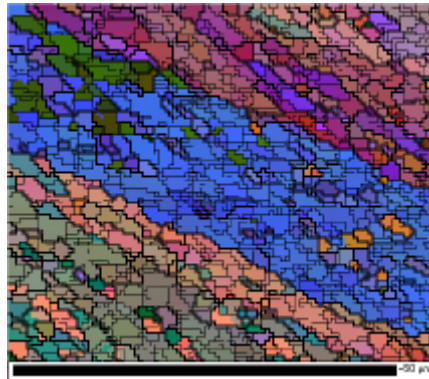
In the present investigation, the strain reaches very high values, and the microstructure undergoes major changes, including introduction of a large amount of new high angle boundaries. The recrystallisation model, presented in the previous chapters, has made good predictions for the recrystallised grain size after cyclic and monotonic torsion. Despite of the relatively well fitting modeling results, it is important to evaluate if the physical basis of the model still persists during the large changes of the microstructure.

6.7.1 Grain shape

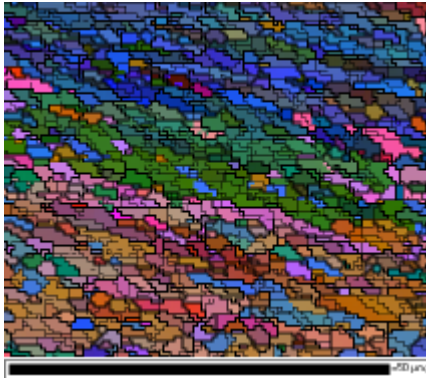
The mechanism for nucleation from grain boundary regions is based on a microstructure consisting of increasingly elongated grains, separated by high angle boundaries. Subgrains from the surface regions will have a misorientation advantage, and can grow into neighboring grains. It is however questionable if the microstructure at large strains have the characteristics required for the model.

AA3103

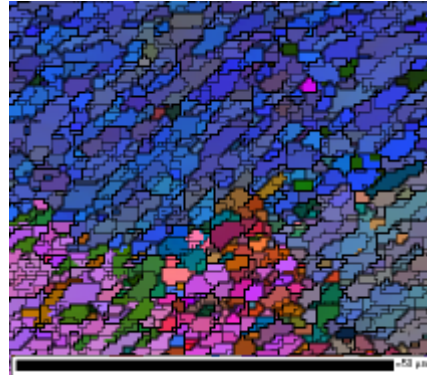
Fig. 6.14 (a) shows that the description from the model is present in the observed microstructure in AA3103 after a strain of $\epsilon=1.8$. Some short segments of high angle boundaries have developed within the bands, but low angle boundaries are dominant and the individual bands are easily distinguished. Increasing the strain to $\epsilon=3.6$ (fig. 6.14 (b)) the band structure is still present. But the fraction of high angle boundaries has shown a major increase compared to a strain of $\epsilon=1.8$. Still, the surface subgrains will clearly have a misorientation advantage if growing into neighboring bands. Going to a strain of $\epsilon=7.2$, heavy break up is seen in the microstructure. Some short bands consisting of subgrains of similar orientations are however still seen. But such a magnitude of the strain is clearly bordering the limits of the model – at best. However, the model clearly picks up the difference between cyclic and monotonic torsion. Looking at fig. 6.14 (c) and (e) it is clear that, compared to monotonically deformed material, a much smaller fraction of the subgrains have a misorientation advantage in the cyclically deformed samples. The microstructure of the sample deformed to a strain of $\epsilon=1.8-1.8+1.8-1.8$ also indicates that the microstructural basis of the proposed model is present for large strains in cyclic torsion.



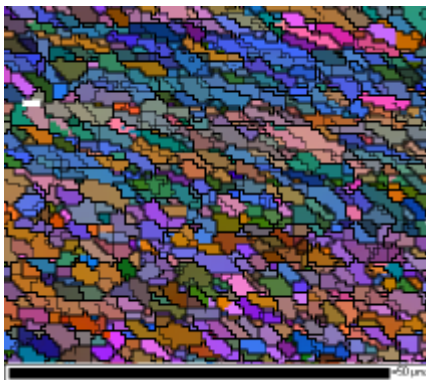
(a) $\epsilon=1.8$



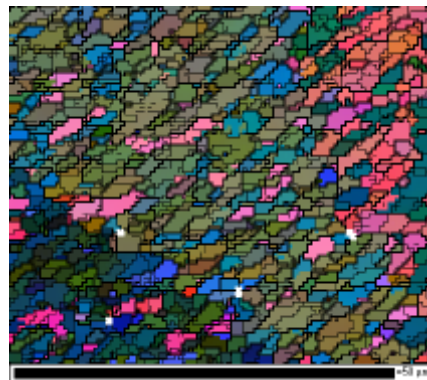
(b) $\epsilon=3.6$



(c) $\epsilon=1.8-1.8$



(d) $\epsilon=7.2$



(e) $\epsilon=1.8-1.8+1.8-1.8$

Fig 6.14: Selected strain states of AA3103 deformed in cyclic and monotonic torsion.

AA1050

To visualize the differences between the alloys, two examples of deformation microstructures for AA1050 are shown. The major difference between the alloys is the initial grain size, which is somewhat larger in AA1050 than in AA3103 (135 μm and 82 μm respectively). The larger initial grain size means that AA1050 could be deformed to higher strains without pinching of the elongated bands. This is clearly visualized in fig. 6.15a.

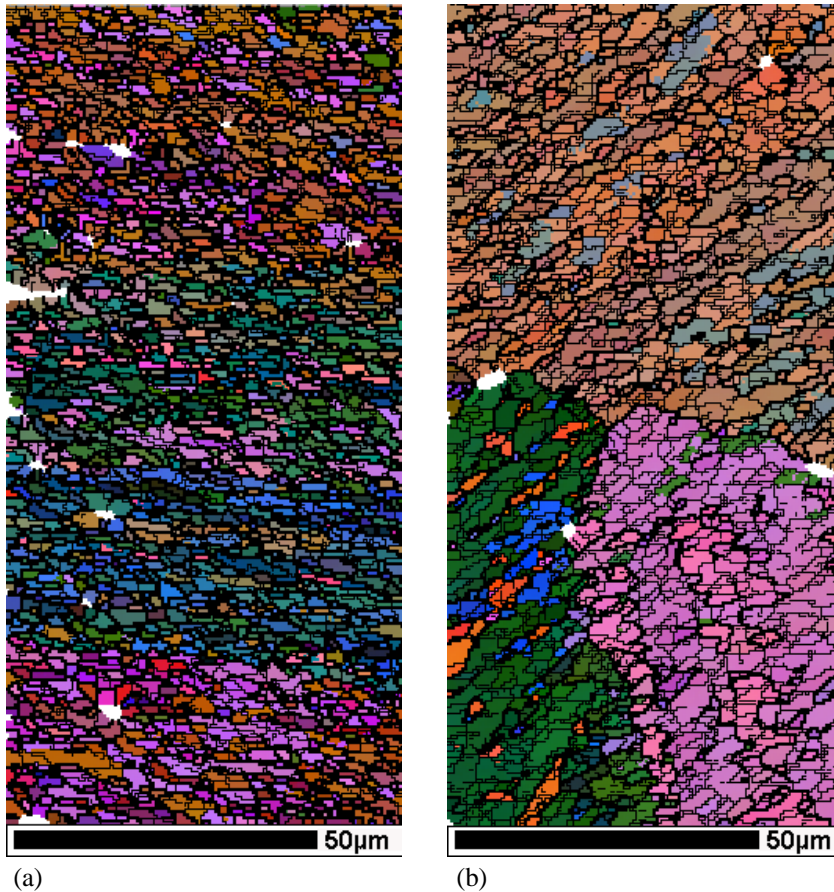


Fig 6.15: Microstructure of AA1050 deformed to $e=5.4$ (a) and $e=1.8-1.8$ (b)

Although the microstructure to a large extent consists of high angle boundaries, the band structure is still clearly visible and surface subgrains will have a growth advantage. This suggests that the proposed mechanism of the recrystallisation model may persist all the way up to the largest strains in AA1050.

6.7.2 Break up of second phase particles

The dependence on strain of the size distribution of second phase particles is not investigated in this study. At high strains and Zener-Hollomon parameters the particle distribution is known to change, resulting in a decreasing number of large particles. This was confirmed experimentally by Pettersen (1999) for AA 6060. Pettersen found that the particle distribution changed only marginally for values of the Zener-Hollomon parameter lower than $10^{13}/s$, and at strains of $\epsilon=1$ and $\epsilon=1.5$. Still, at $Z=10^{11}/s$ the particle distribution changed swiftly as strains were increased from $\epsilon=1$ to $\epsilon=5$. For this study, this means that the contribution of PSN at high strains may be overestimated. This is especially the case for AA3103. Still it should be kept in mind that the driving pressure at these strains is very high, and during the modeling the number of PSN nuclei is to a large extent limited by the value of C_{PSN} . Thus it also turns into a question of whether C_{PSN} is also constant during deformation. However, break up of second phase particles would not contribute to the difference in recrystallised grain size between the strain modes. The break up is likely to be largest during monotonic strain, and will thus rather even the differences in recrystallisation characteristics than increase them.

6.7.3 Geometric dynamic recrystallisation

At large strains geometric dynamic recrystallisation may replace traditional nucleation and growth. To investigate if this mechanism

is likely to occur, the distance between high angle boundaries is calculated from equation 3.7 and plotted against the twice the experimentally measured subgrain sizes as shown in fig 6.16. Due to serrated grain boundaries, the grains are assumed to break up when the subgrain size is the half of the distance between high angle boundaries. Based on the calculations, GDRX does not seem to be a possible mechanism for either of the alloys. However, the possibility is somewhat larger for AA3103 because of the smaller initial grain size. As the distance between high angle boundaries will be much larger in cyclic torsion, GDRX is not a possible recrystallisation mechanism in this case.

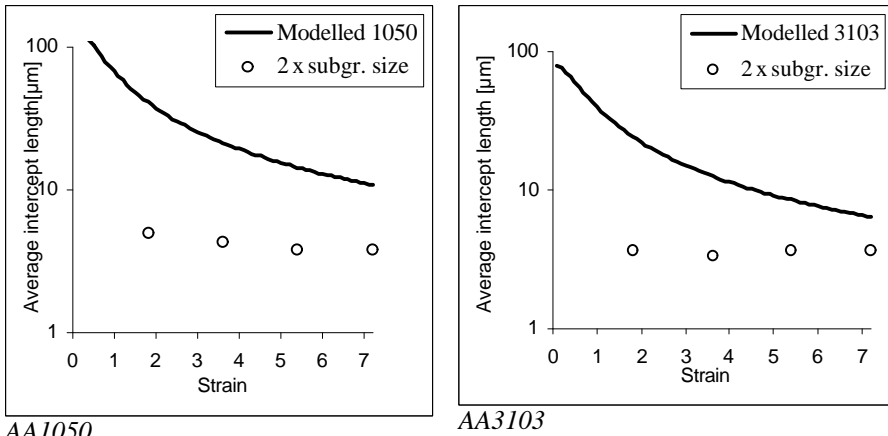


Fig 6.16: Calculated subgrain sizes compared to 2 x experimentally measured values. The criteria for GDRX.

Chapter 6: Discussion

7 Conclusions

Hot cyclic and monotonic torsion have been carried out for AA1050 and AA3103 alloys. The monotonic strains were $\epsilon=1.8$, $\epsilon=3.6$, $\epsilon=5.4$ and $\epsilon=7.2$. Torsion to cyclic strains of $\epsilon=1.8-1.8$, $\epsilon=1.8-1.8+1.8$ and $\epsilon=1.8-1.8+1.8-1.8$ were carried out for comparison. Flow stress and the development of deformation microstructure have been studied, as well as the subsequent recrystallisation process. The work has led to the following conclusions:

1. The monotonically deformed samples were found to change shape during deformation, and the flow stress had to be corrected for this. After correction for shape change, the flow stress after monotonic torsion was consequently found to be larger than that after cyclic torsion.
2. The Bauchinger effect was seen after the strain reversals, but the magnitude differed for the different strain reversals.
3. After cyclic deformation to zero net strain, the grain shape and particle distribution of the undeformed material was seen to reappear.
4. No difference in subgrain size as function of strain path was found, but the subgrain misorientation was larger after monotonic deformation compared to cyclic deformation to the same net strain.
5. No conclusion was established regarding microstructural causes for the observed difference in flow stress.

6. The distance between high angle boundaries in the deformed material was larger for monotonic deformation. However the large break up of grains was seen for both strain paths.
7. A weak residual texture was seen after the first full reversal in cyclic torsion. For full torsion cycles, starting at an already deformed state, a more complete restoration of the texture was seen.
8. The recrystallised grain size was larger after cyclic torsion, compared to equal cumulative monotonic strains.
9. Based on the microstructural investigations, the difference in driving pressure between cyclic and monotonic torsion was not found to be of sufficient size to explain the observed difference in recrystallised grain size between the deformation modes.
10. A relationship between recrystallised grain size and final flow stress during deformation was found for AA1050, but not for AA3103.
11. Effect of strain path changes on nucleation mechanisms was seen as the major cause for the difference in recrystallised grain sizes.
12. According to the observations of restoration of grain shape during cyclic torsion, a mechanism based on difference in grain boundary area as function of strain path was suggested and implemented in an existing recrystallisation model. This mechanism explained the difference in recrystallised grain size observed in AA1050.

13. For AA3103 an additional mechanism, reducing the density of PSN-nuclei, was proposed. The mechanism is based on weakening of deformation zones surrounding second phase particles during cyclic deformation.

Chapter 7: Conclusions

Part III:

Recrystallisation after single pass hot rolling

8 Purpose and outline of the experiment

8.1 Purpose and motivation

In industrial production processes, increasingly more accurate control of microstructural and mechanical properties of the products is required. In this context, to be able to predict and control the recrystallisation properties is crucial. It has long been known that changing the strain path during deformation affects the mechanical properties and the microstructure. More recent studies have also shown that such changes in strain path affect the subsequent recrystallisation process. These experiments have however been carried out under idealized conditions, with texture free materials and clearly defined strain path changes as torsion/reversed torsion and tension/compression.

Recrystallisation after hot rolling is a relatively complex process. The deformation conditions differ through thickness, because of difference in the magnitude of strain and strain rate as well as temperature gradient due to cooling from the roll surface. The distribution of second phase particles will also be affected by the difference in deformation conditions, and difference in the solid solution levels may also occur. All these aspects lead to non-homogenous recrystallisation properties through thickness. An additional contribution to this through thickness variation in recrystallisation properties is a strain path effect caused by the reversed shear strains in the surface regions. Parts of the slab also experience a combination of shear deformation and plane strain compression, and the effect on the recrystallisation process of this interaction in between strain modes is also uncertain. The purpose

of this study is to investigate the hot rolling process and the subsequent recrystallisation process. An important goal is to separate and determine the governing mechanisms of the recrystallisation process, with special focus on the reasons for the microstructural gradients observed through the thickness of the slab after recrystallisation. Potential effects of strain path changes will be a central aspect in this investigation.

8.2 Outline of the experiment

The task of confirming the presence of strain path effects during annealing after hot rolling is far from simple. In order to investigate the possible existence of strain path effects on recrystallisation after hot rolling, a combination of experimental studies and modeling is used, as described in fig. 8.1.

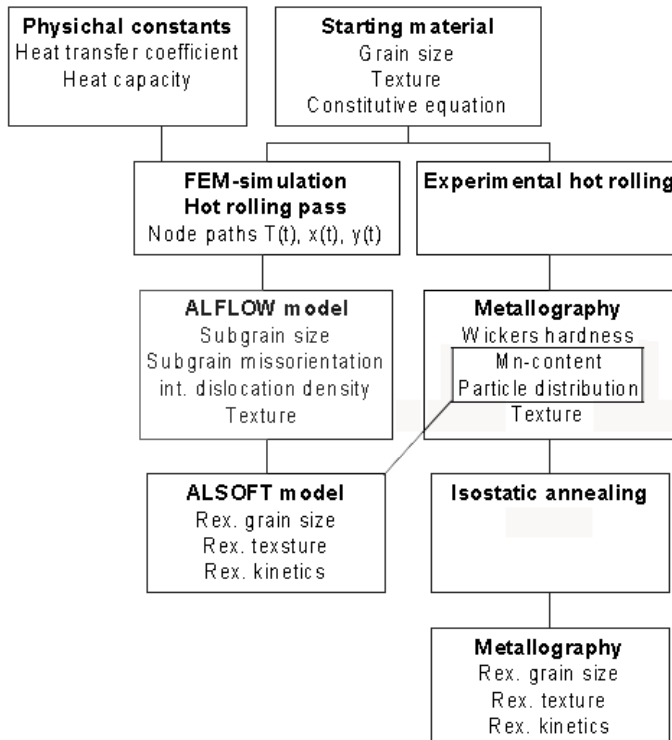


Fig 8.1: Schematic outline of the hot rolling experiment

The hot rolling process and the subsequent annealing are thoroughly studied. The through thickness properties of the material are characterized after each process, and during the annealing. Thus, knowledge of the as deformed microstructure and the recrystallisation process is obtained. Parallel to the experimental investigations of the hot rolling pass and the annealing, the microstructural development is predicted by the aid of FEM-simulations and models for microstructure development during deformation and recrystallisation. This series of simulations and modeling operations is performed as outlined below:

- The hot rolling pass is simulated, using an FEM-code. The input to the FEM-analysis is the constitutive equation of the material (derived from experiments), physical constants (heat capacity), the geometry of the rolling mill and the boundary conditions between the roll and the material (friction conditions and heat transfer coefficient).
- The output from the FEM-simulations is the displacement of individual nodes during deformation, given as position (X,Y) and temperature as function of time. These data enables calculation of the Zener-Hollomon parameter.
- The corresponding microstructural evolution is calculated using the model presented in section 10.3, named *ALFLOW*. The output from *ALFLOW* is the subgrain size, the average sub boundary misorientation and the internal dislocation density.
- Given the initial texture, *ALFLOW* is also capable of predicting the texture development during the rolling pass.
- The *ALSOFT* model, to be presented in section 10.4, is used to predict the recrystallisation process in terms of kinetics, texture and grain size through thickness of the rolled slab. The input to *ALSOFT* is the microstructure and texture data from *ALFLOW*.

Chapter 8: Purpose and outline of the experiment

- Input data for the distribution of large second phase particles and Mn content through thickness is also required. These are obtained experimentally.

Any major trend differences between the results from the simulations/modeling and the experimental investigations may indicate that strain path effects are involved. The simulation and modeling tools are only to limited extent capable of including strain path effects on the prediction of the as deformed microstructure, and thus they are not able to predict the influence from the strain path changes on the number of nucleation sites. Thus, the comparison between experimental and modeling results may reveal information of the mechanisms behind the differences in recrystallisation behavior through thickness. In addition the experimental study itself will likely provide information of the as deformed material and the recrystallisation process.

9 The hot rolling process – background and previous work

9.1 The industrial hot rolling process

Industrial hot rolling is a multi step process. The deformation is applied in a series of passes, separated by inter pass times. During the inter-pass time, the microstructure may be changing either by recrystallisation or recovery. This makes the industrial hot rolling process tricky to predict and model, as the microstructure consist of a mix of deformation microstructure, recrystallised material as well as recrystallised and rerolled areas. In the current study, only one rolling pass will be investigated. This makes modeling of the recrystallisation process much easier. Still, a brief introduction to the industrial hot rolling process is necessary. Hot rolling is separated in two processes: breakdown rolling and tandem rolling.

9.1.1 Breakdown rolling

During breakdown rolling, or roughing, the thickness of the initial ingot is reduced from approximately 550mm to 25mm. This is done on a reversing mill, in a number of passes. The breakdown rolling is characterized by low strains (0.06-0.5) and strain rates (1-10/s) per pass. The temperature during breakdown rolling usually starts at 550°C and drops to approximately 450°C during the rolling process. The surface regions are cooled during each rolling pass due to the contact with the rolls, and heats up during the inter pass time. In the start of the process, when the ingot is relatively short, the inter-pass time is governed by the time it takes to reverse the rolls; in the order of 10 seconds. As the slab increases in length the rolling process is the step, determining the inter-pass time. The ends of the slab then experiences alternating short and long inter pass times, depending on the current rolling direction. At the end of the breakdown rolling

process, the ends of the slab are cut off as they may result in surface defects. Because of the cutting time, the inter-pass time may reach 180 seconds.

9.1.2 Tandem rolling

Tandem rolling is characterized by larger strains (approximately 1) and strain rates (10-100/s) per pass. This also results in fewer passes and shorter inter-pass times, typically 1-3s. In tandem rolling, all the rolling passes are in the same direction, and the slab is coiled after the process. To obtain a fully recrystallised structure, the coil may be annealed. This is done, either by leaving the coil to cool, or by furnace annealing. In tandem rolling the entrance temperature is normally 400-450°C and the exit temperature 300-350°C.

9.2 Mechanical description of the hot rolling process

9.2.1 Strain and strain rate

For a material deformed under plane strain conditions, the plane strain is given as

$$\mathbf{e}_{ps} = \ln \frac{h_f}{h_0} \quad (9.1)$$

where h_f and h_0 are the final and initial thickness of the slab. Assuming plane strain and applying von Mises criterion, the true strain may be calculated

$$\mathbf{e} = \frac{2}{\sqrt{3}} \ln \frac{h_f}{h_0} \quad (9.2)$$

Eq. 9.1 assumes homogenous distribution of strain through the thickness of the specimen. However this is not the case. Close to the center of the slab, the material undergoes plane strain compression. At the surface, sticking between the rolls and the slab causes heavy shearing. In the intermediate regions, the material undergoes a combination of plane strain compression and shear. The distribution of strain and strain rate through thickness is mainly a function of the reduction and the roll radius.

Backhofen (1972) defined a ratio, namely the mean zone thickness/contact length ratio) Δ to describe this variation of strain and strain rate through thickness.

$$\Delta = \frac{\bar{h}}{\sqrt{R(h_0 - h_f)}} \approx \sqrt{\left(\frac{h_0 \cdot h_f}{R(h_0 - h_f)} \right)} \quad (9.3)$$

where h_0 and h_f is the initial and final thickness of the slab, \bar{h} is the geometric average thickness of the slab and R is the roll radius. The value of Δ is closely related to the development of deformation textures, and for laboratory purposes it is therefore important to choose thickness and roll radius so that the value of Δ equals the industrial process that is to be simulated. Beynon and Sellars (1992) have developed an empirical equation to describe the effective strain as a function of the roll radius (R) and the fractional distance from the rolling midplane (X/h_f), where X is the distance from the midplane.

$$\text{effective strain} = e \left[1 + 1.67 \left(\frac{h_f}{R} \right)^{0.5} \left(\frac{X}{h_f} \right)^2 \right] \quad (9.4)$$

An experimental technique for measuring the variation of net strain through thickness is insertion of marker pins in the rolling slab. The angle between the marker pins and the normal direction determine the shear at the various positions through thickness. Saito and coworkers (Sakai et al. (1988)) have developed an equation for calculation of the effective strain as a function of the angle of the marker pins.

$$effective \ strain = \frac{2e}{\sqrt{3}} \left[1 + \left(\frac{(1-r)^2 \tan \mathbf{q}}{r(2-r)} \right)^2 \right]^{\frac{1}{2}} \quad (9.5)$$

where r is the fractional rolling reduction and \mathbf{q} is the angle between the marker pins and the normal direction.

As for the strain, the strain rate also changes through thickness. The friction conditions plays a major role determining the near surface strain rates. Equations exist for calculation of surface strain rates. For calculation of strain rates through thickness of the slab, FEM simulations are required.

9.2.2 Surface shear

As the rolling slab changes thickness during the rolling operation, the surface speed of the slab also naturally changes during a rolling pass. As shown in fig. 9.1 in the beginning of the pass, the surface of the rolls will have a higher speed than the slab, resulting in a surface shear stress. The difference in speed will decrease until it reaches the same level as the roll speed at the neutral point (N). From the neutral point to the exit, the speed of the slab continues to increase, giving rise to a surface shear of opposite sign.

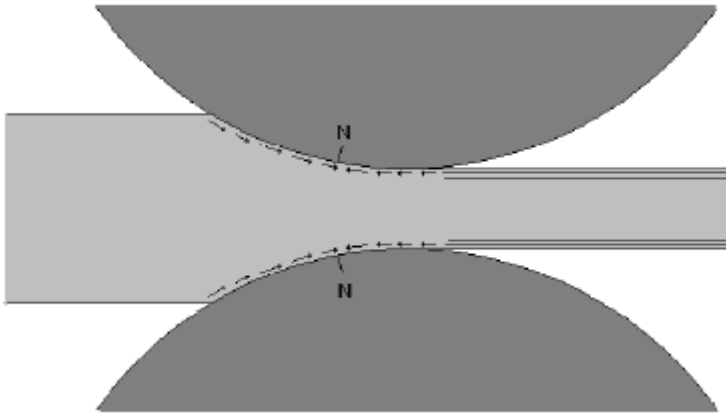


Fig 9.1: Reversal of surface shear in a hot rolling pass.

While the center of the slab is deformed in almost pure plane strain compression, the surface regions are subjected to a more complex strain history. Firstly the surface regions experiences a combination of plane strain compression and shear. Secondly, the shear is reversed during the hot rolling pass. For the case of breakdown rolling the rolling direction is changed for each pass, creating an additional reversal effect, generating an even more complex strain path.

9.3 The hot rolled material – properties through thickness

During a hot rolling pass there is a great difference in the thermo-mechanical influence through the thickness of the slab, as temperature, strain, strain path and strain rate are all changing through thickness. This is of course affecting the through thickness microstructural properties, as well as the concentration of alloying elements in solid solution and the size distribution of large particles.

9.3.1 Microstructure

Higginson and Sellars (2002) measured the subgrain size and the internal dislocation density in hot rolled steel in the center of the slab and close to the surface. They found that the dislocation density was larger close to the surface, while no clear effect of position through thickness on the subgrain size was found. Robson and Prangnell (2002) measured the subgrain size and misorientation through thickness of an AA7050 plate, hot rolled from 500mm to 130mm. They found that the subgrain size decreased going from center to surface, while the subgrain misorientation increased. Thus, the driving pressure for recrystallisation increased from center to surface. Subgrain size and driving pressure is shown in fig. 9.2. Duan and Sheppard (2002) investigated the subgrain size through the thickness of a 25mm thick AA1100 slab, hot rolled to 20mm at 300°C and 500°C. For both deformation temperatures the subgrain size was found to decrease towards the surface.

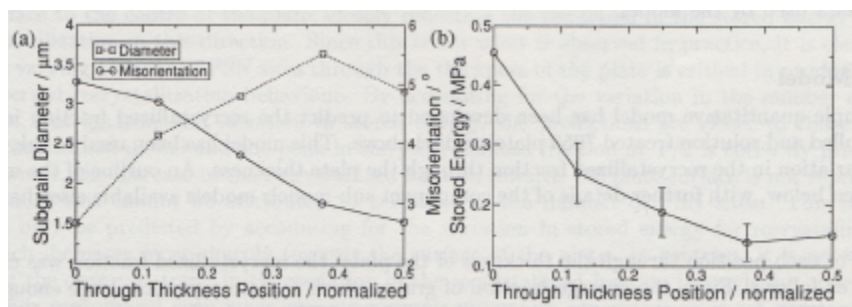


Fig 9.2: Subgrain size, internal dislocation density and calculated driving pressure through thickness of a hot rolled AA7050 plate. (Robson and Prangnell (2002))

9.3.2 Intermetallic particles and alloying elements

Robson and Prangnell (2002) also measured the total concentration of alloying elements as function of position through thickness of a hot rolled AA7050 plate. They found that with respect to most

alloying elements the plate was depleted in the center, and enriched halfway between the center and the surface. An exception was zirconium, where the concentration increased from surface to center. The size distribution of intermetallic particles larger than $5\mu\text{m}$ was also measured for positions in the center, the surface and halfway between center and surface. The fraction of large particles was seen to drop considerably at positions close to the surface, probably as a result of break up of hard particles due to the heavy surface shearing.

9.3.3 Strain path effects

A simple way to investigate the effect of strain path changes in hot rolling is to use a two pass rolling schedule. The strain path effect is achieved by rolling one of the samples the same direction in both passes (FF), while the direction of the other sample is reversed between the passes (FR). In hot rolling of steel, using such a schedule, Higginson and Sellars (2002) discovered that the internal dislocation density was smaller after a FR-rolling schedule compared to a FF-schedule. However, the change of strain path did not seem to affect the subgrain size.

9.4 Hot rolling textures

Compared to cold rolling, a more limited number of studies have been done on the subject of hot rolling textures. Still it is known that texture development during hot rolling is different from cold rolling. The texture development is also relatively unpredictable, depending on several factors such as preheating time and temperature, number of passes, rate of cooling and several other factors.

Cold rolling textures commonly consist of components like C (Copper) $\{112\} \langle 11\bar{1} \rangle$, S $\{123\} \langle 63\bar{4} \rangle$, B (Brass) $\{110\} \langle 1\bar{1}2 \rangle$

and some times Goss $\{110\} \langle 001 \rangle$ (fig 9.3). Maurice and Driver (1997) wrote a review article on hot rolling textures and found that hot rolling normally produced large increases in S and Brass components, together with some Cube. Experimental studies performed in plane strain compression, showed that the texture strength was affected by strain rate and temperature.

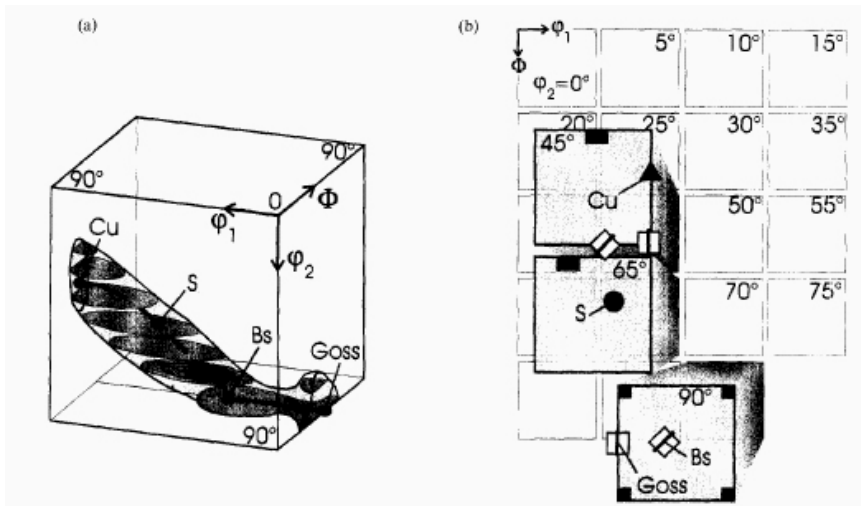


Fig 9.3: Major rolling texture components and their location in Euler space. (a) The **b**-fibre between Copper and Brass, and the **a**-fibre between Brass and Goss. (b) The constant j_2 sections.

Hot rolling generally results in heterogeneous texture through thickness of the slab. The surface regions normally show a sharp $\{001\} \langle 110 \rangle$ shear texture. The central regions deform in plane strain and develop a hot rolling texture. This is shown in fig 9.4. How deep the shear texture penetrates depends on the thickness of the slab. The penetration depth decreases with decreasing thickness.

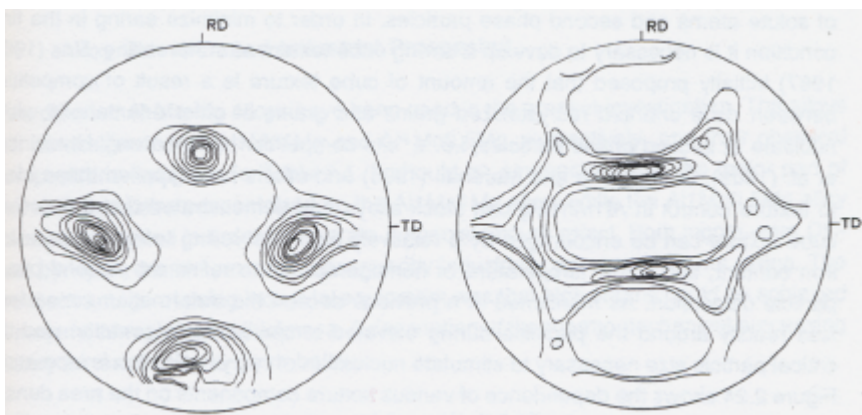


Fig 9.4: (111) pole figure from hot rolled commercial pure aluminium. Left: Surface of sheet. Right: center of sheet. (Dons and Nes (1986))

Using two pass FF and FR hot rolling, Higginson et al. (2003) investigated the strain path effect on texture development on three positions through thickness for an Al-Mn alloy. The major effect of the change in rolling direction was found in the surface region, where the shear texture component was considerably weaker after the FR schedule, compared to FF. For positions 20% into the half thickness and in the center plane there were only small differences in texture after changing of rolling schedule.

9.5 Recrystallisation after hot rolling

9.5.1 Recrystallisation after industrial hot rolling

In the present study, recrystallisation is studied after one pass deformation. As mentioned earlier, industrial hot rolling is a multistep process where recrystallisation frequently occurs between passes. This complicates the prediction of recrystallisation properties, as one has to include partly recrystallised areas receiving further deformation and subsequent recrystallisation.

9.5.2 Strain path effects

McLaren and Sellars (1992) and McLaren et al. (1995) modeled recrystallisation in steel. An Eulerian finite element model was used to predict temperature, strain rate and strain distribution. A finite difference model was used to calculate the temperature distribution and microstructural evolution during recrystallisation. The model predicted a maximum in the recrystallisation kinetics 20% into the half thickness of the slab, with more sluggish kinetics towards the surface and center. Changes in heat transfer coefficient and friction factor had only minor effects on the recrystallisation properties. Experimental studies showed changes in recrystallisation kinetics through thickness similar to those obtained from modeling, but with much smaller changes as shown in fig. 9.5. This deviation between experimental results and modeling was seen as a result of the use of equivalent strain in the calculations of recrystallisation kinetics, thus ignoring changes in strain path. Using two pass FF and FR hot rolling, the effect of strain path changes in hot rolling on subsequent recrystallisation may be determined. This was done by Higginson and Sellars (2002) for stainless steel and by Black et al. (2001) for an Al-Mn alloy.

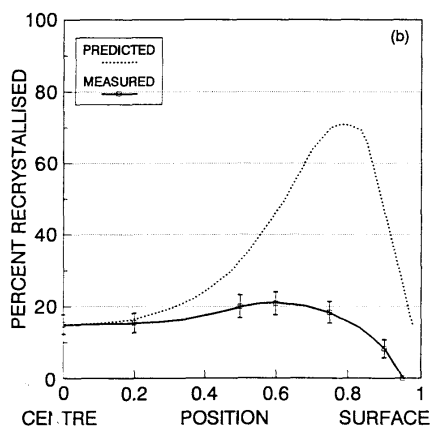


Fig 9.5: Predicted and measured fraction recrystallised for 318L stainless steel hot rolled and annealed at 900°C for 7200s. (McLaren and Sellars (1992))

For the Al-Mn alloy an almost linear increase in recrystallised fraction from center to surface were observed for both deformation modes. Still the kinetics was substantially slower for the FR rolling schedule. It is worth noting that this difference in kinetics was present all the way through thickness, not only in the sheared surface regions. The recrystallised grain size was also found to be larger after FR rolling schedule, compared to FF. These features were explained as a result of lower stored energy after the FR rolling schedule leading to fewer nucleation sites of sufficient energy, as well as lower driving pressure for subsequent growth.

For hot rolling of stainless steel a local maximum in the recrystallisation kinetics was observed 20% into the half depth. As seen in fig 9.6, the feature was most prominent after the FF rolling schedule, but may also be seen after the FR schedule. As for aluminium, the recrystallisation kinetics were slower after the FR rolling schedule. Based on measurements of subgrain size and internal dislocation density, the differences in recrystallisation kinetics between FF and FR rolling schedules was explained as a result of difference in driving pressure.

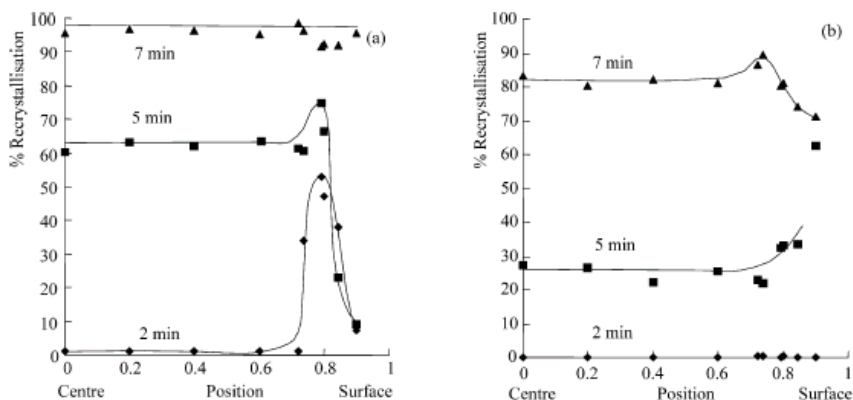


Fig 9.6: Recrystallisation kinetics for stainless steel after two-pass hot rolling in FF(a) and FR(b) mode. (Higginson and Sellars (2002))

9.5.3 Modeling of recrystallisation after hot rolling

Traditionally, models for prediction of recrystallisation have been empirical models predicting the time to 50% recrystallisation. These models usually take the initial grain size, forming temperature, strain and strain rate as input and are normally on the form:

$$t_{0.5} = aD_0^b \cdot e^{-c} \cdot Z^{-d} \left(\frac{Q_{rex}}{RT} \right) \quad (9.6)$$

where a , b , c , and d are constants. D_0 is the initial grain size, Q_{rex} is the activation energy for recrystallisation, R is the gas constant and T is the annealing temperature. Most of these models have been developed for steel, but have occasionally also been used for aluminium. (McLaren et al. (1995))

The major problem with the empirical models is the need for experimental tuning of the constants, and the lack of prediction power for other systems than those tested. In addition, empirical models do not describe the physics behind recrystallisation and do not take the origin of recrystallised grains into account. Vatne (1996 a-d) developed a physically based model for recrystallisation of aluminium after hot rolling, based on the calculation of the number of nucleation sites. The model, which in principle has predictive power both for recrystallised grain size and texture, will be described further in chapter 10.3.

10 Models used in this study

10.1 The motivation of model development

Microstructural modeling of metal fabrication processes is important for several reasons:

- Empirical methods without an understanding of the underlying mechanisms are no longer sufficient for further improvement of product quality and reduction of production costs.
- Microstructural models may give truly predictive capabilities in relation to the effect of process variables on subsequent processing and product properties in contrast to empirical relationships.
- Industrial tests are expensive and difficult to perform.
- Laboratory experiments are unable to reproduce all industrial conditions.
- Models are required in order to handle the complexity of industrial thermo-mechanical processing.
- Models may help initiate new experiments that will provide a more profound understanding of the mechanisms responsible for the microstructural changes.

In this context the objective of several research projects is the development of an integrated modelling approach which is capable of predicting the combined influence of all major process parameters during rolling, extrusion and subsequent annealing on the microstructure and hence the properties of the semi-finished products. This can be realised by the following combination of models: FE-models provide the complex strain paths and their spatial variations encountered under industrial processing conditions. These results are combined with a set of microstructure models, which link the evolution in microstructure (based on input

from the FE-models) in each stage of the production chain to preceding and subsequent production steps.

Over the last 10-15 years, NTNU/SINTEF has, in close collaboration with Hydro Aluminium, developed physically based microstructural models, which *in principle* have a predictive capability beyond the alloys and processing conditions for which they are developed. This includes the *ALSTRUC* model (Dons et al. (1999) Dons (2001)) which can provide the as cast and homogenised structure in terms of solid solution levels of alloying elements and the volume fraction and mean size of constituent particles and dispersoids. This is essential input to the work-hardening model *ALFLOW*, which together with an appropriate deformation texture model, describe the deformed state (basis for the subsequent annealing behaviour) in terms of dislocation densities, sub-grain size and volume fraction of different texture components. (Nes (1998), Marthinsen and Nes (2001), Nes and Marthinsen (2002)) The final annealing behaviour may be calculated with the *ALSOFT* model (Vatne et al. (1996 a-d)). This model calculates the annealing behaviour after hot or cold deformation in terms of kinetics, recrystallised grain size, and texture, and/or the combined effect of recovery and recrystallization on microstructure and properties during back-annealing after cold rolling.

In the following the FEM-model for the hot rolling pass as well as the employed microstructural models, namely *ALFLOW* and *ALSOFT* are described. In the current work, *ALSTRUC* is of less importance, and is not described further.

10.2 FEM-simulations

10.2.1 Constitutive equation

The equivalent stress as function of equivalent strain, is described by a Voce form of equation:

$$\mathbf{s} = \mathbf{s}_0 + (\mathbf{s}_s - \mathbf{s}_0) [1 - \exp(-\mathbf{e} / \mathbf{e}_r)]^m \quad (10.1)$$

where \mathbf{s}_0 is the initial flow stress, \mathbf{s}_s is the saturation or the steady state flow stress, \mathbf{e}_r is the transient strain constant, m is a constant of an order of ~ 0.5 , The parameters \mathbf{s}_0 , \mathbf{s}_s and \mathbf{e}_r can be expressed in terms of strain rate and deformation temperature as follows:

$$Z = A_1 (\sinh B_1 \mathbf{s}_0)^{n_1} \quad (10.2)$$

$$Z = A_2 (\sinh B_2 \mathbf{s}_s)^{n_2} \quad (10.3)$$

$$\mathbf{e}_r = A_3 + A_4 \mathbf{s}_s^2 \quad (10.4)$$

Where n_1 , n_2 , A_1 , A_2 , A_3 , A_4 , B_1 and B_2 are constants, and Z is the Zener Hollomon parameter as previously defined.

The constitutive equation for the material used in the calculation was developed from hot, plain strain compression tests on a Gleeble 3500, using a tool width to sample thickness ratio of 2. The plain strain compression results were checked against results from hot torsion, and a good fit was found. The result is given in table 10.1.

Table 10.1: Constants for constitutive flow stress relationship

\mathbf{s}_*	A	B	n	m	\mathbf{e}_r
\mathbf{s}_0	2.0×10^{11}	0.0625	6.8	0.25	$\mathbf{e}_r = 0.079 + 7 \times 10^{-5} \mathbf{s}_s^2$
\mathbf{s}_s	1.2×10^{12}	0.0208	5.5		

The physical properties of this alloy as a function of temperature are listed in table 10.2. The parameter values at intermediate temperatures are derived by linear interpolation.

Table 10.2: Physical properties of AA3104 used to run Marc for simulation

Temperature (°C)	Coefficient of thermal expansion ($\times 10^{-5}$) K ⁻¹	Specific heat (J kg ⁻¹ K ⁻¹)	Thermal conductivity (W/m K ⁻¹)	E (GPa)
20	2.2	900	173	71.8
100	2.39	938	176	68.8
200	2.43	984	182	65.1
300	2.53	1030	188	61.3
400	2.65	1076	192	57.6
500	2.82	1116	196	53.8

10.2.2 The FEM-analysis

As the rolling operation is performed at elevated temperature, a heat-transfer analysis is included and coupled with the deformation analysis. The temperature profile in the slab during hot rolling was calculated under the following assumptions:

- Since the length of the piece is much greater than either its width or thickness, modeling of this particular process can be reduced to a 2D approach.

- Oxide formation does not significantly affect the heat transfer between the strip and the work roll.
- The work rolls are assumed not to change in shape or size during the deformation process, and to remain perfectly spherical in cross section.

The mathematical model for a non-linear thermomechanical process is given by eq. 10.4-10.6.

$$K(u,T) \cdot u = f \quad (10.4)$$

$$U \mathbf{r} C_p \frac{\partial T}{\partial x} = \frac{\partial}{\partial y} \left(k \frac{\partial T}{\partial y} \right) + \dot{q} \quad (10.5)$$

$$\mathbf{r}_r C_{pr} \frac{\partial T_r}{\partial t} = \frac{1}{r} \frac{\partial}{\partial r} \left(r k_r \frac{\partial T_r}{\partial r} \right) \quad (10.6)$$

Eq. 10.5 and 10.6 are the governing equation for heat flow in the slab and in the work roll, respectively. K is the material stiffness matrix, u is the nodal displacement vector, T is the nodal temperature, f is the prescribed force vector, k , C_p , \mathbf{r} are, respectively, the thermal conductivity, specific heat and the density of the slab. k_r , C_{pr} , \mathbf{r}_r are the thermal conductivity, specific heat and the density of the roll respectively. U is the strip entry velocity ($x = Ut$), \dot{q} is a heat-generation term representing the heat released due to plastic work and is given by:

$$\dot{q} = h s \dot{\epsilon} \quad (10.7)$$

where \mathbf{s} is the equivalent flow stress, $\dot{\mathbf{e}}$ is the equivalent strain rate, and h is the efficiency of conversion of strain energy to heat which is taken to be 0.95, as has been determined empirically for aluminium alloys. The finite element formulation of the mathematical model given by eq. 10.4-10.6 leads to a set of non-linear equations, which are solved in MARC through the full Newton-Raphson method. The flow formulation method and an Arbitrary Eulerian Lagrangian Technique are used. Continuum mechanics are employed as the deformation behaviour is on a macro scale. Due to symmetrical geometry, computations are carried out only for top half of the slab. The following boundary conditions are imposed:

- Symmetrical cooling occurs at the centerline of the strip, the temperature change in the work roll is confined to a thin layer ($d = 40$ mm):

$$t \geq 0, y = 0 \quad -k \frac{\partial T}{\partial y} = 0 \quad (10.8)$$

$$t \geq 0, r = R - 40 \quad -k_r \frac{\partial T}{\partial r} = 0 \quad (10.9)$$

Heat transfer between the strip and the work roll is given by eq. 10.10.

$$t \geq 0, y = Y(t)/2, \quad -k \frac{\partial T}{\partial y} = h_{con} (T_{strip} - T_{roll}) \quad (10.10)$$

- The heat transfer to the environment at surface boundaries exposed to air is given by eq. 10.11

$$t \geq 0, y = Y(t)/2, \quad -k \frac{\partial T}{\partial y} = h_{env}(T_{strip} - T_{room}) \quad (10.11)$$

where $Y(t)$ is the strip thickness at each zone.

- The velocity at the center of the strip in the y direction is zero due to the geometric symmetry.

$$t \geq 0, y = 0 \quad V = 0 \quad (10.12)$$

Initial conditions for the simulations are listed in table 10.3.

Table 10.3: Initial conditions for the simulations

Work roll Initial temperature (°C)	50
Environment sink temperature (°C)	20
Work roll thermal conductivity (W/m K)	36
Work roll heat capacity (N/mm ² K)	3.77
Film coefficient to environment (strip and roll) h_{env}	0.01
Contact heat transfer coefficient (roll) (kW/m ² K) h_{con}	20, 50 or 100

The method used to model the interface friction was the interface shear factor approach, whereby the magnitude of the frictional stress is dependent on the magnitude of the relative sliding between the work roll and the strip. The relation is written as:

$$f_s \cong -mk_s \left(\frac{2}{\mathbf{P}} \tan^{-1} \left[\frac{u_s}{u_0} \right] \right) \quad (10.13)$$

where f_s is the frictional stress, k_s is the shear strength of the work strip, u_s is the relative velocity between roll and work slab, u_0 is a

constant, usually at a value of $(0.01-0.1)u_s$. The interface shear factor, m , represents the ratio of the interface shear stress of the object being deformed to the actual material shear strength ($m = t_i / k_s$), where t_i is the interface shear stress.

10.3 The work hardening model – ALFLOW

The ALFLOW model (Nes (1998), Marthinsen and Nes (2001), Nes and Marthinsen (2002)) is used for predictions of deformation microstructure. It relies on a multi parameter description of the microstructure evolution, fig. 10.1. This is of course a simplified description of the microstructure, compared to the detailed characterisation presented in section 2.3. At small strains the stored dislocations are arranged in a cell structure characterised by a cell size d , cell walls of thickness h , a wall dislocation density r_w , and a dislocation density within the cells r_i . At large strains the cell walls have collapsed into sharp sub-boundaries of a well-defined misorientation, j . A total dislocation density in the material may then be derived:

$$r = r_i + \frac{k_0 j}{bd} \quad (10.14)$$

where k_0 is a geometrical factor of order 3. By using a fictitious misorientation at low strains:

$$j = \frac{a_2}{a_1} \left(\frac{a_2}{a_1 q_c} + 2 \right) \cdot \frac{b}{k_o} \sqrt{r_i} \quad (10.15)$$

eq. 10.14 may be applied to all strains. The evolution of these parameters with deformation and their influence on the flow stress will be presented in the following subsections. Some aspects of the

analysis are not unique for this model, but are used by several models.

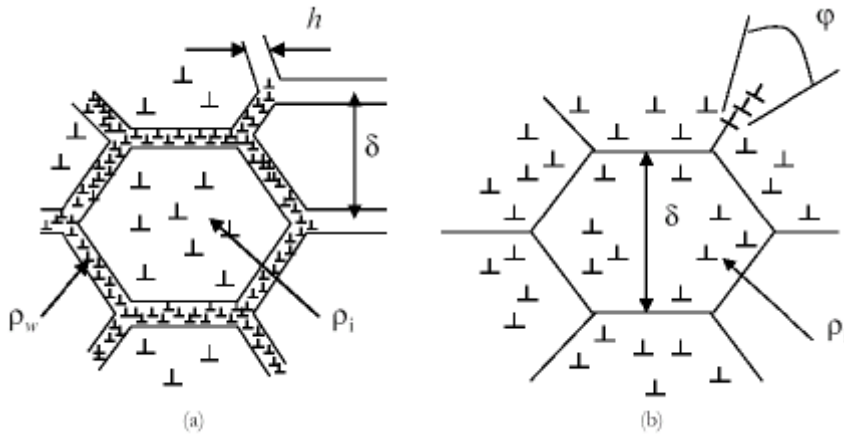


Fig 10.1: Schematic representation of the microstructural parameters used in the work hardening model. (a) Small strains, (b) large strains.

Flow stress

At a constant microstructure the flow stress is defined in terms of a thermal component, t_t , and an athermal component, t_a

$$t = t_a + t_t \quad (10.16)$$

Thermal component

The thermal component is due to short-range interactions between mobile and stored dislocations (cutting of “trees”), dragging of jogs and elements in solid solution. The stress is defined by the Orowan equation:

$$\dot{g} = r_m b v \quad (10.17)$$

where \dot{g} is the shear strain rate, r_m the density of the mobile dislocations and v the average speed of the mobile dislocations. The

density of mobile dislocations is expected to scale with the total dislocation density, i.e. that a fraction of all dislocations present in the material at any time are mobile. An estimate of $r_m = 0.1r$ is used in the model. Eq. 10.17 is then written in the following form:

$$2 \sinh \frac{t_t V_t}{kT} = \frac{\dot{\gamma}}{b^2 r_m B_t n_D} \cdot \exp\left(\frac{U_t}{kT}\right) \quad (10.18)$$

where V_t is the activation volume, U_t is an activation energy, T is the temperature, k is the Boltzmann's constant, n_D is the Debye frequency and B_t is a constant. In the case of a pure metal the activation energy is expected to be that required for dragging of jogs on screw dislocations, i.e. $U_t \mu U_{SD}$, the activation energy for self diffusion. The activation volume depends on the spacing of forest dislocations as $V_t = w_r b^2 r^{-1/2}$. In solid solution alloys, the activation energy is that required for separating the solute atoms from the climbing jogs, which depends on the activation energy for solute diffusion and the solute-dislocation interaction energy: $U_t = U_S + D U_S$. The activation volume scales with the spacing of solute atoms along the dislocation core, given by $V_t = w_r b^3 c^{-e}$. w_r and w_t are scaling factors which needs to be determined experimentally. More details may be found in the work by Nes and Marthinsen (2002).

The athermal component

The athermal component in eq. 10.16 characterises the rate and temperature independent interaction of dislocations with long-range barriers. These barriers are particles, sub-boundaries, grain boundaries and stored dislocation networks, and hence eq. 10.16 can be written as:

$$t = t_t + t_p + a_1 G b \sqrt{r_i} + a_2 G b \left(\frac{1}{d} + \frac{1}{D} \right) \quad (10.19)$$

Here \mathbf{a}_1 and \mathbf{a}_2 are constants of the order 0.3 and 2, respectively, $(1/\mathbf{d}+1/D)$ represents the average spacing of all boundaries, and \mathbf{t}_p is the contribution from non-deformable particles, given as the Orowan bypass stress i.e.

$$\mathbf{t}_p = \frac{AGb}{1.24 \cdot 2\mathbf{p}} \left[\frac{1}{\mathbf{l}} \ln \left(\frac{\mathbf{l}}{b} \right) \right] \quad (10.20)$$

where \mathbf{l} is the particle spacing in the slip plane, given the volume fraction f_r and radius r , of the particles (Brown and Ham 1971):

$$\mathbf{l} = 0.8 \cdot r \left(\sqrt{\frac{\mathbf{p}}{f_r}} - 2 \right) \quad (10.21)$$

It follows from eq. 10.19 that the dislocation substructure contributes both to the thermal and the athermal components. In the next sub-section the evolution of the microstructure is treated. The development of a microstructure during deformation is a result of two concurrent processes: athermal storage and dynamic recovery of dislocations. The evolution equation for each of the microstructural parameters are thus given by two terms: Net evolution = storage + recovery. Since three microstructural parameters are included (i.e. \mathbf{r}_i , \mathbf{d} and \mathbf{j}) a corresponding set of equations needs to be solved in order to obtain the microstructural development during deformation. These equations are:

$$\frac{d\mathbf{d}}{d\mathbf{g}} = \frac{d\mathbf{d}^+}{d\mathbf{g}} + \frac{d\mathbf{d}^-}{d\mathbf{g}} \quad (10.22)$$

$$\frac{d\mathbf{r}_i}{d\mathbf{g}} = \frac{d\mathbf{r}_i^+}{d\mathbf{g}} + \frac{d\mathbf{r}_i^-}{d\mathbf{g}} \quad (10.23)$$

$$\frac{d\mathbf{j}}{d\mathbf{g}} = \frac{d\mathbf{j}^+}{d\mathbf{g}} + \frac{d\mathbf{j}^-}{d\mathbf{g}} \quad (10.24)$$

While physically based expressions are deduced for the internal dislocation density and the subgrain size no such theory has so far been developed that accounts for the misorientation evolution. The sub-boundary misorientation, \mathbf{j} , is expected to reach a constant level of around 3-4° at the III-IV transition (fig. 2.8 and section 2.3). This observation is included as an empirical element in the model.

Athermal storage

The dislocations are stored in the material in three principal ways, see fig. 10.2:

- in the cell interior $\left(\frac{d\mathbf{r}_i^+}{d\mathbf{g}} \right)$
- by forming new cell-boundaries $\left(\frac{d\mathbf{d}^+}{d\mathbf{g}} \right)$
- in old cell-boundaries $\left(\frac{d\mathbf{j}^+}{d\mathbf{g}} \right)$

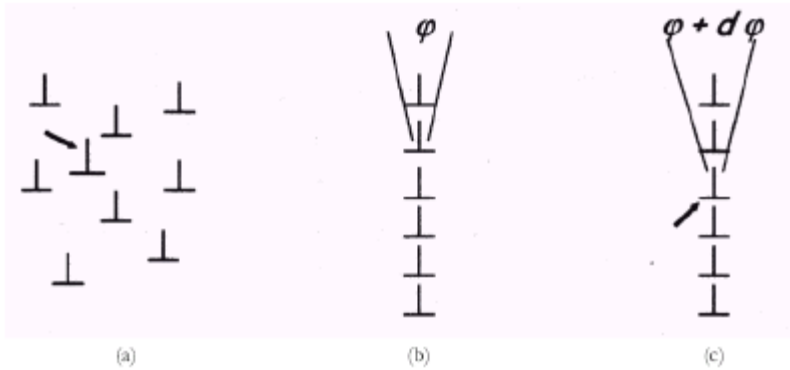


Fig 10.2: Three possibilities of dislocation storage. (a) In a Frank network in the subgrain interior, (b) in new cell boundaries, (c) in old cell boundaries.

A simple one parameter analysis of the storage problem gives the following expression:

$$\frac{d\mathbf{r}^+}{d\mathbf{g}} = \frac{2}{bL} \quad (10.25)$$

where L is the slip length. In a pure single crystal the slip length is limited only by the interactions between the mobile and forest dislocations, see fig. 10.3 (a), and the slip length is given by:

$$L = \frac{C}{\sqrt{\mathbf{r}}} \quad (10.26)$$

C is a constant proportional to $1/q_{II}$, where q_{II} is the stage II work hardening rate. In a polycrystalline alloy, also other barriers in the material will limit the slip length and affect the athermal storage rate, fig 10.3(b). An effective slip length L_{eff} is introduced including both stored dislocations, particles and grain boundaries.

$$\left(\frac{1}{L_{eff}}\right)^2 = \left(\frac{1}{C/\sqrt{r}}\right)^2 + \left(\frac{1}{L_G}\right)^2 \quad (10.27)$$

where the L_G term covers the “alloy barriers”:

$$\left(\frac{1}{L_G}\right)^2 = \left(\frac{1}{D}\right)^2 + \left(\frac{2f_r}{r}\right)^2 \quad (10.28)$$

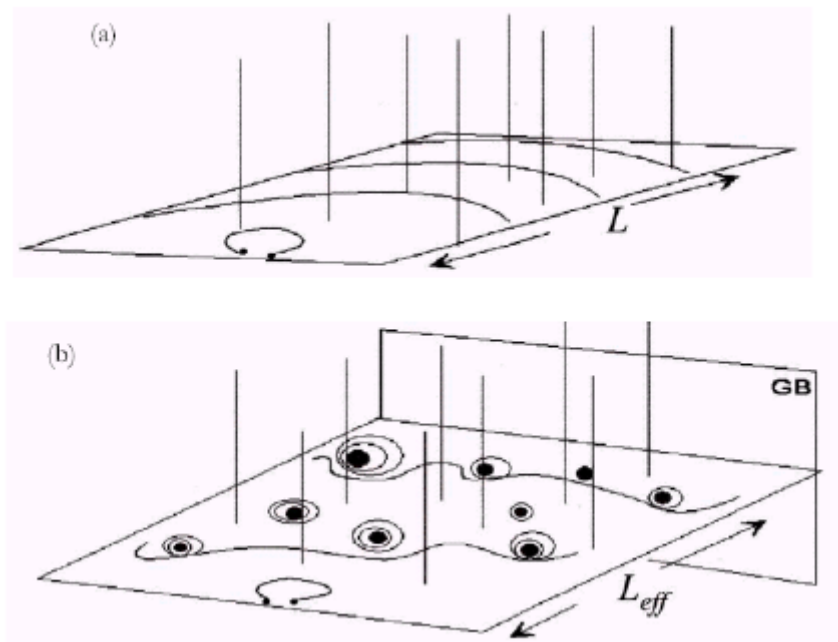


Fig 10.3: Difference in slip length restrictions between a pure metal (a) and an alloy containing particles and grain boundaries (b).

Because the storage pattern is more complex than eq. 10.25 indicates, a statistical analysis is developed which regulates the athermal storage through the following differential equation (Nes 1998)

$$\frac{d\mathbf{r}_{nb}}{d\mathbf{g}} = \frac{2S(1-f)L\mathbf{r}_i}{b} \quad (10.29)$$

where \mathbf{r}_{nb} represents the dislocations stored in new boundaries, S is a cell/sub-boundary storage parameter and f is the volume fraction of cell boundaries. During stage II this dislocation storage pattern is consistent with the principle of scaling, or similitude – a principle that implies that the microstructural elements scale with each other through three scaling constants:

$$q_c = \mathbf{d}\sqrt{\mathbf{r}_i}, \quad q_h = h/\mathbf{d}, \quad q_b = \sqrt{\mathbf{r}_b/\mathbf{r}_i} \quad (10.30)$$

and the storage parameter becomes

$$S = S_{sc} = \frac{fq_b^2}{2C^2(1-f)} \quad (10.31)$$

The resulting storage rate in the cell interior in stage II turns into a modification of eq. 10.25.

$$\frac{d\mathbf{r}_i^+}{d\mathbf{g}} = \frac{1}{1+f(q_b^2-1)} \cdot \frac{2}{bL_{eff}} \quad (10.32)$$

At constant strain rate and temperature, the transition from stage II to III is associated with a saturation of \mathbf{r}_i (Nord-Varhaug et al 2000) i.e a balance between athermal storage and dynamic recovery of dislocations in the cell interior. This means that eq. 10.22 equals zero, from which it follows that further hardening during stage III and IV requires continued storage of sub-boundaries. This follows from eq. 10.29 in the form:

$$\frac{d\mathbf{d}^-}{d\mathbf{g}} = -\frac{2SC^2\mathbf{d}^2}{\mathbf{k}\mathbf{j}L_{eff}} \quad (10.33)$$

where the storage parameter S now becomes a fitting parameter.

Dynamic recovery

By analysing the stability of the cell interior dislocations and the sub-boundary structure, two dynamic recovery processes are incorporated in the model:

- annihilation of dipole segments in the Frank network $\left(\frac{d\mathbf{r}_i^-}{d\mathbf{g}} \right)$
- subgrain growth $\left(\frac{d\mathbf{d}^+}{d\mathbf{g}} \right)$

In the pure metal case these stability problems are analysed in terms of thermally activated cross-slip and climb (Nes 1998, Marthinsen and Nes 2001). Dynamic recovery associated with a 3-D dislocation network will necessarily require both these reactions. In solute containing alloys the rate controlling reaction in cross-slip is assumed to be thermally activated glide of heavily jogged screw dislocations, rather than cross-slip. Recovery of cell-interior dislocation relies on the assumption that network growth is controlled by the collapse of dipoles of separation l_g . The dipoles are formed when mobile dislocations pass through the stored network, and l_g is expected to be much smaller than the average separation of stored dislocations. The collapse rate of dipoles will result in a recovery rate given by:

$$\frac{d\mathbf{r}_i^-}{dt} = -v_g \mathbf{r}_i \quad (10.34)$$

where ν_g is the dipole collapse frequency. The derived expression gives.

$$\frac{d\mathbf{r}_i^-}{d\mathbf{g}} = \mathbf{r}_i^{1+x} b^y l_a \mathbf{J} \mathbf{x}_r B_r \frac{\nu_D}{\dot{\mathbf{g}}} \left(\exp - \frac{U^*}{kT} \right) 2 \sinh \left(\frac{V_r G b \sqrt{\mathbf{r}_i}}{z k T} \right) \quad (10.35)$$

This equation covers three different cases, in which x , y , z , l_a , the activation volume V_p and the activation energy U^* , take different values.

- In pure metals $x= 1$, $y= 1$, $z = 1/2$, $l_a \gg b$, $V_r = \mathbf{x}_r b^3$ and $U^* = U_{SD} + \mathbf{D}U$
- In solid solution alloys with thermally activated glide, $x= 1/2$, $y= 0$, $z = 2\pi$, $l_a \gg b$, $V_r \mu \mathbf{x}_r b^3 c^{-e}$ and $U^* = U_S + \mathbf{D}U_S$
- In solid solution alloys with climb, $x= 1$, $y= 1$, $z = 1/2$, $l_a \gg b/c$, $V_r \mu \mathbf{x}_r b^3$ and $U^* = U_S + \mathbf{D}U_S$

The average subgrain size in a dynamic situation will increase at a rate

$$\frac{d\mathbf{d}^+}{d\mathbf{g}} = \frac{1}{\dot{\mathbf{g}}} \nu_D B_d b \cdot \exp \left(- \frac{U^*}{kT} \right) 2 \sinh \left(\frac{P V_d}{kT} \right) \quad (10.36)$$

where the activation volume is $V_d \mu b^3$ in pure metals and $V_d \mu \mathbf{x}_d b^3 c^{-e}$ in solid solutions. P is the driving pressure given by $P = 4\gamma_{sb}/\delta$, where γ_{sb} is the sub-boundary energy. \mathbf{x}_r , \mathbf{x}_d , B_r and B_d are constants that need to be determined experimentally see (Marthinsen and Nes 2001)

Application

The storage and recovery terms in eq. 10.22 and eq. 10.23 are now available, and together with the particle contribution in eq. 10.20 and the thermal component in eq. 10.8 it is possible to calculate the resolved shear stress, \mathbf{t} . In fig. 2.15 an example of the evolution of

r_i , d , j and t is given through stage II, III and IV into stress saturation at a constant strain rate and temperature. It shows that r_i increases rapidly in stage II, but remains constant during further deformation. The misorientation increases in stage II and III to a constant level in stage IV. The subgrain size decreases gradually all the way until stress saturation is reached. These evolution patterns are reflected in the resulting flow stress.

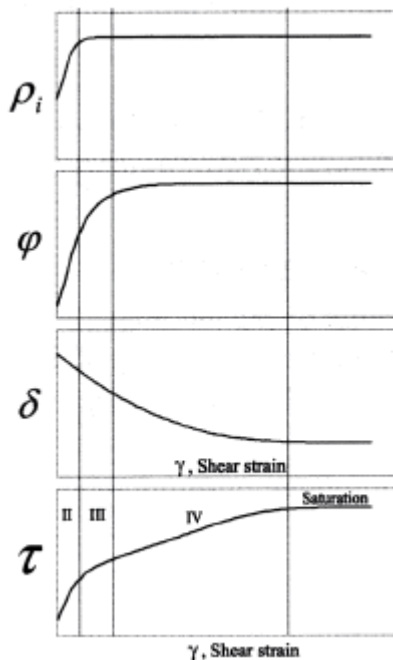


Fig 10.4: Schematic illustration of the evolution of microstructural parameters and flow stress for deformation at room temperature.

10.4 The softening model - ALSOFT

The softening model used in this study is the ALSOFT-model, developed by a group at NTNU in Trondheim. The model is a combined recovery and recrystallisation model. For a complete description of the model the reader is referred to Vatne et al. (1996) and Sæter et al. (1998). The model has the flow stress, recrystallised

grain size and texture as the main outputs, while average misorientation, average subgrain size, strain, temperature, chemistry and distribution of second phase particles are the inputs.

10.4.1 Flow stress

During annealing of a deformed metal softening is a result of recovery and recrystallisation reactions. For a given partially annealed condition the flow stress is given by

$$\mathbf{s}_y = \mathbf{s}_{y,0} + (1 - X_{rex}) \cdot MG_0 b \left[\mathbf{a}_1 \sqrt{\mathbf{r}_i} + \frac{\mathbf{a}_2}{d} \right] \quad (10.37)$$

where $\mathbf{s}_{y,0}$ is the flow stress of the undeformed material, X_{rex} is the fraction recrystallised, G_0 is the shear modulus at room temperature and \mathbf{a}_1 and \mathbf{a}_2 are material constants. Stored energy after deformation and annealing is given by eq. 6.8. For more details see section 6.3.1.

10.4.2 Recovery

The recovery process causes the internal dislocation density to decrease, and the subgrain size to increase. The recovery process was treated in more detail in chapter 2.5.2. In the model, the evolution of the interior dislocation density is given by

$$\frac{d\mathbf{r}_i}{dt} = -2B_r \mathbf{n}_D b \mathbf{r}_i^{2/3} \exp\left(\frac{U_a}{RT}\right) \sinh\left(\sqrt{\mathbf{r}_i} \frac{A_r G b^4}{kT}\right) \quad (10.38)$$

where B_r is a material constant U_a is the activation energy $A_r = \mathbf{w}_r c_{ss}^{-2/3}$ i.e. dependent on the concentration of elements in solid solution.

The evolution of the subgrain size is as follows:

$$\frac{d\mathbf{d}}{dt} = 2B_d \mathbf{n}_D b \exp\left(-\frac{U_a}{RT}\right) \sinh\left(\frac{A_d G b^4}{\mathbf{d} k T}\right) \quad (10.39)$$

where B_δ is a material constant and $A_d = \mathbf{w}_d c_{ss}^{-2/3}$.

On the basis of eq. 10.38 and 10.39, the total dislocation density is calculated:

$$\mathbf{r}_{tot} = \mathbf{r}_i + \frac{kj}{bd} \quad (10.40)$$

From these equations, the subgrain growth and decrease in dislocation density may be calculated.

10.4.3 Recrystallisation kinetics

The recrystallisation kinetics in the model is described by the JMAK-theory, assuming site saturation. This theory was described in chapter 2.5.4.

10.4.4 The density of sites of different categories

Daaland (1993), Daaland and Nes (1996a-b), Vatne (1995), Vatne et al (1996a-d) found that the recrystallisation process is well described by including three different types of nucleation sites: (i) Deformation zones around large second phase particles, (ii) Cube bands and (iii) Grain boundary regions. Such a combination of nuclei was found to result in a recrystallisation texture containing the Cube component and grains of random orientation. The recrystallised grain size is calculated from the total number of sites.

$$D_{rex} = \left(\frac{1}{N_{tot}} \right)^{1/3} \quad (10.41)$$

Deformation zones surrounding hard particles

The calculation of the density of sites nucleated at second-phase particles has been outlined in Section 6.4.4, and the density of the PSN sites is given by eq. 6.17.

Cube sites

Thorough investigations of the nucleation at Cube bands have been carried out by Daaland and Nes (1996a-b), Vatne (1995) and Vatne et al (1996a-d). They demonstrated that the nucleation of Cube grains is associated with Cube grains that were present in the starting material, and which remained orientation stable during deformation. The basis of the nucleation mechanism for Cube grains suggested by Vatne (1995) and Vatne et al (1996a-d) can be summarized as follows: (i) “Old” Cube grains remains metastable during deformation and are deformed to band-like shapes. (ii) Subgrains within the Cube bands have a size advantage compared to the subgrains of other orientations. The typical size distribution of the Cube subgrains was found to have a long tail of large subgrains. (iii) The existence of Cube-S high angle boundary promoted nucleation from Cube bands. The density of Cube sites was found to be (Vatne (1995), Vatne et al (1996a-d)):

$$N_c = \frac{2C_c \bar{d}_c R_c (1 - R_c) R_s S_c^*}{D_0} [\exp(\mathbf{e}) + \exp(-\mathbf{e}) + 1] \quad (10.42)$$

where C_c is a modelling parameter, \bar{d}_c is the average size of the Cube subgrains, R_c is the instantaneous volume fraction of Cube in

the material, R_S is the volume fraction of S in the material, S_C^* is the number of subgrains per unit volume larger than the critical subgrain size, D_0 is the average size of the Cube grains in the starting material and \mathbf{e} is the strain.

Grain boundary regions

Nucleation at pre-existing high angle boundaries has been included basically to account for the large fraction of random oriented grains seen in the recrystallized material even in specimens deformed at low Z -values. In addition nucleation at grain boundary regions is often found to be responsible for a retained deformation texture. In analogy with eq. 10.42 the density of grain boundary sites was found to be (Vatne et al. (1996 a-d)):

$$N_{GB} = \frac{2C_{GB}\bar{\mathbf{d}}(1-R_C)S_{GB}^*}{D_0} [\exp(\mathbf{e}) + \exp(-\mathbf{e}) + 1] \quad (10.43)$$

where C_{GB} is a modeling parameter, $\bar{\mathbf{d}}$ is the average subgrain size and S_{GB}^* is the density of over-critical nuclei in the grain boundary zones.

11 Experimental techniques

11.1 The hot rolling mill

The hot rolling experiments were carried out at the Corus Research Multi Mill in IJmuiden. The mill has a roll diameter of 400mm, and maximum roll force of 1800 kN. The hot rolling was carried out at a roll speed of 1m/s. The initial sample geometry is sketched in fig 11.1. The sample was rolled to a thickness of 30mm giving a net strain of 0.51. Temperatures were recorded with contact pyrometer prior and subsequent to deformation, and the sample were water quenched after reading of final temperature.

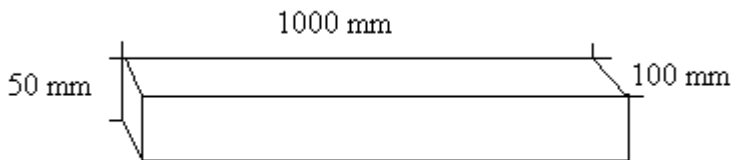


Fig 11.1: Sample geometry of the hot rolling sample

11.2 Hardness measurements

Hardness measurements are an effective way of monitoring softening reactions. A Vickers hardness instrument with load of 1 kg, loading speed of 100 μ m/s and 15 seconds holding time was used. The presented hardness measurements are an average of at least six individual measurements. Samples were polished to a mesh of 1200 prior to hardness measurements.

11.3 Conductivity measurements

Conductivity measurements were performed, using a Sigmatest D2.068. The measurement were done on clean, plane surfaces ground on SiC paper to 1200 Mesh. The presented results are average values of six individual measurements.

11.4 Microstructural characterisation

11.4.1 Sample preparation

The sample preparation for EBSD, and X-ray investigations was carried out as described in chapter 4.5. For characterisation of large particles the samples was prepared by grinding to 2400 mesh on SiC-paper, followed by polishing with 3 μ m and 1 μ m diamond spray and 3-5 minutes treatment with 10% OPS-suspension.

11.4.2 Particle characterisation

Characterisation of large particles was carried out on a conventional SEM in back-scattered mode. The saved pictures were analysed with the KS300 software. A minimum of 1000 particles was measured for each sample. To transpose the recorded “D-distribution into a 3D-distribution, a Johnson-Saltykov method modified to correct for the non zero information depth was applied (Ekström et al. (1998).

11.4.3 Texture measurements - reference frame and notation of orientations

For the hot rolled specimens the texture is represented in the conventional way, that is the polefigures are plotted in the plane (RD,TD).The specimen, is given in Fig. 3.9. Using Miller indexes, the {hkl}-direction is parallel to the normal of the sheet and the <uvw>-direction is parallel to the rolling direction.

Part III: Recrystallisation after single pass hot rolling

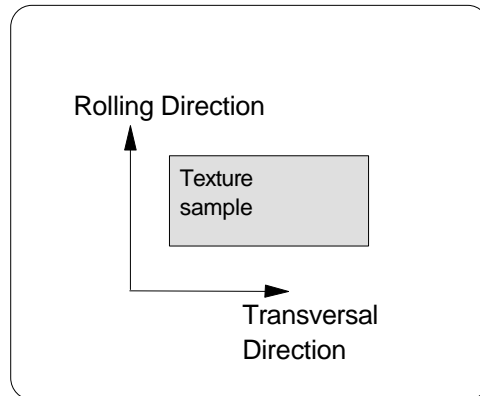


Fig. 11.1: Geometry of the texture sample from PSC specimens, the normal direction comes out of the plane of the paper. (From Pettersen (1999))

Chapter 11: Experimental techniques

12 Experimental Results

12.1 The starting material

The material used was industrially break down rolled and recrystallised AA3103. The samples were machined from the center of the slab, in order to avoid microstructural gradients. The chemical composition of the alloy is given in table 12.1

Table 12.1: Chemical composition of the investigated alloy

Element	Mn	Fe	Si	Mg	Cu	Al
wt.-%	1.0	0.57	0.12	0.015	0.012	Balance

The microstructure of the starting material was investigated in EBSD, while the texture was recorded by X-ray diffraction. The results are presented in fig. 12.1.

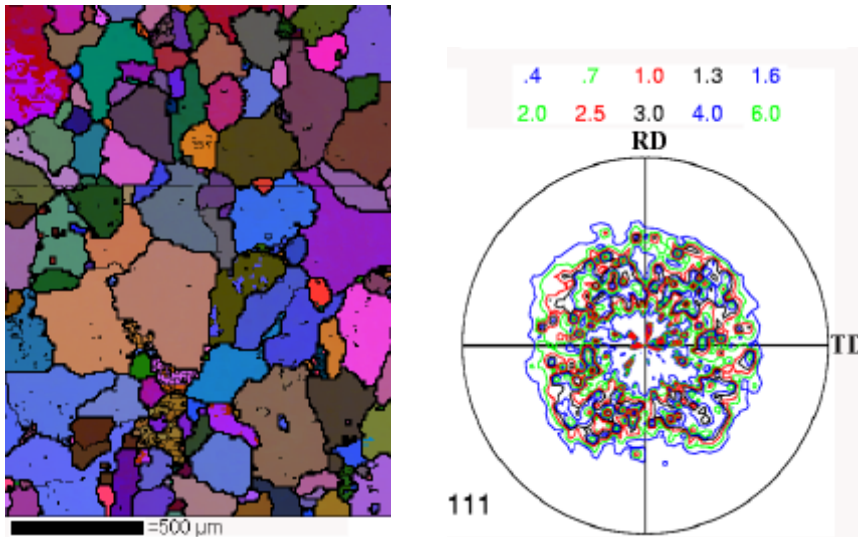


Fig 12.1: Microstructure and texture of the starting material

As seen from the figure, some areas of unrecrystallised material still exist in the microstructure. The average grain size was measured to 112 μm by the line intercept method. The texture is relatively weak

as expected for break-down rolled material. The coarse grained starting material also influences the texture measurements.

12.2 The hot rolling experiment

The most vital parameters for the hot rolling experiment are shown in table 12.2. The temperature after deformation was not measured for the chosen hot rolling pass, in order to be able to quench the sample directly after deformation. But samples deformed to smaller as well as larger reductions showed either a slight decrease or a almost unchanged surface temperature when the surface temperature stabilized after deformation.

Table 12.2: Parameters for the hot rolling experiment

Roll diameter	400 mm
Roll speed	1 m/s
Entry temperature	300°C
Entry thickness	50 mm
Exit thickness	30 mm
True strain	0.51
Average strain rate	8 s ⁻¹

12.3 As deformed microstructure

The microstructure after deformation was investigated using EBSD, and initially the goal was to determine differences in the driving pressure through the thickness of the sample. This goal was approached by measuring the average subgrain size and misorientation at different levels below the surface in the RD/TD-plane. However, no gradient was found, as shown in fig 12.2. As seen in the figure, the subgrain size roughly varies between 2 and 3 μm , while the misorientation is in the range 5-6°. The absence of a gradient in the subgrain size and misorientation may be due to the relatively large grain size combined with the low total strain of the process, namely $\epsilon=0.51$. This will probably lead to inhomogeneous deformation. Each average value in fig. 12.2 is a result from three

different scans, and as shown in fig. 12.3, each scan covers roughly 4-5 grains. To get sufficient resolution, the step size during the EBSD-analysis has to be small, and thus it is hard covering sufficient area.

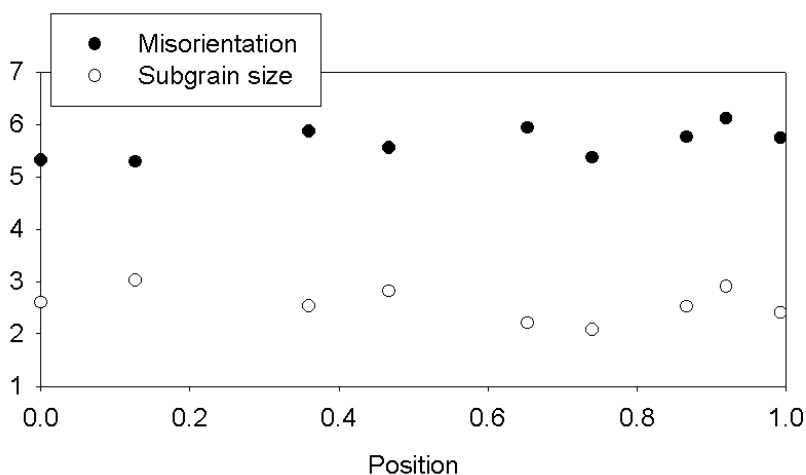


Fig 12.2: Subgrain size and misorientation, measured through thickness by EBSD. (1 = surface, 0 = center)

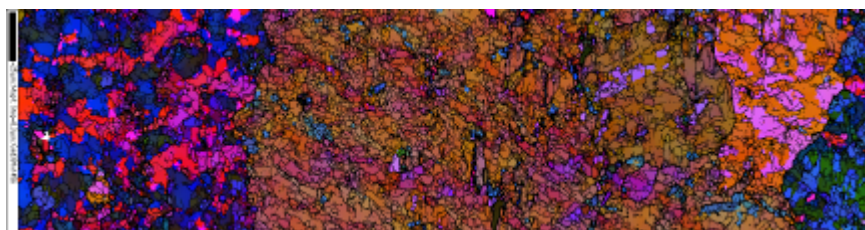


Fig 12.3: Example of as deformed microstructure, 10mm below surface. Black marker pin is 25 μ m.

12.4 Hardness measurements

Hardness measurement is a rapid and easy way to get an estimate of differences in the microstructure. Hardness was measured through thickness in the as deformed sample, and the Vickers hardness number is shown in fig 12.4. It should be pointed out that the scale

on the hardness axis is blown up. Thus, the hardness difference between surface and center is only 6.5% and the fact that the EBSD investigations was not able to show any microstructural gradient is hardly surprising.

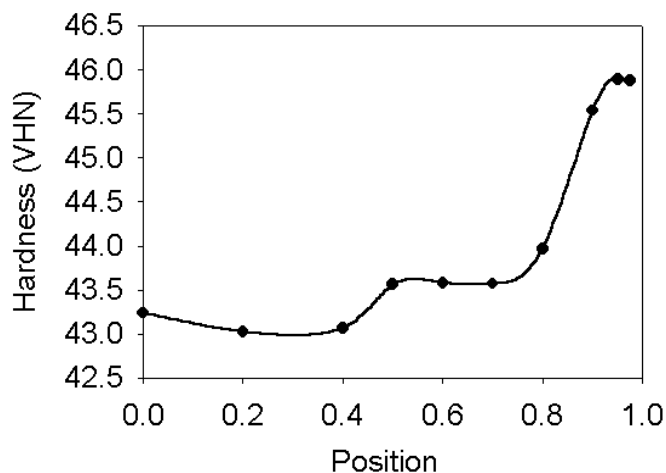


Fig 12.4: Vickers hardness number through thickness. (1 = surface, 0 = center)

12.5 Conductivity measurements

Measurements of conductivity were carried out to get an estimate of the differences in solid solution levels through the thickness of the slab. The results are shown in fig. 12.5. The conductivity is known to depend on the level of elements in solid solution according to Mathiessens rule:

$$\frac{1}{k} = 0.0267 + 0.036Mn + 0.032Fe + 0.0068Si \quad (12.1)$$

As long as the levels of Fe and Si in solid solution is unknown, a correct calculation of the Mn-level is impossible. Still, a maximum level may be calculated, assuming no contribution from Fe and Si. A calculation, based on this assumption is shown in fig. 12.6. The

conductivity measurements show that the levels of Mn in solid solution are largest in the centre of the slab and decreases towards the surface. Close to the surface the decrease is especially rapid.

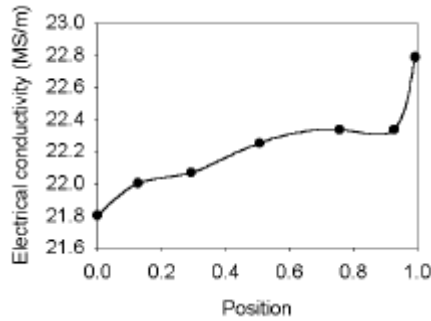


Fig 12.5: Electrical conductivity through thickness. ($1 = \text{surface}$, $0 = \text{center}$)

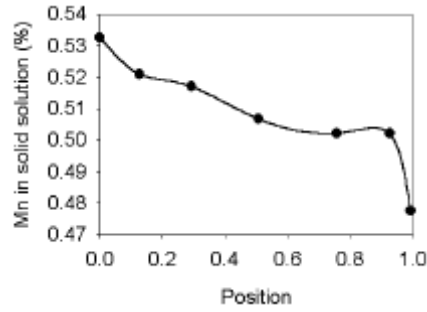


Fig 12.6: Estimated level of manganese in solid solution through thickness ($1 = \text{surface}$, $0 = \text{center}$)

12.6 Distribution of second phase particles

The distribution of large second phase particles is important in terms of nucleation of recrystallisation. Differences through thickness, in the density and size distribution of large particles may affect the recrystallisation properties. Thus, in order to understand the recrystallisation process, knowledge of this parameter is important. In fig. 12.7 the cumulative three-dimensional particle distribution is shown for various positions through thickness. ($S=0$ for centre and $S=1$ for surface). There is a clear gradient in the particle distribution through the thickness of the rolled slab. From the surface towards the center, the number of large particles increases. From approximately $S=0.7$, the particle distribution is more or less constant.

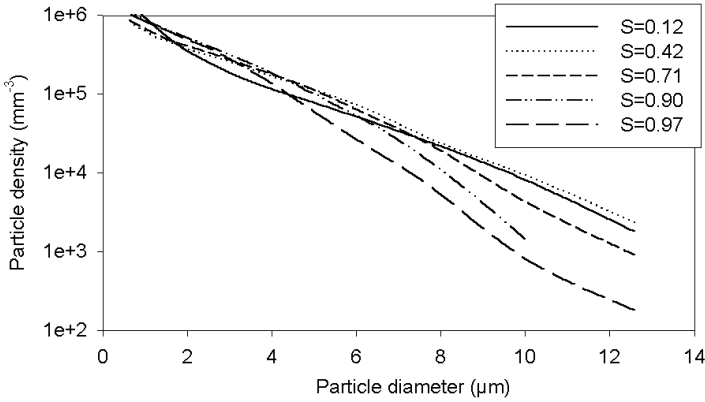


Fig 12.7: Cumulative three-dimensional size distribution of large particles at different positions through thickness ($S=1$ at surface).

12.7 Deformation textures

The deformation textures were recorded for four positions through thickness. The results are shown in fig. 12.9 (a-d).

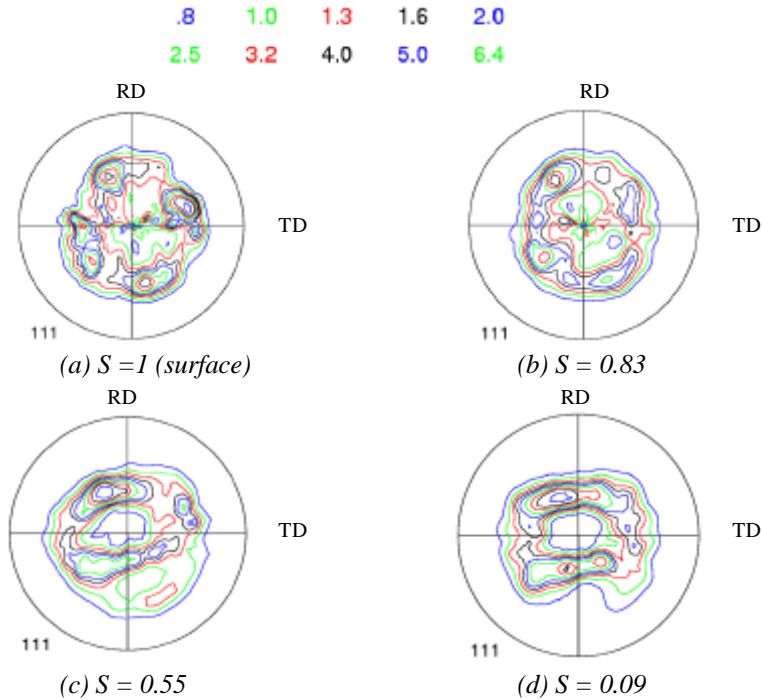


Fig 12.8: Deformation texture for different positions through thickness.

The texture changes gradually from a distorted, relatively weak $\{001\}\langle 110\rangle$ shear texture in the surface, towards a plane strain rolling type texture in the center.

12.8 Recrystallisation kinetics

The recrystallisation kinetics were monitored by annealing samples in salt bath at 350°C. Annealing times from 10 to 10⁶ seconds were used. For each time step the hardness was measured at ten positions through the thickness. This procedure enables construction of the softening curves for each of the ten positions. The softening curves for selected positions through thickness are shown in fig 12.9. The general trend of the figure is faster kinetics towards the surface of the slab. The center of the slab recrystallises slowly, and the recrystallisation process is not complete even after 10⁶ seconds.

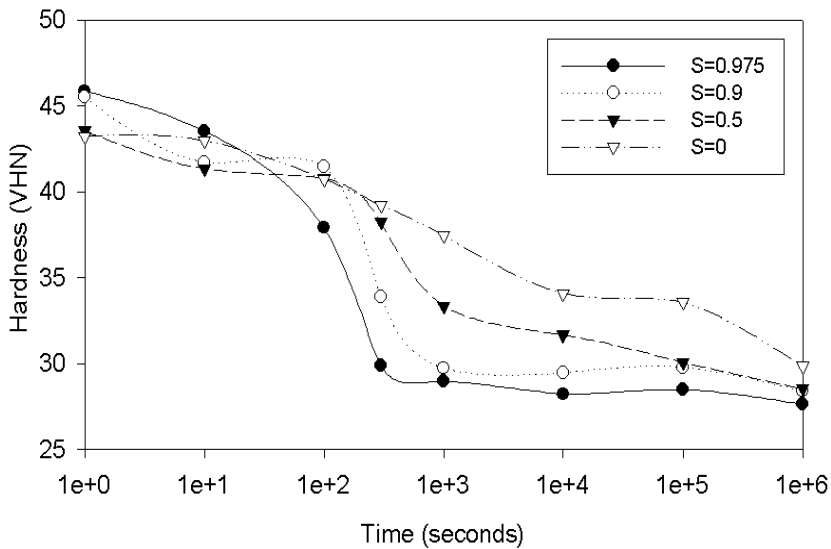


Fig 12.9: Softening curves for various positions through thickness

A better overview of the recrystallisation kinetics as function of position through thickness may be obtained if the time to 50% softening is determined for each position. The result is presented in

fig. 12.10. There is an obvious gradient in the recrystallisation kinetics through the thickness of the slab. A gradual increase up to $S=0.7$ is followed by a plateau extending to $S=0.2$. In the center of the slab, the recrystallisation kinetics are even slower, possibly a sign of precipitation during annealing.

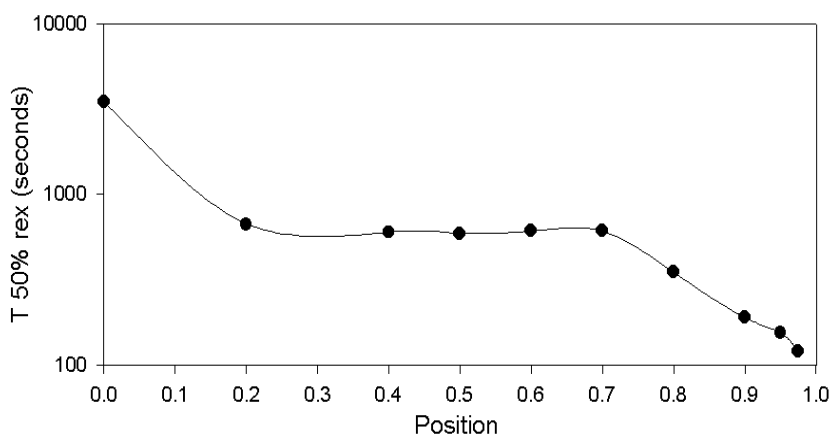


Fig 12.10: Time to 50% recrystallisation for different positions through thickness.

12.9 Recrystallised grain sizes

The recrystallised grain size was measured at different positions through thickness from EBSD-scans. The line intercept method was used for the measurements. In fig. 12.11 the results are shown. Except for the larger recrystallised grain size at $S=0.87$, there are only small differences in the recrystallised grain size. This behavior differs from the recrystallisation kinetics, where a clear gradient was found.

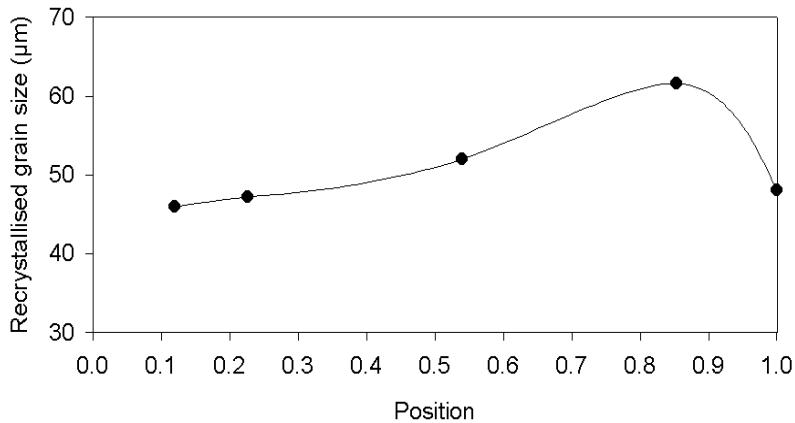


Fig 12.11: Recrystallised grain size as function of position. (0=centre, 1=surface)

Higginson et al. (2003) observed similar characteristics during recrystallisation of an Al-Mn alloy: The recrystallisation kinetics were increasingly more rapidly towards the surface, with a local maximum at 20% below the surface, relative to the half thickness. Interestingly, the position of this local maximum in recrystallisation kinetics corresponded to the position of the maximum recrystallised grain size. Similar gradients in recrystallised grain size have also been observed in extruded profiles. Ryen (2004) observed a very course grained layer between center and surface of the profile, while the center and the surface were more fine grained.

13 Modelling results

13.1 FEM-simulations and prediction of microstructure

13.1.1 The modeling procedure, outline and definitions

The FEM-modeling of the rolling pass, and the subsequent prediction of the microstructure is done in two individual steps: First the FEM-simulation is used to calculate the displacements of the nodes as function of time, as well as the temperature evolution in the slab. Secondly, node paths are extracted from the FEM-results and run through the *ALFLOW* model in order to predict the final microstructure.

The coordinate system for the further presentation of the results is described in fig. 13.1. Origo is placed in the center of the rolls, and the most important points are shown in the figure.

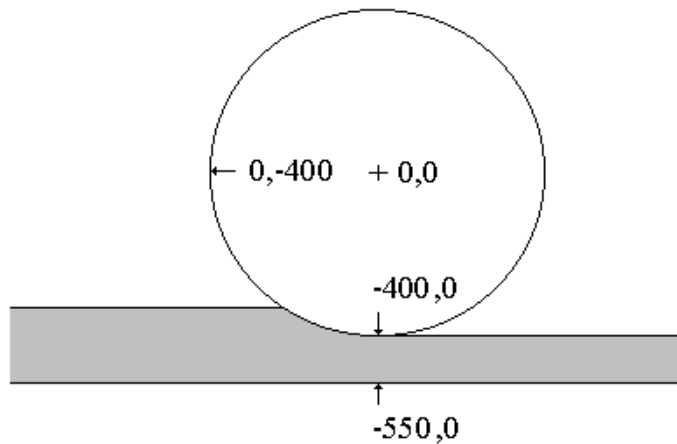


Fig 13.1: Coordinate system for FEM-simulations and prediction of microstructure after deformation.

13.1.2 Mechanical properties

The FEM-results give a good description of the mechanical aspects of the hot rolling process. In particular, it clarifies the difference in deformation history as a function of the position through thickness of the rolling slab. In fig. 13.2 the development of strain during the rolling pass, as function of through thickness position is given.

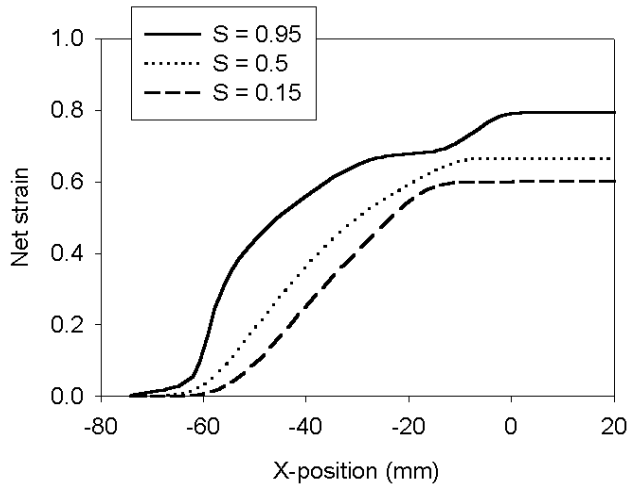


Fig 13.2: Net strain as function of X-position ($X=0$ at the outlet) for various positions through thickness. ($S=0$ at surface)

The development of strain as function of x-position clearly depends on the through thickness position. While the strain increases more or less linearly in the center, the strain development in the surface regions is more complex. In the center of the slab, there is no further increase in strain for the last 15-20 mm. of the rolling gap. The differences are even clearer if the strain rate is investigated, as shown in fig. 13.3.

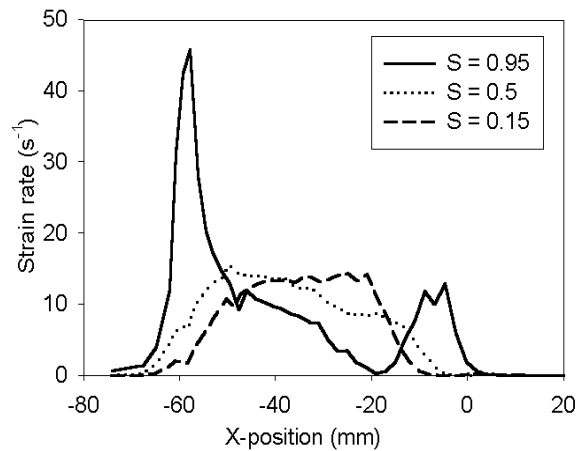


Fig 13.3: Strain rate as function of x -position ($X=0$ at the outlet) for positions through the thickness.

The plot of the strain rate for various positions through the thickness shows the major difference in deformation history between the surface and the center. The surface regions experience very large strain rates in the beginning of the rolling pass, due to shearing against the rolls. However, neither the data for strain rate nor for strain give the direction of the applied strain. The strain in hot rolling is a mix of plane strain compression and shear. The plane strain component works in the same direction through the whole process, but the shear component is not that straightforward. This is visualized in fig. 13.4 where the relative velocity between the rolls and the material is plotted for nodes close to the surface. The large initial strain rate observed in fig. 13.3 for the surface node, is no surprise when the large relative velocity between rolls and slab is considered. The position of the neutral point is also given by fig. 13.4. It should be noted that the final shear stress, applied after the neutral point, is in the opposite direction. It is therefore representing a strain reversal. The temperature development in the slab during the rolling operation could also be obtained from the FEM-data, and is shown in fig 13.5.

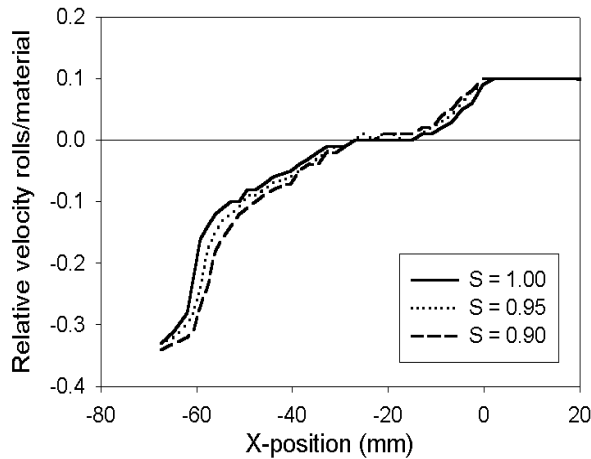


Fig 13.4: Relative velocity between rolls and slab through the rolling gap, for positions near the surface. Horizontal line marks the neutral point, and X=0 at the outlet.

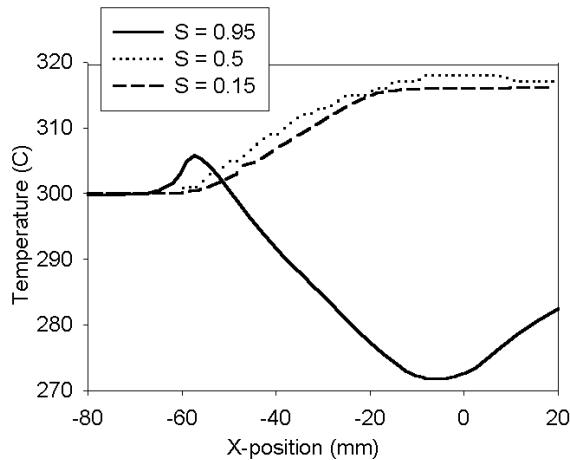


Fig 13.5: Temperature development through the rolling gap for different positions through thickness.

There is a large difference in the temperature development through thickness of the slab. Close to the surface the rolls are cooling the slab, and thus the temperature decreases for the nodes closest to the

surface. When the surface is no longer in contact with the rolls, the temperature increases as heat is transferred from the center of the slab. Closer to the center of the slab, the temperature increases through the rolling gap due to the energy from the deformation. As both the strain rate and the temperature are known from the FEM-simulations, the Zener-Hollomon parameter may be calculated. The development of Z through the rolling gap is given in fig 13.6.

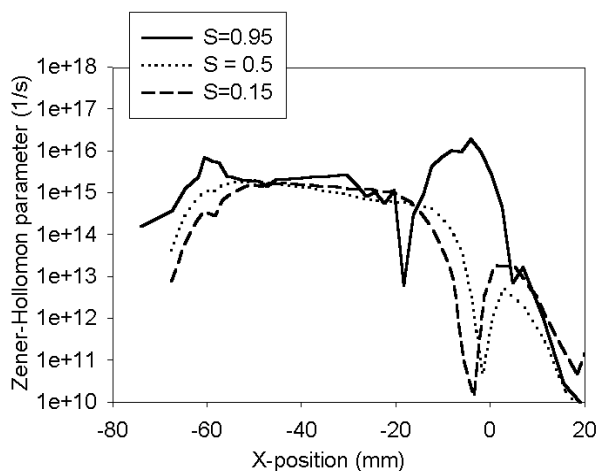


Fig 13.6: Development of the Zener-Hollomon parameter through the rolling gap for different positions through thickness.

The value of the Zener-Hollomon parameter goes through several changes during the rolling pass. The value is generally largest for the surface node, except for a small range in the vicinity of the neutral point. Especially near the outlet of the rolling gap, the value of Z is much larger near the surface than in the center of the slab, due to the combination of increased strain rate and lower temperature.

13.1.3 Microstructure evolution through the rolling pass

In the following, an example of the development of microstructure through a hot rolling pass will be presented. The friction factor (m)

is set to 0.8 while the heat transfer coefficient (d) is set to 50. The microstructure development is then followed for nodes ending up at relative thickness of 0.9, 0.5 and 0.15. The results are shown in fig 13.7-13.9. Generally, the internal dislocation density is more sensitive to changes in the deformation through the rolling gap than the subgrain size and the subgrain misorientation.

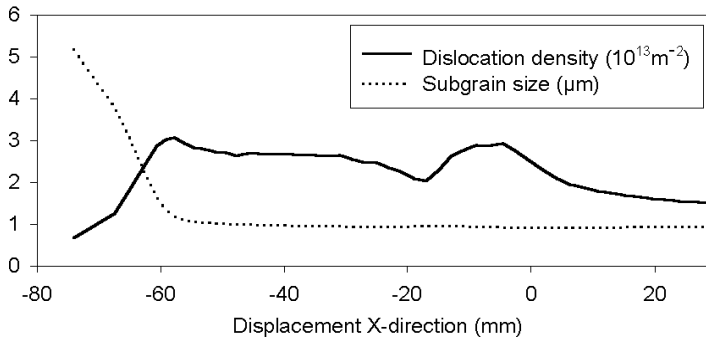


Fig 13.7: Development of microstructure through the hot rolling pass for a node ending up 1.5mm below the surface. ($S = 0.9$)

The node, followed in fig. 13.7 ends up 1.5mm below the surface, and is thus affected by surface shear. This is visible, looking at the dislocation density. The dislocation density drops at the neutral point, followed by an increase, before the density drops towards the outlet of the rolling gap. The intermediate drop in the dislocation density corresponds to the position of the neutral point, and is thus an effect of the reduced strain rate in this region. The subgrain size rapidly reaches saturation, and is not affected by the changes in strain rate through the rolling gap.

Part III: Strain path effects in hot rolling.

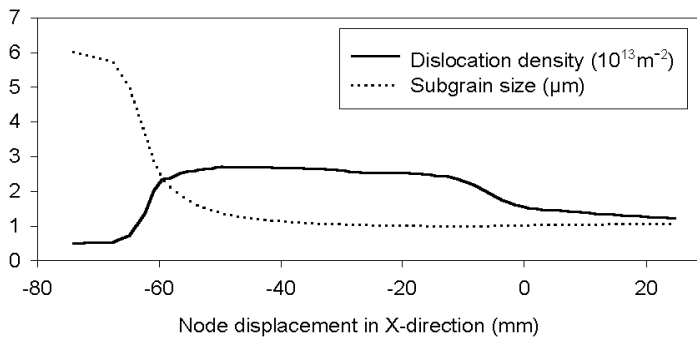


Fig 13.8: Development of microstructure through the hot rolling pass for a node ending up 7.5mm below the surface. ($S=0.5$)

The main difference, moving to the node ending up 50% into the half thickness, is that the effect from surface shear on the dislocation density is gone. However, the dislocation density drops towards the outlet of the rolling gap as a result of the lowered strain rate. The subgrain size also saturates slower, and at a slightly smaller size, compared to the surface node.

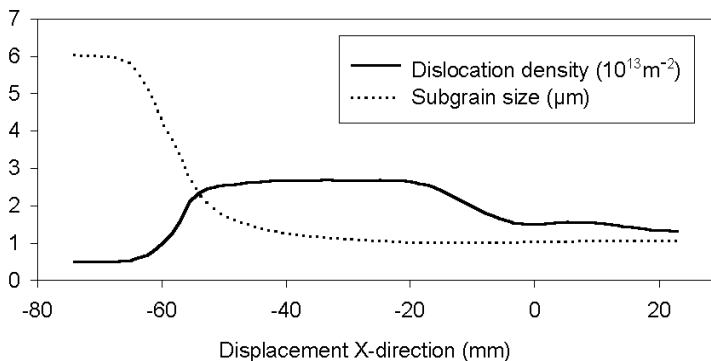


Fig 13.9: Development of microstructure through the hot rolling pass for a node ending up 12.8 mm below the surface. ($S=0.15$)

Moving even closer to the center does not affect the development of microstructure much. As shown in fig. 13.9 the subgrain size changes little after saturation, and the dislocation density drops

towards the outlet of the rolling gap. As seen from the figures, the average subgrain misorientation is not included in the modeling. The inability of the model to produce realistic subgrain misorientation data is of course a weakness. Especially when it comes to modeling recrystallisation, there is a need for good subgrain misorientation data.

13.1.4 Parameter sensitivity

As the modeled deformation microstructure is the basis for modeling the recrystallisation process, knowledge of the parameter sensitivity of the simulations and modeling is important. In fig. 13.10-13.15 the effect of changes in friction parameter and heat transfer parameter on dislocation density, subgrain size and calculated flow stress is shown.

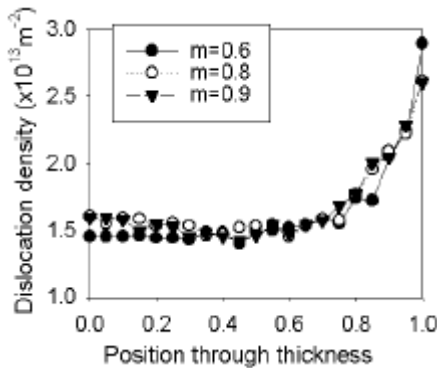


Fig 13.10: Effect of friction parameter on dislocation density inside subgrains, for $d=50$.

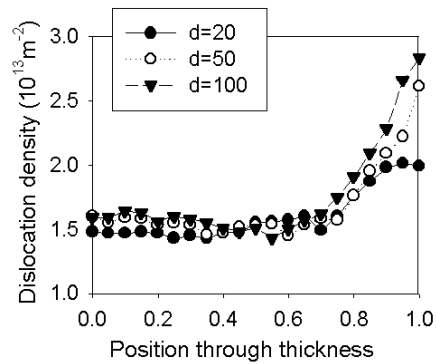


Fig 13.11: Effect of heat transfer coefficient on dislocation density inside subgrains, for $m=0.8$.

The dislocation density through thickness of the slab is not much affected by changes in the friction parameter. The effect of changes in the heat transfer coefficient is however much larger. Higher heat transfer coefficient results in higher dislocation density, as the cooling from the rolls is increased, resulting in a higher Zener-Hollomon parameter.

Part III: Strain path effects in hot rolling.

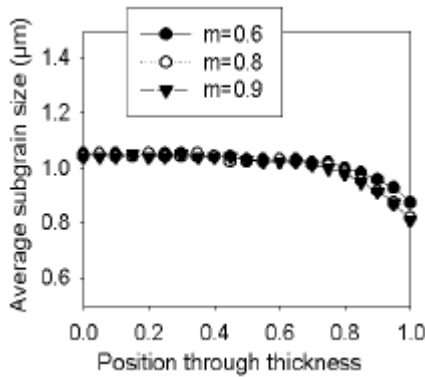


Fig 13.12: Effect of friction parameter on subgrain size, for $d=50$.

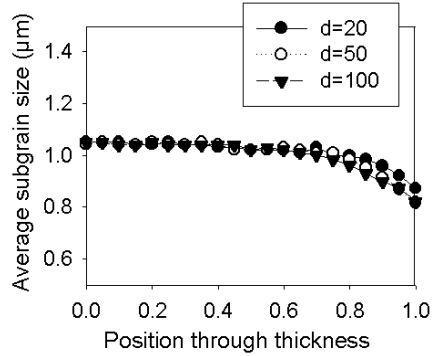


Fig 13.13: Effect of heat transfer coefficient on subgrain size, for $m=0.8$.

The effect on the subgrain size from changes in friction parameter or heat transfer coefficient is much smaller. Large friction parameter and large heat transfer coefficient result in the smallest subgrain size. In opposition to the effect on the dislocation density, the changes in subgrain size as a result of changes in heat transfer coefficient and friction parameter, are both of the same magnitude. Combining the microstructure parameters, the flow stress is calculated, as shown in fig 13.14 and 13.15.

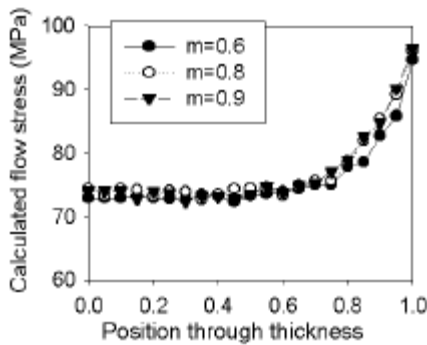


Fig 13.14: Effect of friction parameter on calculated flow stress, for $d=50$.

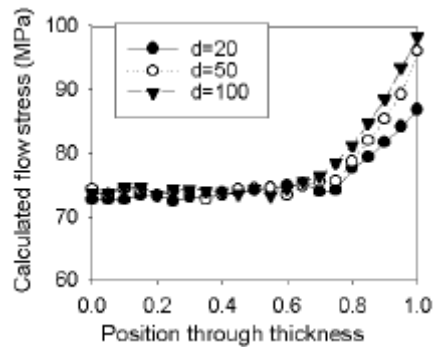


Fig 13.15: Effect of heat transfer coefficient on calculated flow stress, for $m=0.8$.

The friction factor has very little influence on the flow stress, while the effect of change in heat transfer coefficient is somewhat larger. For comparison to the experimental data, it is possible to convert the Vickers Hardness measurements from fig 12.4 to flow stress. Eq. 13.1 has proven to give a good fit, given the right value of the constant C.

$$s_{0.2} = C \cdot VHN - 10 \cdot C \quad (13.1)$$

The constant is normally found to have a value between 2.5 and 4 (Sæter (1997)). In fig. 13.16 the calculated flow stress for three different values of C is shown.

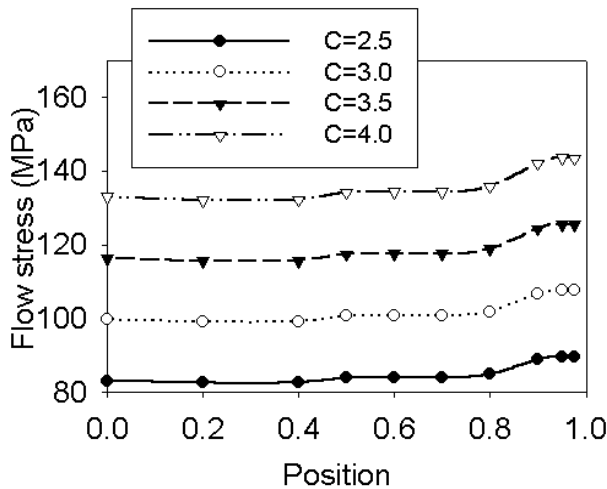


Fig 13.16: Flow stresses calculated from hardness measurements for different values of C.

In the current study, the most important aspect is the variation in the microstructure through the sample thickness. It is therefore worth noting that the constant of eq. 13.1 does not change the gradient in the calculated flow stress. The calculations suggest that the gradient in the hardness corresponds to a difference in flow stress of 7-8 MPa. The simulations, on the other hand, predict a variation in flow

stress differences of up to 25MPa, four times the experimentally measured gradient. However as shown in the experimental results, the simulations predict that the microstructure changes little from the center to $S=0.8$, and then changes towards the surface.

13.1.5 Texture evolution

The texture evolution was modeled for the surface and center node, using a FC-Taylor model. The results are shown in fig 13.17. The plane strain texture in the center was well captured by the model, while the surface texture was not as well predicted. This may be due to the more complex strain path in the surface zones.

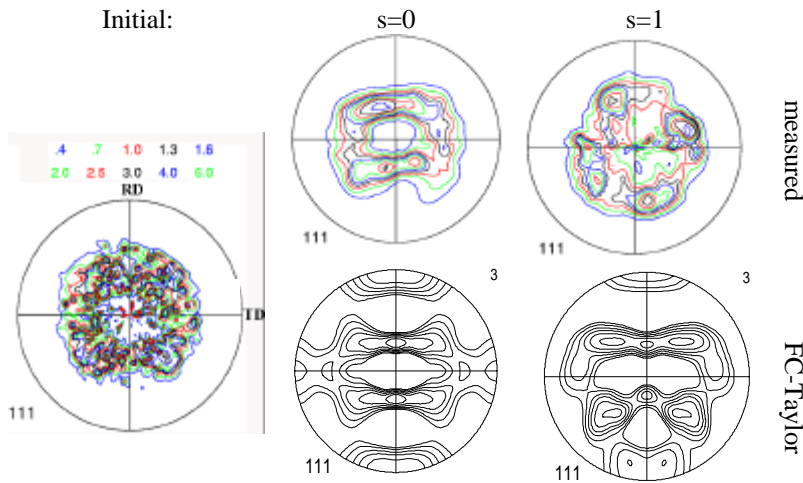


Fig 13.17: Measured and modeled texture evolution. Directions as shown in pole figure of initial condition.

13.2 Modeling recrystallisation - ALSOFT

As an aid for the discussion of the experimental recrystallisation results, an attempt was made to model the recrystallisation kinetics. *ALSOFT* was used for this purpose.

13.2.1 Input values

The input parameters of *ALSOFT* are subgrain size, subgrain misorientation, dislocation density inside subgrains, particle distribution parameters, level of elements in solid solution and annealing temperature. The values for subgrain size and dislocation density inside subgrains are taken from the simulations in *ALFLOW*, even though this means that the gradient from center to surface is probably too large. The misorientation is set to 3.5° . Values for particle distribution and manganese in solid solution are taken from the experimental data. The particle distribution is fitted to equation 13.2 for each position through thickness. The set of input values is shown in table 13.1.

$$f(\mathbf{h})=A \exp(-B\mathbf{h}) \quad (13.2)$$

Table 13.1: Input values for modeling of recrystallisation

	S	δ (μm)	ρ_i (m^{-2})	ϵ	Mn (ss) wt-%	A	B
Input values	0.95	0.87	$2.2 \cdot 10^{13}$	0.803	0.493	$2 \cdot 10^6$	0.74
	0.9	0.91	$2.1 \cdot 10^{13}$	0.794	0.502	$1 \cdot 10^6$	0.55
	0.7	1.01	$1.6 \cdot 10^{13}$	0.728	0.502	$2 \cdot 10^6$	0.66
	0.2	1.05	$1.5 \cdot 10^{13}$	0.608	0.519	$1 \cdot 10^6$	0.51

The model was tuned against flow stress data for the surface node, derived from the hardness measurements.

13.2.2 Modeling results

In fig 13.17 the modeled softening curves are shown. The curve with the largest starting flow stress is the surface node, and the curve with the lowest starting flow stress corresponds to the

Part III: Strain path effects in hot rolling.

position $S=0.2$. The effect on recrystallisation kinetics of the microstructural differences through thickness is very small. The model is neither able to predict the difference in the shape of the softening curves nor the difference in time to 50% softening through thickness, just on the basis of difference in stored energy.

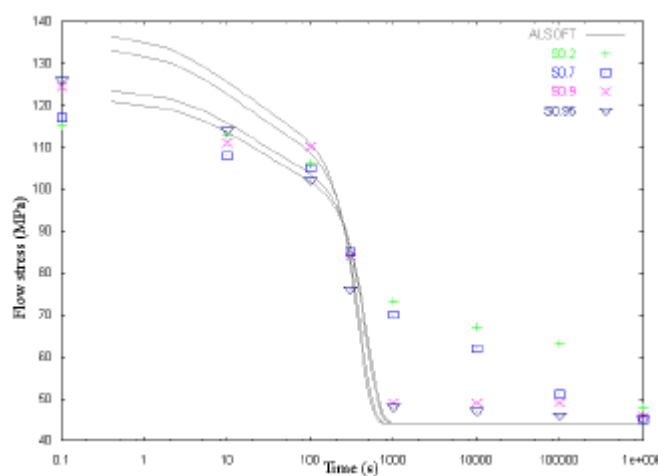


Fig 13.18: Results from recrystallisation modeling in ALSOFT

14 Discussion

14.1 As deformed microstructure

ALFLOW predicts a larger gradient in flow stress from center to surface than what is derived from the hardness measurements. The deformation history in the hot rolling process is quite complicated, especially in the surface areas. Strain rate, temperature and thus also the Zener-Hollomon parameter change considerably through the rolling pass as shown in fig. 13.2, 13.3 and 13.5. This of course makes FEM-simulations of the hot rolling process difficult, and some of the observed difference between modeling and experimental results are probably due to mispredictions in the FEM-simulations.

The rapid changes in Zener-Hollomon parameter of course also complicate the modeling of subgrain sizes and dislocation densities. The development of subgrain size and dislocation density through the rolling pass was shown in fig. 13.7-13.9 for three positions through thickness. The dislocation densities show relatively rapid response to change in deformation conditions, while the subgrain size is not much affected. However, experimental observations suggest that the subgrain size could be somewhat more sensitive to changing deformation parameters: Baxter et al. (1999) investigated the microstructural effect of transients in strain rate during deformation of Al-1%Mg in plane strain compression. They found that the subgrain size rapidly responded to change in strain rate

In addition to the large changes in deformation conditions, the surface areas also undergo a change in strain path because of the surface strain reversals. Effect of strain path is not included in *ALFLOW*. Accordingly, strain path effects may explain some of the difference in microstructure gradient through thickness between

model and experimental results, especially since the change of strain path should cause a smaller gradient towards the surface. However, strain path changes are not commonly seen to affect subgrain size (Zhu and Sellars (1996) Higginson and Sellars (2003)). Accordingly, attributing the whole difference in flow stress to strain path effects is probably an overestimation.

14.2 Recrystallisation

To understand the recrystallisation process after hot rolling, especially in terms of potential strain path effects, has been the major goal of this study. The modeling approach using *ALSOFT* has shown that vital aspects of the origin of the through thickness recrystallisation gradient after hot rolling are probably missing in today's handling of the phenomena. In *ALSOFT* the recrystallisation properties, both in terms of nucleation and growth, is mostly governed by the driving pressure. The driving pressure, and its change through the thickness of the slab, is closely related to the microstructural properties discussed in the previous chapter. If the gradient in driving pressure is calculated from the hardness profile, the difference in driving pressure between surface and center turns out to be relatively small. The *ALSOFT* model is not able to predict the through thickness gradient in t_{50} neither on the basis of this input nor the somewhat steeper gradient in microstructural parameters obtained from the *ALFLOW* model.

14.2.1 A simplified modeling approach

As *ALSOFT* is not able to predict the observed recrystallisation kinetics, a simplified model is employed in order to obtain an estimate of the subgrain size on the subsequent recrystallisation process. The model is similar to the one used to explain recrystallised grain sizes after hot torsion in chapter 6.4. In this

case it is used to estimate the time to 50% recrystallisation. A similar model was also used by Furu et al.(1999) for the case of plane strain compression. The model assumes that the nucleation density is controlled primarily by the grain boundary area. The development of grain boundary area pr. volume with strain is given by

$$A(\mathbf{e}) = \frac{2}{D_0} (\exp(\mathbf{e}) + \exp(-\mathbf{e}) + 1) \quad (14.1)$$

Where D_0 is the initial grain size. The strain for each position through thickness is obtained from the FEM-simulations. Similar to the equation developed for grain boundary nucleation after torsion, the density of nuclei may be calculated.

$$N = \bar{\mathbf{d}} \cdot A(\mathbf{e}) \cdot S_{GB}^* \quad (14.2)$$

Where $\bar{\mathbf{d}}$ is the average subgrain size and S_{GB}^* is the density of subgrains larger than the critical size, calculated from eq. 6.14. The driving pressure is calculated from eq. 6.8, and the time to 50% recrystallisation may then be estimated as

$$t_{50} = \frac{C_t}{M_{GB} P_D} \left(\frac{1}{N} \right)^{1/3} \quad (14.3)$$

Where C_t is a constant, M_{GB} is the grain boundary mobility, which is assumed to be constant, and P_D is the driving pressure. Thus, the recrystallisation kinetics in this model are mainly a function of driving pressure, with a contribution from the increasing grain boundary area close to the surface. This is of course an oversimplification of the process, both in terms of involved parameters, and the fact that only one position on the softening

curve is predicted. But as a tool to understand the effect of some of the involved parameters it is helpful and easily handled. The equation for t_{50} is tuned to the experimentally observed recrystallisation time for $S=0.2$. Three different gradients in subgrain size from center to surface are used in order to see the effect on the recrystallisation kinetics. The first approach is to use the gradient in subgrain size derived from the through thickness hardness measurements.

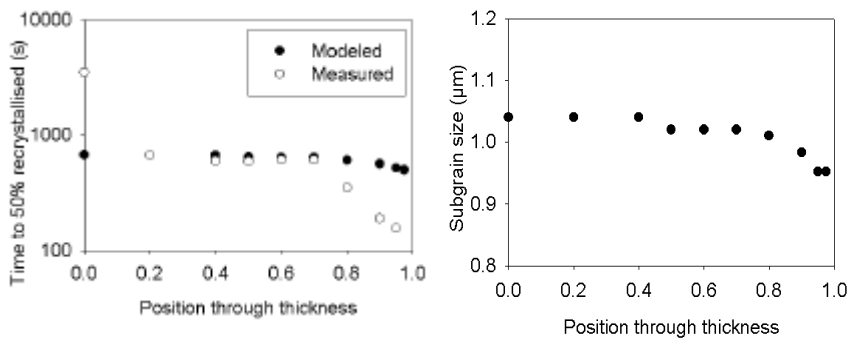


Fig 14.1: Modeling of time to 50% recrystallisation, and the subgrain size profile used. The subgrain sizes are derived from hardness measurements.

Using the experimentally obtained microstructural gradient, it was not possible to fit the change in recrystallisation kinetics through thickness. The next attempt is then to use the gradient obtained from the modeling of the deformed microstructure.

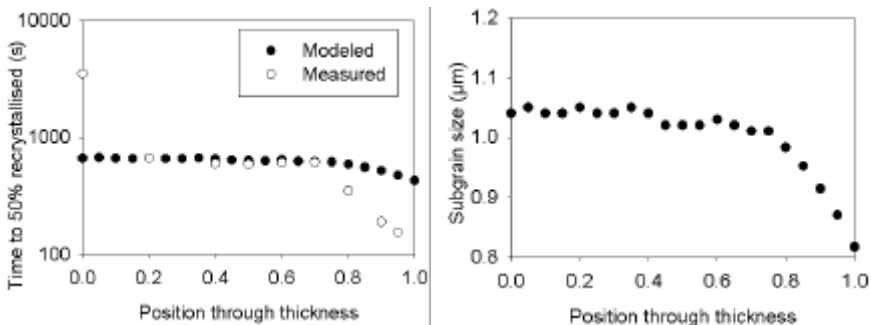


Fig 14.2: Modeling of time to 50% recrystallisation, and the subgrain size profile used. The subgrain profile is based on modeling results.

Still, the predicted gradient in t_{50} is not even close to the experimentally observed. In order to investigate the size of microstructural gradient that is required to produce the observed gradient in t_{50} , the subgrain size was roughly tuned to obtain fit between experimental and modeled results. The result for t_{50} and the associated subgrain size is shown in fig. 14.3.

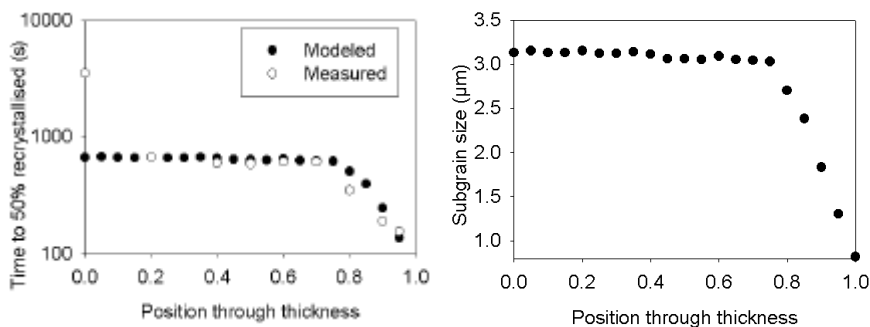


Fig 14.3: Modeling of time to 50% recrystallisation. Subgrain size tuned to match recrystallisation data.

It turns out that if the subgrain size at the surface was kept constant, the subgrain size in the center had to be increased to over $3\mu\text{m}$ in order to explain the observed difference in recrystallisation kinetics. The relative difference in subgrain size between center and surface is then almost four times larger than the modeled and almost 10 times larger than derived from the hardness data. On the basis of these results it is likely that the gradient in recrystallisation kinetics through thickness is due to other effects than just a difference in driving pressure.

14.2.2 Nucleation

As the gradient in driving pressure could not explain the magnitude of the gradient in recrystallisation kinetics, it is natural to look at the nucleation mechanisms.

Particle stimulated nucleation

It was shown in fig. 12.7 that the particle distribution differs through thickness after the rolling pass. Which effect this has on the recrystallisation process depends on the local deformation conditions. Humphreys and Hatherly (1996) calculated the minimum particle size for successful nucleation by PSN as function of Zener-Hollomon parameter. The result is shown in fig. 14.4.

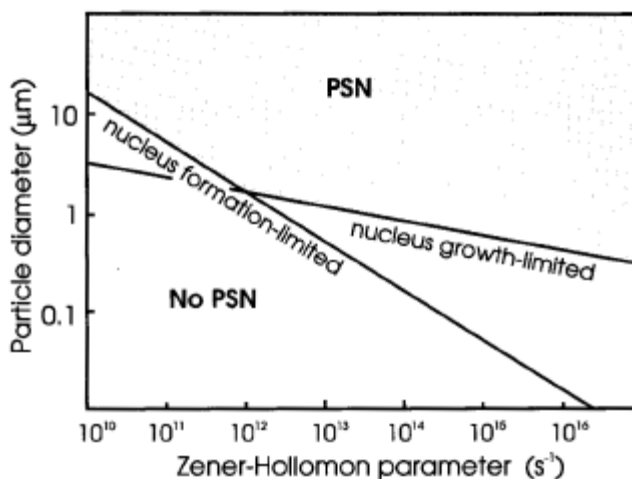


Fig 14.4: The effect of deformation conditions on PSN (Humphreys and Hatherly (1996))

The Zener-Hollomon parameter is calculated From the FEM-simulations. It was found to be larger than 10¹³/s during most of the rolling operation. If this is compared to the calculations presented in fig. 14.4 it is seen that particles down to almost 1µm may serve as nucleation points. This means that for the present study, the break up of particles close to the surface may be of little relevance to the efficiency of PSN as nucleation mechanism through thickness, as the difference in cumulative particle density is small in this range. It should also be noted that for Zener-Hollomon parameters larger that 10¹² s⁻¹ nucleation at particles is limited by nucleus growth. This means that the density of PSN-nuclei is actually directly related to

the driving pressure (eq. 2.15). Still there is one additional effect to consider which is not included in modeling. In addition to the combined requirements for Zener-Hollomon parameter and particle size illustrated in fig. 14.4, a certain amount of strain is needed in order to form the deformation zone. The formation of the deformation zone may however be affected by strain path as well. In chapter 6.2 a mechanism for weakening of deformation zones surrounding particles during strain reversals was proposed. This may reduce the number of nucleation sites due to PSN. At the present state of knowledge it is however hard to estimate the magnitude of such an effect. Also, the interaction between different strain modes may influence the PSN activity. Parts of the slab experiences a combination of plane strain compression and shear. It is not known what effect this has on the development of the deformation zone.

Grain boundary area

The grain boundary area is an important parameter in terms of nucleation. In the center of the slab, the grain boundary area is relatively easily predicted as the deformation mode is almost pure plane strain compression. Closer to the surface the deformation mode is a combination of plane strain compression and shear, and the reversal of the surface strain complicates the picture as well. However, the difference in total strain between center and surface is relatively small, and the error by calculating the grain boundary area in terms of total strain is probably relatively small.

Effects of inhomogenous microstructure

During modeling the microstructure is described in terms of average values for parameters like subgrain size- and misorientation, as well as for the distribution of nucleation sites. However, the EBSD-measurements of the as deformed microstructure show that the microstructure is not homogenous. Grains of differed orientations

clearly have differences in subgrain size. The large initial grain size and relatively small reduction also contributes to a microstructure that is not homogenous. Glez and Driver (2003) studied aluminium single crystals of different orientations, deformed in plane strain compression. They found that subgrain size as well as misorientation depended on orientation. This means that some grains will be better suited as nucleation sites than others, and some are more likely to be consumed.

14.2.3 Summing up

In the current interpretation of recrystallisation and in the current recrystallisation models, the driving pressure is an essential parameter. The driving pressure also to a large extent governs the calculation of nucleation sites, especially for small deformations where the change in grain boundary area is small. In order to understand recrystallisation behavior after complex strain paths, in inhomogeneous materials and under changing deformation conditions a better understanding of the effect on the nucleation process is needed. More comments on the mechanisms possibly influencing the density of nuclei originating from different mechanisms, and a broader discussion of strain path effects on recrystallisation based on comparison of results from the current work with literature data is found in chapter 16.

14.2.4 Concurrent precipitation

The experimentally determined recrystallisation kinetics show a large increase in the time to 50% recrystallised for the position in the center of the sample. The large increase in recrystallisation time from $S=0.2$ to $S=0$ is hard to explain in terms of effects related to nucleation or driving pressure. However, the gradient in the amount of manganese in solid solution may explain this behavior. Sjølstad

(2003) studied precipitation effects on annealing of aluminium. For annealing at 350°C after a strain of $\epsilon=0.5$ the critical amount of Mn in solid solution for concurrent precipitation to occur was found to be approximately 0.47%. In this study, the level of Mn in solid solution after deformation was calculated to 0.48% at the surface, increasing to 0.53% in the center of the sample. These values were calculated without correcting for other alloying elements, so the actual level of manganese is probably somewhat smaller. Therefore it is not unlikely that a precipitation effect may be seen in the center of the sample, explaining the large increase in recrystallisation time.

Part III: Strain path effects in hot rolling

15 Conclusions

One-pass hot rolling of an aluminium slab, and subsequent recrystallisation have been studied experimentally and by a combination of simulations and modeling. The following conclusions have been reached:

1. The combination of FEM-simulations of the rolling gap and use of the model ALFLOW to obtain the gradient in microstructural parameters through thickness resulted in a larger gradient than indirectly obtained from hardness measurements.
2. The texture developed in the center of the sample was successfully simulated using a FC-Taylor code. The prediction of the texture development in the surface was less accurate.
3. A gradient in the time to 50% recrystallisation through the thickness of the hot rolled slab was seen experimentally. The recrystallisation was fastest in the surface regions, and slowest in the center.
4. The Mn-content after deformation increased from surface to center.
5. The center of the sample recrystallised much slower than any other point. This was seen as a probable effect of concurrent precipitation.

Part III: Strain path effects in hot rolling

6. Modeling of the recrystallisation kinetics, using the gradient in microstructural data as input, did not show the experimentally observed gradient in kinetics.
7. This mismatch between experimental data and the model was explained as an effect of the models limited coverage of effects on nucleation density, due to other effects than change in driving pressure.

Part IV: Summing up

16 Summing up

It is a proven fact that recrystallisation is affected by the strain path during deformation. In laboratory trials, this has been shown by Lindh et al. (1993), Zhu and Sellars (1996), Vatne et al. (1996) as well as in the present study. Hot rolling experiments, comparing recrystallisation after different rolling schedules, differing only in terms of strain path, have shown that strain path dependence of recrystallisation is also a phenomena of industrial relevance. (Higginson and Sellars (2001), Black et al. (2001), Higginson et al. (2003)). Still, the understanding of the phenomena is very limited, and opinions differ regarding the causes of the strain path effects on recrystallisation. In this chapter, the experimental results obtained in torsion and hot rolling during the current study are compared to data from the literature. The aim is to sort out which strain path related effects are important for the recrystallisation process, based on the existing experimental studies of the subject.

16.1 Stored energy

In previous studies of strain path effects on recrystallisation, much effort has been put into studies of the stored energy in the material after deformation, and thus the driving pressure for recrystallisation.

16.1.1 The concept of strain efficiency

Lindh et al. (1993) studied recrystallisation in copper after deformation in tension/compression. Samples deformed in tension/compression showed higher recrystallisation temperatures than those deformed in simple compression to the same net strain. It was concluded that reversed deformation was less efficient in terms of energy storage in the specimens, and an efficiency factor of 0.65 was calculated for the reversed strain, using the least squares

method. This approach seemingly explained the results. But such a method must be used with caution, and can't explain other experimental observations: The flow stress response on strain reversals is highly dependent on the alloy, as shown by Stout and Rollett (1990), and is probably due to several different microstructural effects. This makes it highly unlikely that a universal efficiency factor may be established. In the present study the recrystallised grain size in AA3103 after hot torsion is smaller after a deformation of $\epsilon=1.8$ than after a deformation of $\epsilon=1.8-1.8$. If this result is to be explained in terms of strain efficiency, a negative efficiency factor is required. Similar behavior was seen by Higginson et al. (2003) in two pass hot rolling with different roll pass schedules. The rolling reduction was 50% in the first pass and 20% in the second. The rolling direction of one of the samples was reversed before the second pass (FR) while the other sample was rolled the same direction in both passes (FF). One sample was recrystallised after the first pass as a reference. It was found that the sample subjected to FF rolling recrystallised faster than the single pass sample, while the FR rolled sample showed slower recrystallisation kinetics than the single pass sample. Once again, this is hard to explain in terms of strain efficiency, and both the observations suggest that other mechanisms than simply a difference in stored energy are present.

16.1.2 Flow stress as a measure of stored energy

The flow stress is a function of the substructure development during deformation. Thus, if driving pressure is the main cause of strain path dependence of recrystallisation, it is a reasonable approximation that the flow stress and the stored energy are proportional. Accordingly, recrystallisation properties should scale with flow stress. Lindh et al. (1993) observed a linear relationship between flow stress and recrystallisation temperature for high purity copper deformed in tension/compression and simple compression.

Embury et al. (1992) reported similar observations for pure aluminium deformed in combinations of tension and compression. After deformation to the same *net strain* in tension and tension/compression, the samples deformed in tension showed more rapid recrystallisation kinetics. If the samples instead were deformed to the same *flow stress* in different deformation modes, they showed equal recrystallisation kinetics. However, this relationship does not apply as a general rule. In the current studies, a vague relationship between flow stress and recrystallised grain size is observed for AA1050 deformed in cyclic and monotonic torsion, while such relationships are weak, if present at all, for AA3103. In the studies of Zhu and Sellars (1996), Al-2Mn deformed to different cumulative strains in tension, compression and tension/compression showed large differences in recrystallised grain sizes and recrystallisation kinetics for equal flow stresses. This means that other effects are present, although difference in stored energy is probably a contributing factor, particularly in pure metals.

16.1.3 Driving pressure and microstructure

The microstructural parameters that influence the driving pressure are the average subgrain size, the average subgrain misorientation and the dislocation density inside subgrains. Some studies have been done on the development of these properties during deformation along different strain paths. Before these studies are discussed further, a closer look at the individual contribution of the mentioned microstructural parameters on the driving pressure is required.

The individual effect of microstructural parameters on driving pressure

The equation for the driving pressure was derived in chapter 2.6.3. The equation enables separation of the contribution to driving pressure from dislocation density inside subgrains and average subgrain size/misorientation. If the principle of similitude is applied the contribution to the driving pressure from dislocation density and subgrain size and misorientation may be calculated as a function of the of Castro-Frenandez constant, C_d . Nord-Varhaug et al. (2000) measured subgrain sizes and dislocation densities in AlMg-alloys and AA1050 deformed in torsion, and reported values of C_d in the range 5.5 to 32, where the largest values corresponded to small deformations and large subgrain sizes (7-8 μ m.) In fig 16.1 (a-c) the individual contribution to the driving pressure from dislocation density inside subgrains and from subgrain size/misorientation is shown for different combinations of subgrain size and misorientation, and for four different values of C_d in the range 5-20. For a subgrain size of 2 μ m fig 16.1 shows that the contribution from the dislocation density is 2-3 orders of magnitude smaller than the contribution from subgrain size and misorientation, depending on the value of Castro-Fernandèz constant. For a subgrain size of 1 μ m, the difference is somewhat smaller, but keeping in mind that the value of Castro-Fernandèz constant usually decreases at small subgrain sizes, the difference is probably still at least two orders of magnitude. Based on the calculation, it is highly unlikely that differences in the dislocation density inside subgrains will affect the driving pressure for recrystallisation sufficiently to explain differences in recrystallisation properties of the observed magnitude. Thus, for further studies of strain path dependence of recrystallisation, measurements of average subgrain size and misorientation is more important than measurements of dislocation densities inside subgrains. The priority of measurements of subgrain

size and misorientation should be even easier as both these parameters could be efficiently measured in an FEG-SEM equipped with an EBSD system, providing sufficient statistics. On the other hand, TEM-measurements of dislocation densities are experimentally demanding and time consuming

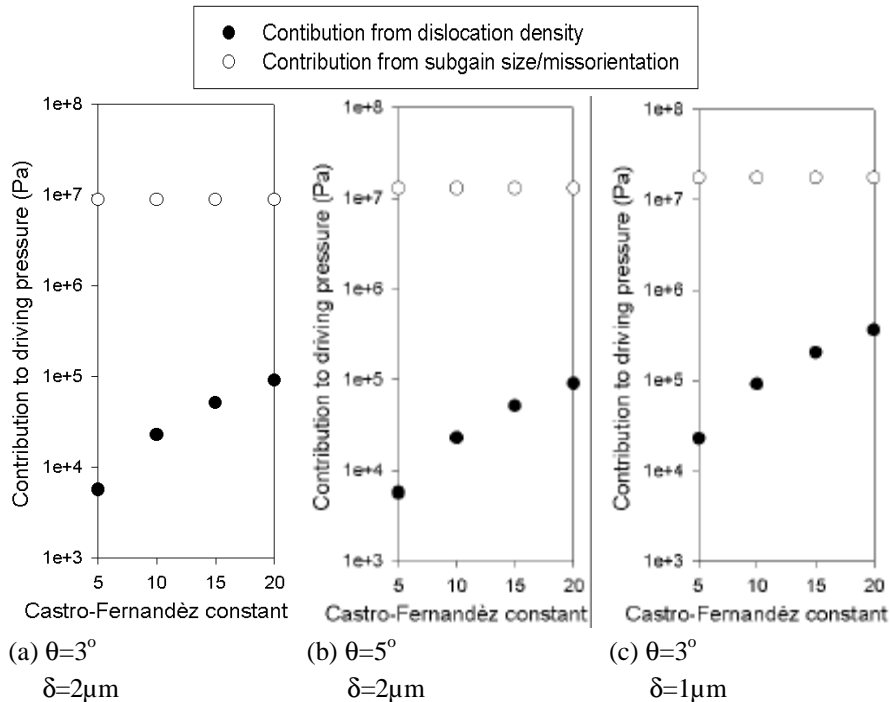


Fig 16.1: Contribution to driving pressure from dislocation density inside subgrains and subgrain size/misorientation, for given values of \mathbf{q} and \mathbf{d} . Plotted for different values of Castro-Fernandéz constant.

The significance of driving pressure

In the current study, the average subgrain size and misorientation have been studied by EBSD after different strain paths in torsion. No difference was found in the subgrain size, while the average subgrain misorientation was seen to be somewhat smaller after cyclic deformation, compared to monotonic. Similar experimental

observations of subgrain size and misorientation were also reported by Zhu and Sellars (1996). As no differences in subgrain size as function of strain path has been found, the only parameter having a notable influence on the driving pressure is the subgrain misorientation. The strain path dependent difference in driving pressure caused by this parameter is however so small that it is highly unlikely that the major reason for the changes in recrystallised grain size and recrystallisation kinetics as function of strain path is the difference in driving pressure. The experimental observations and modeling of recrystallisation after hot rolling in this study also suggest that other parameters than simply stored energy are of importance for the recrystallisation process. The microstructural data obtained from hardness measurements through thickness clearly indicated that the gradient in driving pressure from center to surface was not large enough to explain the difference in recrystallisation kinetics observed over the thickness. The results obtained by Higginson and Sellars (2002), for hot rolled steel, provide further evidence that other effects than simply a difference in driving pressure are present. The experiment consisted of two rolling passes with 50% reduction in the first pass and 20% reduction in the second pass. For some of the samples the rolling direction was reversed in the second pass, creating a difference in strain path. The subgrain size and the dislocation density were measured in the center of the slab ($S=0$) and close to the surface ($S=0.8$), and the results are presented in table 16.1.

Table 16.1: Subgrain sizes and dislocation densities for different rolling schedules and positions through thickness. (From Higginson and Sellars (2002))

Sample and location	Average subgrain size(μm)	Dislocation density (10^{14}m^{-2})
FF 0	0.54 \pm 0.12	3.9 \pm 1.00
FF 0.8	0.56 \pm 0.13	6.5 \pm 0.85
FR 0	0.48 \pm 0.11	3.3 \pm 1.08
FR 0.8	0.59 \pm 0.10	4.4 \pm 1.00

For the position closest to the surface there is a slight reduction of the driving pressure for the FR rolling schedule, as subgrain size increases and dislocation density decreases – the latter showing the most prominent change. Still, if the difference in recrystallisation kinetics is attributed to this difference, problems arise in the explanation of what happens in the sample center. As seen from table 16.1 the subgrain size in the center of the FR-rolled sample is actually smaller than in the sample subjected to a FF rolling schedule. Even if the dislocation density is somewhat larger after the FF rolling schedule the driving pressure is probably largest after the FR rolling schedule. Still the recrystallisation kinetics are slowed down just as much in the center of the sample as in the surface after the FR rolling schedule. This behavior was shown in fig 9.6, and indicates that other mechanisms are present. Black et al. (2001) observed the same behavior in hot rolled aluminium. Change of rolling direction did not only affect the recrystallisation kinetics in the sheared surface regions it also resulted in substantial retardation of the recrystallisation kinetics in the center of the slab.

The influence of strain path on recrystallisation all the way through thickness of the hot rolled slab is a very important point, as strain path effects in hot rolling have normally been seen as a phenomena related to the surface regions. In the surface, the shear deformation is large and the strain path change due to FF and FR rolling schedules is obvious. The center section of hot rolled slabs is normally expected to undergo almost pure plane strain compression. It is therefore quite surprising that a strain path effect is present in this position as well. In the study of Higginson et al. (2003) the texture was recorded for samples deformed in FF and FR rolling pass schedules. A small difference was found, indicating that rolling schedule also affects the center of the sample slightly.

16.2 Nucleation

As strain path effects on recrystallisation can't be explained in terms of differences in driving pressure only, the next natural step is to look at the nucleation process. The driving pressure will of course affect the number of successful nuclei, but as suggested in chapter 6.3 strain reversals may also affect the nucleation mechanisms directly. So far, not much has been published regarding the strain path effects on nucleation of recrystallisation

16.2.1 Nucleation mechanisms

Nucleation from grain boundaries

The model for nucleation from grain boundaries explains the strain path dependency of recrystallised grain size as a result of different grain boundary area. The basis of the mechanism is the reversal of the grain structure after cyclic deformation. For the case of cyclic torsion (the current study) and tension/compression (Zhu and Sellars (1996)), this development of grain shape is confirmed experimentally. As the model is based purely on geometrical considerations it could in principle be transferred to any combination of deformation modes. Still, care should be taken if a non-equiaxed starting microstructure is subjected to strain path changes different from 180°. In that case the resulting grain boundary area depends on the initial orientation of the sample. Higginson et al. (2002) studied recrystallisation in a hot rolled Al-2Mn alloy, subjected to strain path changes of 0°, 90°, 120° and 180° from combinations of free- and plane strain compression. Two different 90° strain path changes were used, and the recrystallisation properties of the two samples were drastically different, both in terms of grain size and kinetics. A non-equiaxed grain structure may be present in the hot rolled starting material, and a difference in grain boundary area may thus explain this result.

Particle stimulated nucleation

The proposed mechanism of reversal of deformation zones surrounding second phase particles is also translatable to other deformation modes. However, the occurrence of the mechanism is only observed indirectly and direct studies of the deformation zones in TEM may be required to prove the occurrence of the effect. Differently from the mechanism governing nucleation from grain boundaries the formation of deformation zones and the efficiency of nucleation from PSN is not equally easily predicted. The efficiency of nucleation by PSN is determined by several parameters. For cold deformation the particle size and the total strain are the most important. For hot deformation the Zener-Hollomon parameter and the particle size are the vital factors. Adding strain path effects on top of this complicates the prediction of PSN-efficiency further. Even if it could be experimentally determined that the deformation zones surrounding particles are weakened by reversed deformation, it would still be very tricky to predict which combinations of strains would cause nucleation by PSN and which would not.

Other nucleation mechanisms

It is of course also possible that other nucleation mechanisms are affected by strain path changes. It is not unlikely that the formation of transition bands and shear bands are affected by strain path changes. Both these microstructural defects are known to act as nucleation sites. Zhu and Sellars (1996) observed a drastic reduction in the density of microbands as a result of strain path changes in tension/compression, and it is not unlikely that other microstructural phenomena may be affected in a similar manner.

16.2.2 Site saturation

Deviations from site saturation will also cause difference in recrystallisation kinetics and recrystallised grain size. Zhu and Sellars (1996) partly explained the slower recrystallisation kinetics

after deformation in tension/compression compared to tension/tension as a result of larger deviation from site saturation in the cyclic case.

16.3 Comparison of the proposed mechanisms – influence of magnitude of strain reversal

In the two previous chapters, the recrystallisation dependence on strain path is explained as a combined effect of difference in driving pressure and effects of strain path on nucleation mechanisms. For nucleation from grain boundaries and particles, mechanisms for the change in nucleation density as function of strain path have been proposed. However, these effects will probably have a different dependence on the magnitude of strain after the reversal. This issue is illustrated in figure 16.2, where the flow stress and the development of grain shape and deformation zones surrounding particles as a function of strain and strain path is illustrated.

16.3.1 Driving pressure

As an approximation, the driving pressure and the flow stress are assumed to be related. Thus, the difference in driving pressure between monotonic and cyclic deformation will be largest immediately after the reversal of the strain. After reversal, the difference in driving pressure between cyclic and monotonic deformation decreases and in the end disappears. The effect on the flow stress curve of strain reversals is however depending strongly on alloy and deformation mode, and other patterns may of course occur. However as a general rule, the effect of differences in driving pressure is probably largest after small strain reversals.

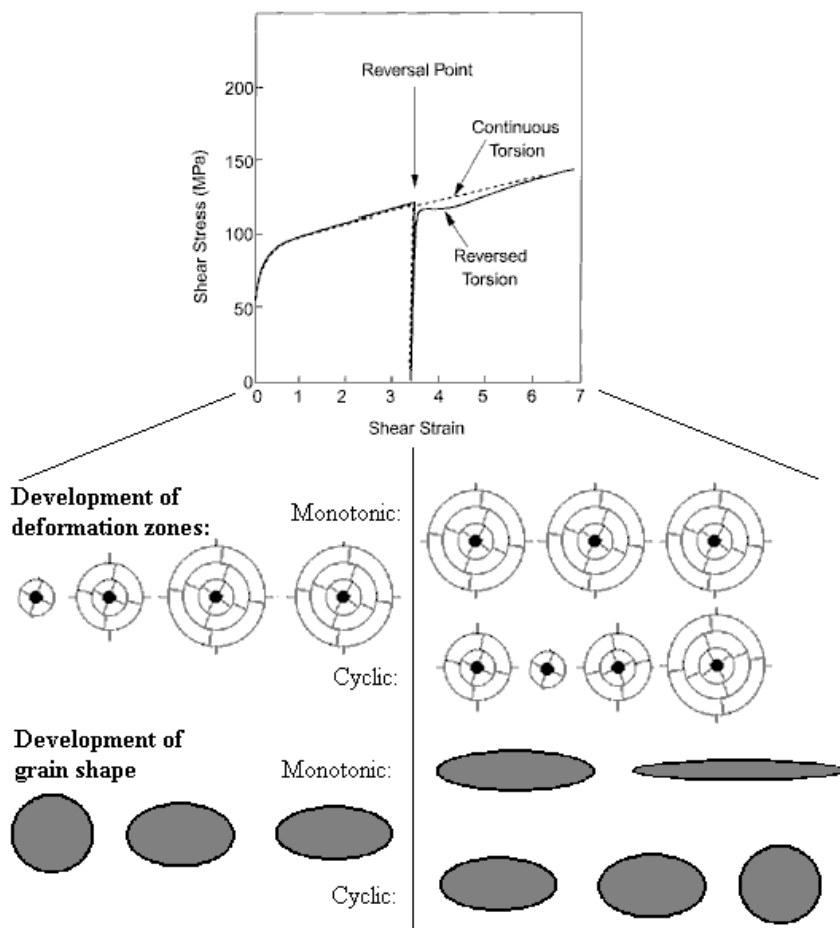


Fig 16.2: Summarized description of strain path effects on flow stress and nucleation mechanisms – as function of strain. Stress strain curve from (Davenport and Higginson (1998))

16.3.2 Particle stimulated nucleation

Looking at the development of deformation zones around particles, the diameter of the deformation zone increases during monotonic deformation and will reach saturation at some magnitude of strain. From this level of strain the density of PSN-nuclei will remain constant during monotonic deformation. After strain reversal, if the

theory of weakening of deformation zones proves correct, there will be a reduction in the density of PSN-nuclei until the deformation zone reaches a minimum size where the strain path related effect on PSN-nucleation will have its maximum value. Further increase of the strain from this value will then increase the diameter of the deformation zone, until saturation once again is reached.

16.3.3 Nucleation from grain boundaries

In monotonic deformation the grain boundary area per volume will increase with strain, in a manner characteristic for the deformation mode. This increase will continue until the grain boundary separation is so small that the grains are pinched off. For cyclic deformation, the grain boundary area will decrease until the initial value is reached at zero net strain. Then the grain boundary area will increase in the same manner as during monotonic deformation. Thus the difference in grain boundary area between cyclic and monotonic deformation, and accordingly the difference in the density of grain boundary nuclei, will be small just after reversal, and then increase with magnitude of the strain reversal.

16.4 Future work – suggestions, thoughts and challenges

The subject of strain path effects on recrystallisation has only been studied for a relatively short period of time, and only in a limited number of studies. However, experiments have shown that strain path effects on recrystallisation exist, and are of industrial relevance. Still the phenomenon is not fully understood, even under the most simplified experimental conditions. A basic understanding of the individual contributing mechanisms is important if the more complex industrial processes like hot rolling are to be explained. This knowledge must be obtained in simple laboratory experiments enabling full parameter control. A vital part of designing new

experiments is to isolate the effects from each proposed mechanism for individual study, in order to confirm their presence and influence in different alloy systems.

16.4.1 Alloy selection

In order to investigate the effect of strain reversals on PSN comparison between alloys containing particles and pure metal is a good way of obtaining knowledge. Thus, to do strain path experiments on as pure alloys as possible would be beneficial, as only the difference in driving pressure and grain boundary area should govern recrystallisation properties. A two pass hot rolling experiment with different rolling schedules using high purity aluminium would also be of interest to compare the effect of strain reversal with particle containing alloys on which the existing has been performed.

16.4.2 Non complete reversals

In industrial conditions the strain reversals are seldom complete ie. net strain is different from 0. This could for instance be seen in fig 13.2, showing the development of strain in the surface regions during hot rolling. As has been suggested in chapter 16.3, the magnitude of strain applied after reversal may influence which mechanism plays the major role in the strain path effect on recrystallisation. Thus, a torsion experiment consisting of a relatively large prestrain, and reversed strains of different magnitudes could be an idea.

Part IV: Summing up

17 References

Abtahi S., Sjølstad K., Marthinsen K. and Nes E., Proc. Recrystallisation and Grain Growth (ed. Gottstein and Molodov), Springer Verlag, Berlin, 251 (2001)

Adcock F., J.Inst. Met., **27**, 73 (1922)

Avrami M: J. Chem. Phys., **7**, 1103 (1939)

Backofen W. A., Trans. AIME, **188**, 1454 (1950)

Backhofen W. A., Deformation Processing, Addison-Whelesley publishing company, ISBN 0-201-00388-0 (1972)

Bailey J.E., Phil. Mag., **5**, 833 (1960)

Bailey J.E., Hirsch P.B., Proc. Roy. Soc., **267A**, 11 (1962)

Bardal A., Lindseth I., Vatne H.E. and Nes E., Proc. 16th Risø Int. Symposium (ed. Hansen *et al.*), Risø National Laboratory, Roskilde, 261 (1995)

Barrett C.S., Trans. Metal. Soc. A.I.M.E., **137**, 128 (1940)

Bate P. S. and Wilson D. V., Acta Met., **14**, 1097 (1986)

Baxter G. J., Furu T., Q. Zhu, J. A. Whiteman and C. M. Sellars, Acta Met, **47**, 2367 (1999)

Bay, B. and Hansen, N., Metall. Trans. A, **14A**, 287 (1984)

Beck P.A., Sperry P.R., J. Appl. Phys., **21**, 150 (1950)

Beynon. J. H. and Sellars, C. M., ISIJ Int., **32**, 359 (1992)

Chapter 17: References

- Black M. P., Higginson R. L. and Sellars C. M., *Mat. Sci. Tec*, **17**, 1055 (2001)
- Burgers W.G., Louwense P.C., *Z. Physik*, **61**, 605 (1931)
- Burke J.E., Turnbull D., *Prog. Met. Phys.*, **3**, 220 (1952)
- Canova G.R., Kocks U.F., Jonas J.J., *Acta Met.*, **32**, 211 (1984)
- Castro-Fernandez F.R., Sellars C.M., Whiteman J.A., *Mat. Sci Tech*, **6**, 453 (1990)
- Cowan J. R., Higginson R.L., Hutchinson W.B., Bate P.S., *Mater. Sci. Technol.* **11**, 1104 (1995)
- Daaland O., *Dr.ing thesis, The Norwegian Institute of Technology, Trondheim* (1993).
- Daaland O., Nes E., *Acta mater.*, **44**, 1389 (1996a)
- Daaland O., Nes E., *Acta mater.*, **44**, 1413 (1996b)
- Davenport S. B., Higginson R. L., *Mat. proc. tecn.*, **98**, 267 (2000)
- Dehlinger U., *Metallw.*, **7**, 1172 (1928)
- Dillamore I.L., Katoh H., *Metal Science*, **8**, 73 (1974)
- Dillamore I.L., Morris P.L., Smith C.J.E., Hutchinson W.B., *Proc. Royal Society*, **329A**, 405 (1972)
- Doherty R.D., "Nucleation", In: "Recrystallization of Metallic Materials". (Ed. F. Haessner), Dr. Riederer-Verlag GmbH, Stuttgart, 23 (1978)
- Doherty R.D, *Scripta met.*, **19**, 927 (1985)

Chapter 17: References

- Dons A.L., Nes E., *Mat. Sci. Tech.*, **2**, 8 (1986)
- Dons A.L., Jensen E.K., Langsrud Y., Trømborg E., and Brusethaug S., *Met. Trans. A*, **30A**, 2135 (1999)
- Dons A.L., *Journal of Light Metals*, **1**, 133 (2001)
- Duan X. and Sheppard T., *Journ. Mat. Proc. Tec.*, **130-131**, 245 (2002)
- Ekström H.E., Östensson L. and Hagström J., "Dispersoids and constituent size distribution in 2.2 mm thick hot rolled bands of AA3104", Brite-Euram Report BE96-3364 (1998)
- Embury J. D., Poole W.J. and Koken E., *Scr. Met. et Mat.*, **27**, 1465 (1992)
- Engler O., Hirsch J., Lücke K., *Acta Met.*, **43**, 121 (1995)
- Estrin, Y., Mecking, H., *Acta Met.*, **32**, 57 (1984)
- Fields D.S., Backofen W.A., *Am. Soc. Test. Mater. Proc.*, **57**, 1259 (1957)
- Furu T., Marthinsen K., Nes E., *Mater. Sci. Tech.*, **6**, 1093 (1990)
- Furu T., Marthinsen K., Nes E., *Materials Science Forum*, **113-115**, 41 (1993a)
- Furu T., Ørsund R. and Nes E., *Acta met. mater.*, **43**, 2209 (1995)
- Furu T., Ørsund R. and Nes E., *Mater. Sci. Eng*, **A214**, 122 (1996)
- Furu T., Shercliff H. R., Baxter G. J. and Sellars C. M., *Acta mater.*, **47**, 2377 (1999)
- Glez J. Ch. and Driver J. H., *Acta Mat.*, **51**, 2989 (2003)
- Gokhale A.M. and DeHoff T.T., *Met. Trans.*, **16A**, 559 (1985)

Chapter 17: References

Hargreaves M.E., Loretto M.H., Clarbrough L.M. and Segall R.L., NPL Symposium No. 15 Teddington, NMSO, 209 (1963)

Hasegawa T., Yakou T. and Karashima S., *Mat. Sci. Eng.*, **34**, 267 (1975)

Higginson R. L. and Sellars C. M., *Mat. Sci. Eng.*, **A338**, 323 (2002)

Higginson R. L., MacGregor A. and Palmiere E.J, **Vols. 396-402**, 303 (2002)

Higginson R. L., Pinna C., Beynon J. H. and Wynne B. P., *Mat. Sci. Tec.*, **19**, 477 (2003)

Hjelen J., Nes E., *Proc. 7th Int. Risø Symp.*, (Eds. Hansen *et al.*), 367 (1986)

Hjelen J., Ørsund R., Nes E., *Acta Met.*, **39**, 1377 (1991)

Humphreys F.J., *Acta Met.*, **25**, 1323 (1977)

Humphreys F.J., *Acta Met.*, **27**, 1801 (1979)

Humphreys F.J., Kalu P.N., *Acta Met.*, **35**, 2815 (1987)

Hutchinson W.B. and Davis T., *Proc 4th Int. Conf. on the Behaviour of Materials*, Eds. Carlsson J. and Olsson N. G., Stockholm, 1227 (1983)

Hutchinson W.B., *Acta Met.*, **37**, 1047 (1989)

Iyer A.A, and Gordon P., *Trans. Met. Soc. AIME.*, **215**, 729 (1959)

Johnson W.A. and Mehl R.F., *Trans. AIME*, **135**, 416 (1939)

Kassner M.E., McMahon M.E., *Metal. Trans.*, **A18**, 835 (1987)

Chapter 17: References

Knustad O., McQueen H.J., Ryum N., Solberg J.K., *Praktische Metallogr.*, **22**, 215 (1985)

Kocks, U F., *J. Eng. Mater. Tech. (ASME-H)*, **98**, 76 (1976)

Kocks, U F., Mecking, H., *Prog. Mat. Sci.*, **48**, 171 (2003)

Kolmogorov A.N: *Izv. Akad. Nauk., USSR Ser. Matemat.*, **1**, 355 (1937)

Lindh E., Hutchinson B. and Ueyama S., *Scr. Met. et Mat.*, **29**, 347 (1993)

Lücke K., *Proc. ICOTOM 7*, (Eds. Brakman *et al.*) The Netherlands Society for Materials Science, Zwijndrecht, The Netherlands, 195, (1984)

Marthinsen K. and Nes E., *Mater. Sci Tech.*, **17**, 376 (2001)

Maurice Cl. and Driver J. H, *Acta Mater*, **45**, 4627 (1997)

McLaren A.J and Sellars C.M., *Mater. Sci. Tec.*, **8**, 1090 (1992)

McLaren A.J, Mat N.Le, Beynon J.H and Sellars C.M., *Ironmaking and Steelmaking*. **22**, 71 (1995)

McQueen H.J., Knustad O., Ryum N., Solberg J.K., *Scripta met.*, **19**, 73 (1985)

McQueen H.J., Solberg J.K., Ryum N., Nes E., *Phil. Mag.*, **60A**, 473 (1989)

Mecking H. and Kocks U. F., *Acta Met.* **29**, 1865 (1981)

Montheillet F., Cohen M., Jonas J.J., *Acta Met.*, **32**, 2077 (1984)

Chapter 17: References

- Mousavi, M. G., Diploma Thesis, The Norwegian institute of technology, Department of metallurgy (1995)
- Mughrabi H., Mater. Sci. Eng. **85**,15 (1987)
- Nes E., Scripta Met. Mater., **33**, 225 (1995)
- Nes, E., Prog. Mat. Sci., **41**, 129 (1998)
- Nes E., Proc. 1st Int. Risø Symp., (eds. Hansen *et al.*), 85 (1980)
- Nes E., Ryum N., Hunderi O., Acta Met., **33**, 11 (1985)
- Nes E. and Furu T., Scr. Met. Mater., **33**, 87 (1995)
- Nes, E., Marthinsen, K., Mat. Sci. Eng., **A322**, 176 (2002)
- Nord-Varhaug K., Forbød B., Benstad J., Pettersen T., Rønning B., Bardal A., Benum S., Marthinsen K. and Nes E., Mat. Sci. Forum, **Vols. 331-337**, 1387 (2000)
- Perdrix Ch., Perrin M.Y., Montheillet F., Mèm. Sci. Rev. Métal., **78**, 309 (1981)
- Pettersen T., Dr.ing. thesis, Norwegian University of Science and Technology (1999)
- Pettersen T. and Nes E., Met. Trans, **34A**, 2717 (2003a)
- Pettersen T. and Nes E., Met. Trans, **34A**, 2727 (2003b)
- Pettersen T., Nes E. and Holmedal B., Met. Trans, **34A**, 2737 (2003)
- Ridha A.A., Hutchinson W.B., Acta Met., **30**, 1929 (1982)
- Robson J. D. and Pragnell P. B., Mat. Sci. Forum, **Vols. 396-402**, 545 (2002)

Chapter 17: References

Rollett A. D., Lowlet T., Kocks U. F. and Stout M. G, ICOTOM 8, 473 (1988)

Roters F., Raabe D. and Gottstein G., Acta Mat. **48**, 4181 (2000)

Ryen Ø., Dr. ing. thesis, Norwegian University of Science and Technology (2004)

Rønning B., Dr.ing. thesis, Norwegian University of Science and Technology (1998)

Rønning B., Nord-Varhaug K., Iveland T., Furu T., Nes E., reap task2, Norwegian University of Science and Technology, NTNU report (1998)

Sachs E., Ver. dt. Ing., **72**, 734 (1928)

Sakai T., Saito Y., Hirano K. and Kato K., Trans. Iron Steel Inst Jpn, **28**, 1028 (1988)

Sandstrøm R., Lehtinen B., Hedman E., Groza I. and Karlsson S., J. Mat. Sci. **13**, 1229 (1978)

Sellars C.M., McGregor Tegart W.J., Met. Rev., **17**, 1 (1972)

Sjølstad K., Dr. ing. thesis, Norwegian University of Science and Technology, Trondheim (2003)

Smith C.S., Trans. Metal. Soc. A.I.M.E., **175**, 15 (1948)

Solberg J.K., McQueen H.J., Ryum N., Nes E., Phil. Mag. A, **60**, 447 (1989)

Stoltz R. E. and Pelloux P.M, Met. Trans A., **7A**, 1295 (1976)

Stout M. G. and Rollett A.D., Met. Trans, **21A**, 3201 (1990)

Chapter 17: References

Sæter J. A., Dr. ing. thesis, Norwegian University of Science and Technology, Trondheim (1997)

Taylor G. I., *J.Inst. Met.*, **62**, 307 (1938)

Vandermeer R.A. and Rath B.B., *Met. Trans.*, **20A**, 391 (1989)

Varma S.K and Willits B.L: *Met. Trans.*, **15A**, 1502 (1984)

Varma S.K: *Mat. Sci. Eng.*, **L19**, 82 (1986)

Varma S.K. and Westrom B.C: *J. Mat. Sci. Lett.*, **7**, 1092 (1988)

Vatne H.E., Dr. ing. thesis, Norwegian Institute of Technology, Trondheim (1995)

Vatne H.E., Benum S., Shahani R., Nes E., *Proc. 16th Int. Risø Symp.*, 573 (1995).

Vatne H.E., Furu T., Ørsund R., Nes E., *Acta Met.*, **44**, 4463 (1996a)

Vatne H.E., Marthinsen K., Ørsund R. and Nes E., *Met. Trans.*, **A27**, 4133 (1996b)

Vatne H.E., Furu T., Nes E., *Mat. Sci. and Tech.*, **12**, 201 (1996c)

Vatne H.E., Shahani R., Nes E., *Acta Metall. Mater.*, **44**, 4447 (1996d)

Vatne H. E., Mousavi M.G, Benum S., Rønning B. and Nes E., *Mat. Sci. Forum*, **Vols. 217-222**, 553 (1996e)

Weiland H., Hirsch J., *Textures & Microstr.*, **14-18**, 647 (1990)

Wilson, D. V. and Bate, P. S., *Acta Metall. Mater.*, **42**, 1099 (1994)

Chapter 17: References

Zhu Q. and Sellars C. M., International conference on Recrystallisation and related topics, Monterey (1996)

Ørsund R., Nes E., *Scr. met.*, **23**, 1187 (1989)